Purdue University
Purdue e-Pubs

Department of Electrical and Computer Engineering Technical Reports

Department of Electrical and Computer Engineering

12-1-1984

Final Report: Theory of Advanced High Efficiency Concentrator Cells

Mark S. Lunstrom
Purdue University

R. J. Schwartz
Purdue University

C. M. Maziar
Purdue University

P. D. DeMoulin
Purdue University

Follow this and additional works at: https://docs.lib.purdue.edu/ecetr

Lunstrom, Mark S.; Schwartz, R. J.; Maziar, C. M.; and DeMoulin, P. D., "Final Report: Theory of Advanced High Efficiency Concentrator Cells" (1984). *Department of Electrical and Computer Engineering Technical Reports.* Paper 533.
https://docs.lib.purdue.edu/ecetr/533

This document has been made available through Purdue e-Pubs, a service of the Purdue University Libraries. Please contact epubs@purdue.edu for additional information.

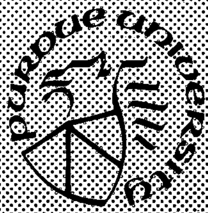

Final Report: Theory of Advanced High Efficiency Concentrator Cells

M.S. Lundstrom
R.J. Schwartz
C.M. Maziar
P.D. DeMoulin

TR-EE 84-49
December 1984

School of Electrical Engineering
Purdue University
West Lafayette, Indiana 47907

Prepared for Solar Energy Research Institute, under sub-contract XL-3-03124-1

FINAL REPORT

THEORY OF ADVANCED HIGH EFFICIENCY CONCENTRATOR CELLS

M.S. Lundstrom

R. J. Schwartz

C. M. Maziar

P. D. DeMoulin

School of Electrical Engineering

Purdue University

West Lafayette, IN 47907

December 1984

Prepared for Solar Energy Research Institute, under sub-contract XL-3-03124-1

TABLE OF CONTENTS

Page

LIST OF TABLES iv

LIST OF FIGURES vi

ABSTRACT x

CHAPTER I - PROJECT OVERVIEW 1

1.1 Review of Device Models 7
Van der Plas, James, Moon and Nelson 10
Konagai and Takahashi 11
Tsaur and Milnes 12
Lamorte and Abbott 13
Sutherland and Hauser 14
1.2 Parameter Compilation for GaAs Cell Modeling 15
1.3 Numerical Model Development 16
1.4 Device Model Verification 16
1.5 Demonstration of Heterostructure Modeling 18
1.6 Summary and Conclusions 19

CHAPTER 2- GaAs MATERIAL PROPERTIES AND MODELS 20

2.1 GaAs ... A Material Description 21
2.2 Carrier Statistics 24
Intrinsic Carrier Concentration 24
np Product 28
Bandgap Narrowing 35
2.3 Mobility 39
2.4 Absorption 53
Absorption Mechanisms 54
Free-Carrier Absorption 55
Impurity Absorption 59

Page

Interband Transitions 62
2.5 Refractive Index 72
2.6 Minority Carrier Diffusion Lengths and Lifetimes 78

CHAPTER 3- ANTI-REFLECTION COATINGS MATERIALS AND MODELS 82

3.1 $Al_xGa_{1-x}As$ 83
Bandgaps 83
Absorption Coefficient 86
Refractive Index 91
3.2 Native Oxide 93
3.3 Reflection from Multiple-Layer Structures with Complex Refractive Indices 97

CHAPTER 4- COMPARISON OF SCAP1D/GAAS TO EXPERIMENT 100

4.1 Fan-Bozler Shallow Homojunction 100
4.2 Fan-Bozler Cell / No AR Coating 113
4.3 Borrego p^+n Cell 115
4.4 Sahai Heteroface 118
4.5 Summary 121

CHAPTER 5- OPEN-CIRCUIT VOLTAGE ENHANCEMENT IN GRADED GAP CELLS 122

5.1 Introduction 122
5.2 Origin of the Graded Bandgap Photovoltage 124
5.3 Numerical Simulation of Heterostructures 131
5.4 Results of Numerical Simulation 132
5.5 Cell Design and Optimization 139
5.6 Summary 146

LIST OF REFERENCES 147

APPENDICES

Appendix A 157
Appendix B 160
Appendix C 169

Page

LIST OF TABLES

Table Page

Table 1.1 Plots Available from PLOT1D/SCAP1D 17

Table 2.1 Common Dopants for GaAs....................23

Table 2.2 Material Constants for GaAs....................26

Table 2.3 Electron and Hole Mobilities of Common Semiconductors 42

Table 2.4 Caughey-Thomas Parameters Extracted from Walukiewicz 42

Table 3.1 Parameters for Refractive Index Model....................94

Table 4.1 Results of SCAP1D Simulation of Fan-Bozler Cell 102

Table 4.2 Parameters Used to Simulate Fan-Bozler Shallow Homojunction....................103

Table 4.3 J_{SC}, and V_{0C} for Several Solar Concentrations 107

Table 4.4 Ideal Diode Parameters....................107

Table 4.5 Results of SCAP1D Simulations Using Internal Reflectance Routine and Lumped Shadow Factor 111

Table 4.6 Results of SCAP1D Simulations Using a Step Junction Profile and an Erfc Profile....................112

Table | Page

Table 4.7 Results of SCAP1D Simulation of Fan-Bozler Cell Without an AR Coating....113

Table 4.8 Parameters Used to Simulate a Fan-Bozler Cell Without an AR Coating....114

Table 4.9 Parameters Used to Simulate the Borrego p^+n Cell....117

Table 4.10 Results of SCAP1D Simulation of the Borrego Cell....117

Table 4.11 Parameters Used to Simulate the Sahai Heteroface Cell....119

Table 4.12 Results of SCAP1D Simulation of the Sahai Heteroface Cell....121

Table 5.1 Additional Information for the Simplified Cell....134

Table 5.2 Additional Information for the Practical Cell....141

LIST OF FIGURES

Figure Page

Figure 1.1.1 Typical Shallow Homojunction Cell 3

Figure 1.1.2 Heteroface Cell 4

Figure 1.1.3 Graded Band-Gap Cell a) Energy Band Diagram, b) Typical Cell Structure 5

Figure 2.1.1 Gallium Arsenide Bandstructure 25

Figure 2.2.1 $n_i(T)$ ... T = 100 - 10 00 K 29

Figure 2.2.2 $n_i(T)$ ... T = 275 - 325 K 30

Figure 2.2.3 Distribution of Carriers Over the Γ,X and L Bands versus η_C 33

Figure 2.2.4 Carrier Concentrations in Γ,X and L bands versus η_C 34

Figure 2.2.5 **np** Product versus η_C 36

Figure 2.2.6 **np** Product versus N_D Including Heavy Doping Effects 39

Figure 2.3.1 Electron Mobility versus Electron Concentration for Several Compensation Ratios 47

Figure 2.3.2 Fit of NREF (Θ) to Extracted Parameters 49

Figure 2.3.3 Fit of $\mu_{min}(\Theta)$ to Values Extracted from Walukiewicz 50

Figure 2.3.4 Fit of $\alpha(\Theta)$ to Values Extracted from Walukiewicz 51

Figure Page

Figure 2.4.1 Free Carrier Absorption of Incident Radiation 56

Figure 2.4.2 Absorption Coefficient versus λ Showing Effects of Free-Carrier Absorption 58

Figure 2.4.3 Optically Induced Transitions Between Bands and Impurity Levels 60

Figure 2.4.4 Idealized Fundamental Absorption Edge 61

Figure 2.4.5 Transistion Between Indirect Valleys 63

Figure 2.4.6 Transistion Between Direct Valleys 64

Figure 2.4.7 Comparison Between Absorption Coefficient Model and Experimentally Determined Results 66

Figure 2.4.8 Absorption Coefficient for Heavily Doped n-Type GaAs 68

Figure 2.4.9 Absorption Coefficient for Heavily Doped p-type GaAs 69

Figure 2.4.10 Optical Generation versus Distance for Heavily Doped n-type GaAs 70

Figure 2.4.11 Optical Generation versus Distance for Heavily Doped p-type GaAs 71

Figure 2.5.1 Refractive Index of GaAs 74

Figure 2.5.2 Optical Generation for Heavily Doped n-Type GaAs Considering Effects on the Refractive Index 77

Figure 2.6.1 Minority Carrier Diffusion Length, L_p 80

Figure 2.6.2 Minority Carrier Diffusion Length, L_n 80

Figure 3.1.1 $Al_xGa_{1-x}As$ Bandgaps versus Composition 84

Figure Page

Figure 3.1.2 $Al_xGa_{1-x}As$ Absorption Coefficient for Several Compositions 90

Figure 3.1.3 $Al_xGa_{1-x}As$ Refractive Index for Several Compositions 95

Figure 3.3.1 Enumeration of Layers for Multi-Layered Structure 99

Figure 4.1.1 Energy Band Diagrams a) Step Profile b) Erfc Profile 104

Figure 4.1.2 Photocurrent versus Applied Voltage... Fan and Bozler Shallow Homojunction 105

Figure 4.1.3 Spectral Response of Fan and Bozler Cell. Simulations Run for Oxide of 0.085μm 108

Figure 4.1.4 Spectral Response of Fan and Bozler Cell. Simulations Run for Oxide of 0.095μm 109

Figure 4.1.5 Optical Generation Rate 110

Figure 4.2.1 Spectral Response of Fan and Bozler Cell with no Anti-Reflection Coating 116

Figure 4.3.1 Internal Quantum Efficiency of Borrego Cell 120

Figure 5.2.1 Graded Bandgap Solar Cell Equilibrium Energy Band Diagram 125

Figure 5.2.2 Schematic Device Representation 127

Figure 5.4.1 Device Structure of a Graded Gap Solar Cell Designed to Illustrate Voc-Enhancement 133

Figure 5.4.2 Voc versus Solar Intensity for the Simple Cell 135

Figure 5.4.3a 1-Sun Carrier Concentrations at Voc 136

Figure Page

Figure 5.4.3b 1000 Sun Carrier Concentrations at Voc....137

Figure 5.4.3c 5000 Sun Carrier Concentrations at Voc....138

Figure 5.5.1 Device Structure of a Graded Gap Cell Designed for Reduced Series Resistance....140

Figure 5.5.2 Voc versus Solar Intensity for the Practical Cell....143

Figure 5.5.3 Fill factor and Efficiency versus Solar Intensity....144

Figure 5.5.4 I versus V for the Practical Cell....145

Appendix Figure

Figure B.1 Energy Band Diagrams..Fan-Bozler Shallow Homojunction....161

Figure B.2 Optical Generation....162

Figure B.3 Excess Carrier Concentration....163

Figure B.4 Recombination Rate....164

Figure B.5 Charge Density....165

Figure B.6 Current Density....166

Figure B.7 Carrier Concentration....167

Figure B.8 Electric Field....168

ABSTRACT

The goal of this project was to begin developing accurate, and ultimately predictive, device models for III-V concentrator cells. The project consisted of extending a one-dimensional numerical device model previously developed at Purdue to III-V solar cells. We also began verifying the accuracy of the code by comparing computed and measured solar cell characteristics. Gallium arsenide was selected because it is the most mature III-V technology and because GaAs solar cells have demonstrated high conversion efficiency [1,2,3]. The present device model should be useful in optimizing GaAs solar cells and forms a foundation that can be extended to other III-V homo- and heterostructure solar cells.

The numerical device model developed in this work solves Poisson's equation simultaneously with the electron and hole continuity equations without making common assumptions such as low-level injection, piece-wise uniform doping, neglect of space-charge recombination, etc. Materials models for GaAs solar cells (e.g. intrinsic carrier concentration, carrier mobilities, lifetimes, optical absorption and reflection coefficients, etc.) were compiled, evaluated, and in some cases extended. These materials models were then implemented into the numerical device model. The device model was also extended to analyze optical absorption and reflection from bare and anti-reflection (AR) coated cells.

To test the GaAs cell model, we compared its predictions to measured results for an N^+P cell (the shallow homojunction cell reported by Fan and co-workers) and a P^+N cell (fabricated by Borrego and co-workers). In general, good agreement between theory and experiment was obtained for both concentrated and unconcentrated conditions. Although detailed comparisons of the model's predictions with measured results continue, the present model is a useful tool for GaAs cell design and optimization.

CHAPTER 1

PROJECT OVERVIEW

The goal of this project was to begin developing accurate, and ultimately predictive, device models for III-V concentrator cells. The work described in this report consisted of developing and verifying a one-dimensional computer simulation program for gallium arsenide (GaAs) based solar cells. The motivation for the project arose from the observations that GaAs is the most mature III-V technology and that GaAs solar cells have demonstrated high conversion efficiency [1]. The results described in this report should be useful in optimizing GaAs solar cells and form a foundation that can be extended to other III-V cells.

Gallium arsenide displays several strengths as a photovoltaic material. It has been known for many years that GaAs's band-gap is a nearly ideal match to the solar spectrum [2]. In addition the temperature sensitivity of cells fabricated from GaAs is less than that of those made of Si, in part due to the wider band-gap of GaAs. At 600 K, GaAs cells are roughly twice as efficient as their Si counterparts [3] making the GaAs cell more appealing for concentrator application. In addition, this material is particularly attractive for use in space because of its resistance to radiation. Minority carriers in GaAs have such short lifetimes (1-5ns) when compared to those of Si ($\sim$250 μs) that the additional recombination mechanisms introduced by defects caused by exposure to high energy radiation do not appreciably compete with the existing

recombination mechanisms. GaAs is also a compositional end-point of a ternary alloy system, $Al_xGa_{1-x}As$, which is useful in the application to heterostructure devices. Heterostructures built in this alloy system have been observed to have low interface recombination velocities, attributed to the good lattice match for the system across the compositional range.

Model development must be done in view of the anticipated cell device structures and operating conditions. Since GaAs cells are likely to be used in concentrator systems, care must be taken not to imbed assumptions in the model that would preclude its use at high solar intensity. Many device geometries require a two (or even three) dimensional analysis.

The n^+p shallow homojunction cell reported by Fan and Bozler [4] is shown in Fig. 1.1.1. This cell reduces surface recombination losses by employing a very thin emitter. A one-dimensional device model (or quasi-2D model) suffice for this cell. Nevertheless, it should be noted that two-dimensional effects associated with the contact grid can be important and must be treated carefully.

In the heteroface cell, the active portion of the device is isolated from the surface by a thin layer of high-bandgap semiconductor. A typical heteroface cell structure is shown in Fig. 1.1.2. For such cells, it may be possible to treat the high-bandgap semiconductor as an antireflection coating that also reduces the front surface recombination velocity. A conventional, homojunction, device model may, therefore, prove adequate for modeling heteroface cells. The graded bandgap cell shown in Fig. 1.1.3 offers the potential for improved spectral response and, possibly, enhanced open-circuit voltage. To model this cell, it is essential to treat carrier transport, generation and recombination within

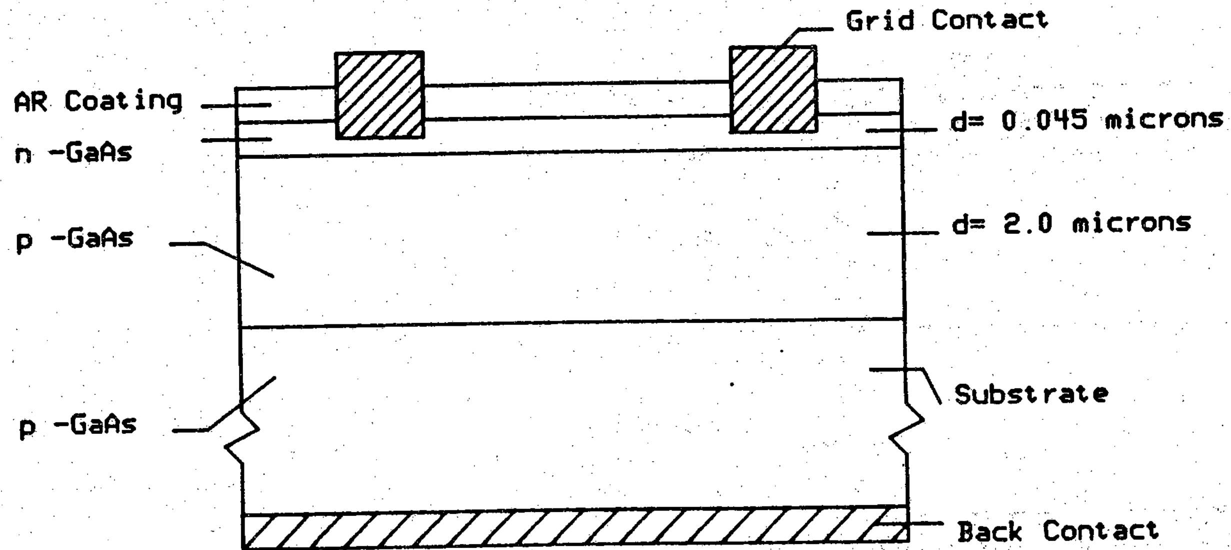

Figure 1.1.1 Typical Shallow Homojunction Cell

HETEROFACE

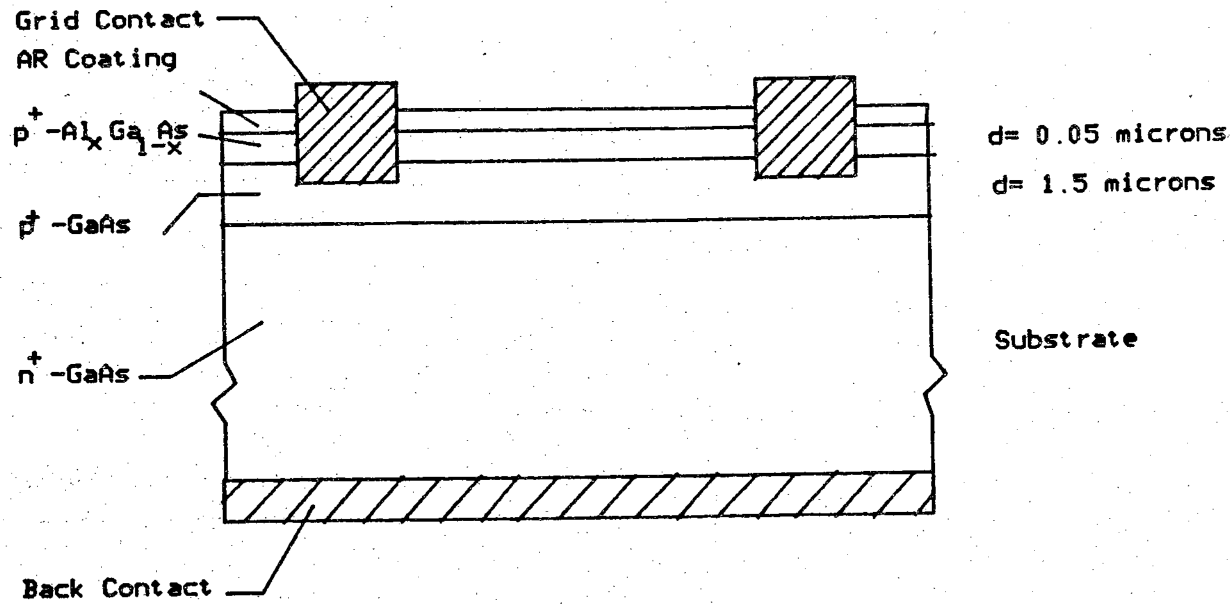

Figure 1.1.2 Heteroface Cell

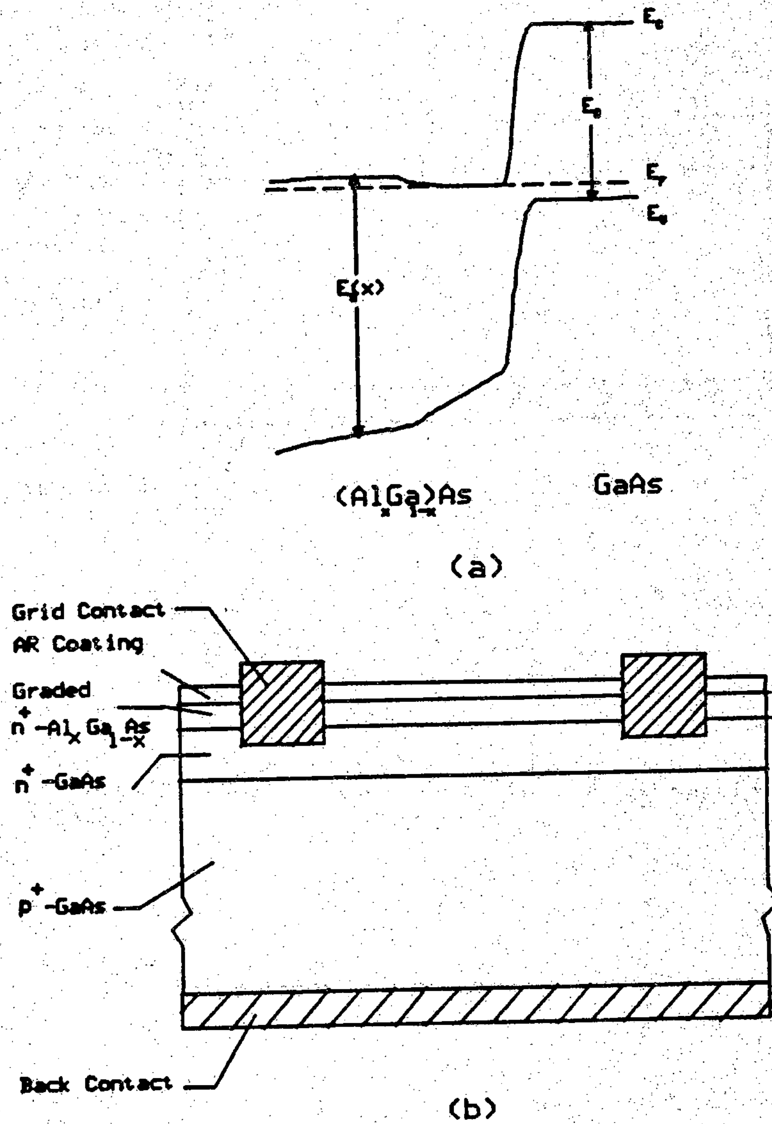

Figure 1.1.3 Graded Band-Gap Cell a) Energy Band Diagram, b) Typical Cell Structure

the compositionally nonuniform graded region.

Project Objectives

Our ultimate objective is to develop a versatile, two-dimensional simulation program for III-V homo- and heterostructure concentrator cells. Work under this contract was devoted to establishing one-dimensional modeling capability for GaAs homojunction cells. The specific tasks performed during the past year were:

- Critical review of existing III-V device models
- Compilation of material parameters required for device modeling
- Development of a 1-D numerical model for GaAs solar cells
- Assessment of model accuracy
- Demonstration of heterostructure modeling capability

We also initiated work to design an optimized GaAs homojunction cell. Each of the tasks listed above is described in detail in this report. The following section reviews the state-of-the-art for III-V solar cell device models. The remaining sections in this chapter highlight significant results for each task; the reader is referred to later chapters for details.

1.1 Review of III-V Solar Cell Modeling

Our first task was to review the capabilities and weaknesses of existing III-V solar cell models. To model a solar cell, three coupled partial differential equations must be solved. A semiconductor device operating in steady-state is described by Poisson's equation,

$$\nabla^2 V + \frac{1}{\kappa_s}\nabla\kappa_s \cdot \nabla V = \frac{q}{\kappa_s \epsilon_0}\left(n - p - DOP^+ \right), \tag{1.1.1}$$

and the hole and electron continuity equations

$$\nabla \cdot \vec{J}_p = q\,(G - R), \tag{1.1.2}$$

$$\nabla \cdot \vec{J}_n = -q\,(G - R). \tag{1.1.3}$$

The parameter, $DOP^+ = N_D^+ - N_A^-$, is the net ionized doping density. The optical generation rate is G, and R is the net recombination rate.

The modified band structure associated with heavy impurity doping has important effects on carrier transport. A convenient Boltzmann-like form for the transport equations is [24]:

$$\vec{J}_p = -pq\mu_p \nabla(V - V_p) - kT\mu_p \nabla p \tag{1.1.4}$$

and

$$\vec{J}_n = -nq\mu_n \nabla(V + V_n) + kT\mu_n \nabla n . \tag{1.1.5}$$

The band parameters, ∇V_p and ∇V_n, which appear like drift terms in these equations account for the effects of the nonuniform band structure and Fermi-Dirac statistics [24]. The quantity, $(V_p + V_n)$, may be interpreted as an

effective bandgap shrinkage [24].

An effective intrinsic carrier concentration can be defined as [24]

$$n_{ie}^2 = n_o p_o \;, \tag{1.1.6}$$

which is related to the effective gap shrinkage by

$$n_{ie}^2 = n_{io}^2 = e^{\frac{q(V_p^o + V_n^o)}{kT}} \tag{1.1.7}$$

where the superscript "o" denotes equilibrium values. The effective intrinsic carrier concentration is equal to n_{io} for low doping densities, but when the doping density is large, the effects of band tailing and gap shrinkage increase n_{ie}. The influence of Fermi-Dirac statistics is also included in n_{ie} (through $V_p^o + V_n^o$). The effective gap shrinkage (or equivalently, the effective intrinsic carrier concentration) is the parameter inferred from electrical measurements of heavily doped semiconductor devices [24].

Use of these equations makes the assumptions that the Boltzmann Transport Equation and the quasi-static local field approximation are valid [13]. For application to photovoltaic work there is little question about the validity of these approximations. Since (1.1.4) and (1.1.5) are written in Boltzmann-like form, they are particularly convenient for analyzing semiconductor devices. The two parameters, V_p and V_n, describe the effects of the nonuniform band structure and the influence of Fermi-Dirac statistics. Although bandgap narrowing has received little attention for III-V devices such as solar cells or transistors, it does have important effects in III-V semiconductor lasers.

Two classes of device models can be identified, those which solve (1.1.1) - (1.1.3) directly by numerical techniques and, more commonly, those which make assumptions to simplify (1.1.1) - (1.1.3), then solve the resulting

simplified equations. Since both classes of models are sometimes referred to as computer models, some confusion can result. In this review, we will attempt to clearly identify the equations upon which the various models are based.

Models that are based on simplifications of (1.1.1) - (1.1.3) usually solve the minority carrier diffusion equation. The commonly used approximations are [14]:

- Operation is in the low-level injection range.
- The electric field is approximately zero in the regions under analysis (or is equal to its value in equilibrium).

Other common assumptions include, no recombination in the space-charge region, mobilities independent of position, absorption coefficients independent of position, and constant quasi-Fermi levels across the depletion region.

For very high solar concentrations (>1000 suns), the cell may be driven into high level injection in which case the basic semiconductor equations must be solved for both carrier types not just the minority carrier solution.

This focus on some of the weaknesses of the analytical approach should not be overstated. As will be indicated in the next few pages, several workers have had considerable success in applying an analytical or simple numerical analysis method in modeling cells. These models are useful in determining the sensitivity of terminal characteristics to parameter variations, but do not have the capacity to 'look' into the cell and examine the effect of those parameter variations on such quantities as carrier concentration and electric field. We now review some of these models.

Van der Plas, James, Moon, and Nelson

The Varian group described a modeling program in 1975 [7] which they used to optimize a heteroface concentrator cell. The user could specify up to 29 independent parameters in describing the cell. Essentially, the program calculated the generation in each layer and then applied the minority carrier transport equation. An interesting feature of this program is a subroutine which optimized the contact grid. The Varian group obtained good agreement between the computed cell characteristics and their experimental work when they applied it to an analysis of a heteroface cell with a relatively large $Al_xGa_{1-x}As$ window (1.2 μm), layers of uniform doping, and no minority carrier mirror at the rear of the cell. This is the type of structure for which the minority carrier analysis is expected to yield good results, particularly since GaAs cells may operate at quite high concentrations before going into high level injection. Thus, this program has the ability to describe the terminal characteristics of cells but but does not give the user access to detailed information about field quantities and carrier concentrations in the interior of the cell.

Konagai and Takahashi

Konagai and Takahashi described an analysis of a graded band-gap structure in a 1976 paper [15]. They assumed that the minority carrier diffusion equation applied and that the electric field in the $Al_xGa_{1-x}As$ layer was constant. In addition, they only treated cells which had layers of uniform doping and assumed that the electric field was zero in the quasi-neutral regions of the cell. This model also failed to consider any recombination in the space-charge region. Konagai and Takahashi examined a hypothetical cell and did not compare their calculated results with experimental data, however, their model did demonstrate the benefits of using a graded band-gap front layer. It is also interesting to note that Konagai and Takahashi used a window layer with a low Al fraction ($x < 0.3$). They cited lower contact resistances for low Al fraction as the reason for choosing this composition range. This is in contrast with the philosophy of most other designers who choose alloys with a high Al content for the window material so that the loss of carriers generated by high energy photons is reduced by reducing the number of carriers generated in the window layer.

<u>Tsaur and Milnes</u>

Tsaur and Milnes described a model for GaAs homojunction cells in 1972 [16] which included the effects of a position dependent electric field through the consideration of a non-uniform doping profile. Tsaur essentially used the minority-carrier diffusion equation which he recast into a form dependent on doping [16]:

$$\frac{d^2\Delta n}{dx^2} + \frac{d\Delta n}{dx}\left(\frac{1}{D_n}\frac{dD_n}{dN_A}\frac{dN_A}{dx} + \frac{1}{N_A}\frac{dN_A}{dx}\right) + \Delta n\left[\frac{1}{N_A}\frac{d^2N_A}{dx^2}\right.$$

$$\left. - \left(\frac{dN_A}{dx}\right)^2 \left(\frac{1}{N_A^2} - \frac{1}{D_nN_A}\frac{dD_n}{dx} - \frac{1}{D_n\tau_n}\right)\right]$$

$$+ \frac{1}{D_n}\int_0^{\lambda_c} \alpha(\lambda)\,(1-R(\lambda)\,N(\lambda)\,e^{-\alpha(\lambda)x}\,d\lambda = 0$$

This equation is solved subject to the boundary conditions:

$$\frac{d\Delta n}{dx} = \Delta n\left(\frac{S}{D_n} + \frac{q}{kT}(\vec{E})\right) \qquad \text{at } x = 0$$

$$\Delta n = 0 \qquad \text{at } x = x_j$$

by a fourth order Runge-Kutta method.

The spectral response curves calculated by these workers agreed well with experimental data, however, several material parameters were used in fitting the results. Later work by these authors [17] does not indicate that this approach was extended to heteroface or graded band-gap structures.

Lamorte and Abbott

Lamorte and Abbott discussed an computer program [18,19,20] for computing the terminal characteristics of cascade cells. They also made the minority carrier diffusion equation approximation, but went further in their assumptions, obtaining a closed form solution. Lamorte and Abbott applied this solution to the several layers of a cascade cell and used a computer program to optimize those layers. The assumptions which they indicated are as follow:

i) Mobility independent of position or some average value is used for each layer.

ii) The electric field is independent of position within a layer, in other words there is no band-gap grading and doping must have a uniform profile.

iii) Recombination in the space-charge region is negligible.

iv) Optical reflection and carrier recombination at the heterojunction interface are negligible.

As is expected this analysis does not yield detailed information about the interior of the cell. Lamorte and Abbott indicated that their analysis has shown good agreement (to within 5%) between calculated and measured efficiencies for one junction cells for which the above assumptions are reasonable.

Sutherland and Hauser

Sutherland and Hauser reported a variable composition analysis program in 1977 [21,22], which was a modification of a Si homojunction model by Dunbar and Hauser [23]. Their approach was the most complete of the models discussed in this review in that they numerically solved the basic one dimensional semiconductor equations; current transport, continuity and Poisson's equations. This program was capable of considering:

i) position dependent band-gap
ii) position dependent electron affinity
iii) built-in fields due to varying band-gaps
iv) composition dependent refractive index
v) heterojunction interface recombination
vi) position dependent mobility, dielectric constant and absorption

A weakness in this model was the application of Boltzmann statistics to carrier concentrations. Because of GaAs's low conduction band effective density of states this material may become degenerate at relatively low doping levels ($N_D \simeq 1\times10^{17}$) . Also of concern is the failure of this model to consider the effect that sheet resistance has on the characteristics of cells operated under high solar concentration. This model was the only one which we have discussed that demonstrated the ability to give the cell designer a view of the interior conditions of the cell.

1.2 Parameter compilation for GaAs cell modeling

Accurate values of mobilities, minority carrier lifetimes, doping profiles, etc. are required for device modeling. From the current literature, a list of the best available parameters for device modeling was compiled. GaAs materials models are described in detail in Chapter 2 of this report. Although electrical bandgap narrowing effects are not well-characterized in GaAs devices, theoretical calculations described in Chapter 2 lead us to expect that bandgap narrowing may be significant in heavily doped p-type GaAs but not in n^+ GaAs.

We also complied the optical parameters of materials used as anti-reflection coatings for GaAs cells. Two materials were considered, $Al_xGa_{1-x}As$ (considered as an AR coat for heteroface cells) and the native oxide for GaAs which is prepared by anodic oxidation. As discussed in Chapter 3, the data for $Al_xGa_{1-x}As$ throughout the composition range is scarce and the properties of the native oxide depend to some degree on the fabrication technique. For these reasons, we expected to encounter difficulties in modeling the spectral response of GaAs-based cells. Clearly, better measurements of the optical properties of such materials are required.

1.3 1-D Numerical Model Development

A one-dimensional solar cell simulation program (SCAP1D), in use at Purdue since 1979 [24,25,26], was modified for GaAs homojunction solar cell analysis by installing the materials models described in Chapter 2 and 3. The program has the capability to compute both dark and illuminated (low and high intensity) I-V and spectral response characteristics. Open-circuit voltage, short-circuit current, conversion and collection efficiencies, etc. can be computed by the program. A graphical analysis package, used to "observe" the internal operation of cells, allows the user to plot the physical quantities listed in Table 1 over any segment of the device. The device model resembles that of Sutherlan and Hauser in that it solves the basic semiconductor equations by finite difference techniques. A discussion of the numerical solution techniques is contained in Lundstrom's or Gray's thesis [24,26]. A brief user's manual for this program is contained in Appendix C of this report.

1.4 Device Model Verification

To test the device model, we chose the n^+p shallow homojunction cell reported by Fan and Bozler [4]. For this cell, a one-dimensional model should suffice. As detailed in Chapter 4, the model did a good job of simulating

Table 1.1 Plots Available from PLOT1D/SCAP1D

PLOT	DESCRIPTION
'carrier'	....carrier concentrations vs. position
'curden'	.....hole and electron current densities vs. position
'delpot'	.....change in potential (from equilibrium) vs. position
'doping'	.....doping density vs. position
'eband'	......energy band diagram
'efield'	.....electric field vs. position
'equasi'	.....hole and electron quasi-electric fields vs. position
'eeff'	.......the effective fields (electric plus quasi-electric) for holes and electrons
'gen'	........optical generation rate vs. position
'jp'	.........hole current density and components
'jn'	.........electron current density and components
'logexss'	....log of the excess carrier conc vs. position
'logrho'	.....log of the charge density vs position
'mob'	........mobility vs. position
'niplot'	.....ratio of ni/ni0, where ni0 is the intrinsic carrier
'potent'	.....potential vs. distance
'recrate'	....net recombination rate vs. position
'rho'	........charge density vs. position
	concentration in the absence of bandgap narrowing
'xcescar'	....excess carrier concentration vs. position

shallow homojunction cells. Some difficulties were encountered when modeling the cell's spectral response, but these were not unexpected given our limited knowledge of the optical properties of the AR coating.

We also exercised the device model by modeling a p^+n cell and a heteroface cell. For both of these p^+n cells, the model proved to be quite accurate. While the work described in Chapter 4 establishes some confidence in the model's accuracy, it should be stressed that model verification is never really complete. As comparisons between theory and experiment continue, the model will evolve and confidence in its accuracy will increase.

1.4 Demonstration of Heterostructure Modeling Capability

Several types of advanced solar cells (e.g. heteroface and cascade) require that the model be capable of analyzing cells with position-dependent material composition. Although the development of a complete heterostructure solar cell was not attempted in the course of this work, we did demonstrate the capability for such analysis. By coupling a heterostructure device model developed for transistor applications with our existing solar generation routines, we simulated a simple graded bandgap solar cell. By this method we studied a problem of current interest - the enhancement of open-circuit in graded bandgap solar cells. The results of this study are described in Chapter 5.

1.5 Summary and Conclusions

The major result of this year's efforts is a detailed, numerical device model for GaAs solar cells. Although our knowledge of the material parameters that control GaAs devices is far from complete, we have achieved good success in comparisons between theory and experiment. The continued use of this code in modeling various GaAs-based solar cells should help us identify weaknesses of the model while providing useful insight into cell operation.

CHAPTER 2

GaAs MATERIAL PROPERTIES AND MODELS

This chapter has as its purpose the compilation of material parameters and models for GaAs as they relate to solar cell device performance. Some parameters will simply be presented, as their values are generally agreed upon, while other parameters, such as the absorption coefficient and intrinsic carrier density, are of such importance and interest that they dictate a closer look at the physical mechanisms which underlie their existence. In general, all parameters will be given for 300 K unless otherwise specified.

Because many of the assumptions made when working with silicon have become almost second nature, this chapter will point out areas and applications for which these assumptions may not be made for gallium arsenide.

2.1 GaAs ... A Material Description

Gallium arsenide is a binary compound and as such, when compared with elemental compounds such as silicon and germanium, we expect additional features in the preparation and usage of the material to be important. One feature which is immediately recognized as being important is the stoichiometry of the material. How does the material respond if it is either Ga- or As-rich? Gallium arsenide is commonly grown by several widely varying techniques, liquid phase epitaxy (LPE), vapor phase epitaxy (VPE), molecular beam epitaxy (MBE), chemical vapor deposition (CVD), as well as from a melt. How do these various growth techniques affect the stoichiometry of the material and its physical properties?

Holmes et.al. [73] showed that the stoichiometry of the melt determined whether the GaAs grown in the liquid encapsulated Czolchralski (LEC) process was semi-insulating or low-resistivity and identified a critical arsenic composition of 0.475 for the melt. A deep donor level, EL2, is known to exist in GaAs [27] and, depending on the growth technique, either compensates impurities introduced in the melt or must be compensated for. As an example, material grown by the LEC method is thought to have a large acceptor concentration due to the introduction of carbon in the growth of the material. Holmes [73] associated an increase in the concentration of EL2 with an increase in the As atomic fraction and explained the semi-insulating nature of the As-rich GaAs as a compensation of the carbon acceptors by the EL2 donors. In contrast, material grown by the Bridgman technique is known to be n-type due to Si donors introduced during growth [28]. This requires that acceptors be

added to compensate for the shallow-donor states introduced by the Si and the deep levels associated with EL2. The impurity most commonly used is Cr which creates an acceptor state near the mid-gap.

Because of GaAs' zinc-blende lattice and the existence of two separate sublattices, one corresponding to gallium and the other to arsenic, it is not always clear what effect a given impurity will have on the carrier concentration of a sample. Will the impurity introduce donor states or acceptor states? Silicon, as an impurity in GaAs, illustrates this ambiguity well. If Si, a group IV element, substitutes for Ga, a group III element, it acts as a donor. However, if it substitutes for As, a group V element it will behave as an acceptor. Clearly, the frequently made approximations:

$$n \simeq N_D \tag{2.1.1}$$

or

$$p \simeq N_A \tag{2.1.2}$$

are questionable in this instance. The uncertainty concerning the type of state that a given impurity will introduce also indicates that the question of compensation should be addressed. The impurity concentration may be considerably higher than the free-carrier concentration, particularly for low carrier concentrations.

Other group IV materials also act in an ambiguous fashion in GaAs. Germanium is a shallow acceptor in LPE GaAs, primarily a donor in VPE GaAs, and shows no preference for one carrier type or another in melt grown GaAs [29]. Common dopants in GaAs device work and their ionization energies are listed in Table 2.1 [30].

Table 2.1 Common Dopant for GaAs

Impurities in GaAs		
Element	Type	Ionization Energy (eV)
S	donor	0.03
Te	donor	0.0061
Sn	donor	0.0058
Si	donor	0.0058
Ge	donor	0.0061
Sn	acceptor	0.17
Si	acceptor	0.0345
Ge	acceptor	0.0404
Zn	acceptor	0.0307
Be	acceptor	0.028
C	acceptor	0.026
Cr	acceptor	0.75
Mg	acceptor	0.0284
Mn	acceptor	0.113

No introductory overview of GaAs should be without a discussion of its bandstructure. More than any other contributing factor, it is the bandstructure of GaAs which makes it attractive for device work. Figure 2.1.1 illustrates the major features of the GaAs bandstructure. The most prominent of these being the direct bandgap at $\mathbf{k} = 0$. The direct bandgap makes the radiative transitions from the conduction band to the valence band much more favorable than in either Si or Ge. Thus, GaAs finds many useful applications in luminescing and lasing-type devices. It also is useful for sensitive photodetectors due to the sharp rise in the absorption coefficient for energies near the bandgap. For photovoltaic applications the direct band-gap and associated high absorption coefficients can be translated into high efficiency cells with thin absorption layers.

Finally, useful constants and material parameters are presented in Table 2.2. The parameter values incorporated in SCAP1d are those of Blakemore [31]. These were chosen as a set of consistent values which agreed well with those cited by other authors.

2.2 Carrier Statistics

Intrinsic Carrier Concentration

A frequently encountered quantity in semiconductor device modeling is the intrinsic carrier concentration, n_i. This quantity is often a component of the constants found throughout device modeling [32]. Thus, some effort should be expended in the determination of n_i. Much of the difficulty in the experimental

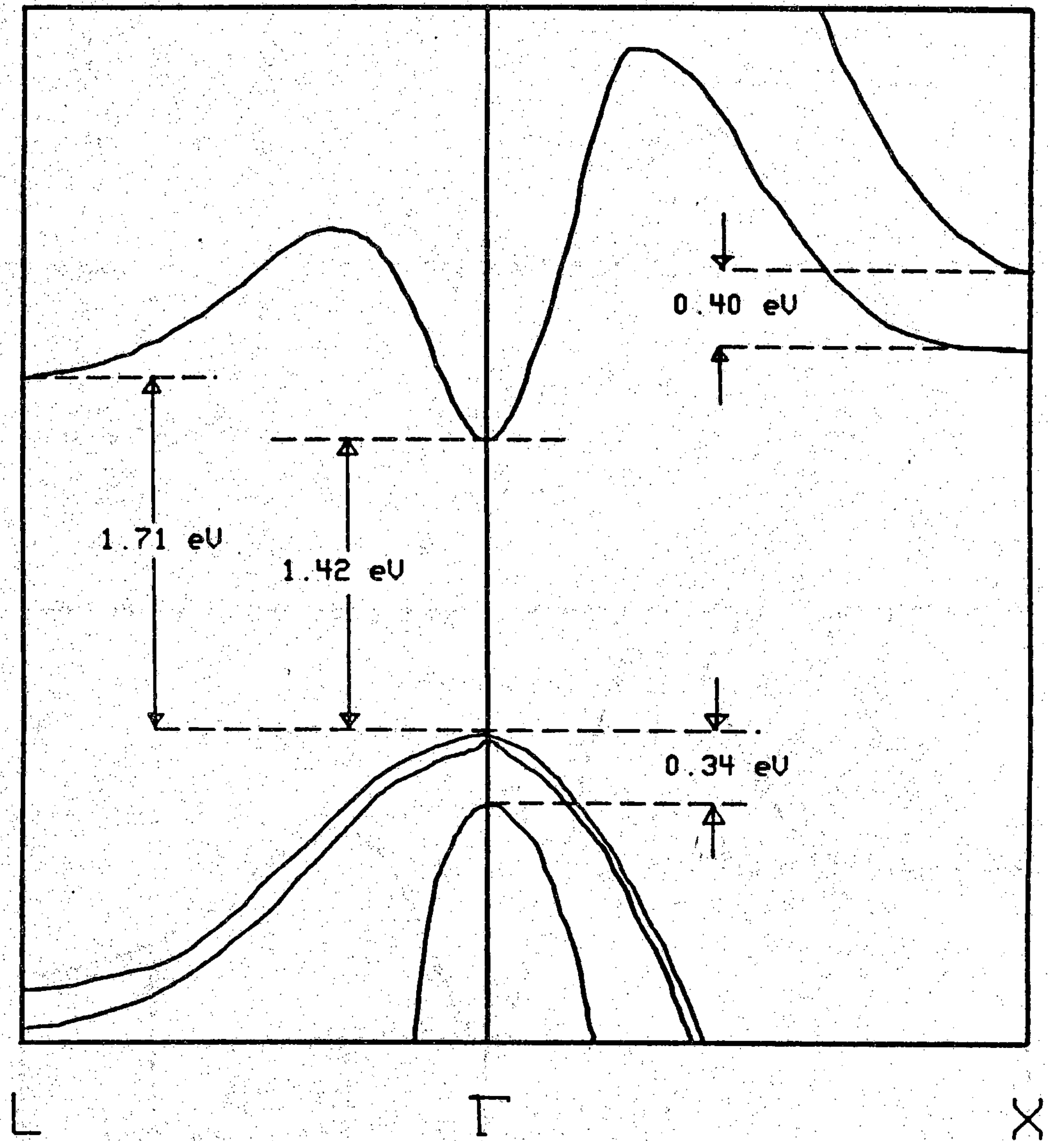

Figure 2.1.1 Gallium Arsenide Bandstructure

Table 2.2 **Material Constants for GaAs**

Useful Material Constants				
Parameters	*Sutherland*[74]	*Sze*[30]	*Blakemore*[31]	*Casey&Panish*[46]
E_{GL}	1.87	1.73	1.707	1.708
$E_{G\Gamma}$	1.439	1.423	1.424	
E_{GX}			1.899	1.900
ε_o	13.2	13.1	12.85	13.1
ε_∞	10.9		10.88	
m_p^*	0.68	0.47	0.53	0.48
m_Γ^*	0.0636	0.067	0.0632	0.067
m_L^*	0.811		0.55	0.55
$\mu_{p\,\max}$	380	400	320	
$\mu_{n\,\max}$	7200	8500	8000	
N_c		4.7e17	4.21e17	4.27e17
N_v		7.0e18	9.51e18	8.19e18

determination of $n_i(T)$ is due to the problems involved in growing intrinsic GaAs. However, semi-insulating GaAs generally displays free-carrier densities near those expected for intrinsic GaAs. The semi-insulating GaAs is commonly obtained by doping the material with chromium to compensate for native defects and impurities.

Blakemore [31] discussed a set of equations which can be used to model $n_i(T)$ based on the temperature dependence of the bandgaps, non-parabolicity of the bands, higher energy conduction bands, and mass parameters. He verified his method by comparing his results with those derived from the experimental results of Martin et.al. [33] concerning the absorption and emission coefficient of the Cr_{GA} deep level impurity.

Blakemore [31] developed the following equations for the temperature dependence of the carrier densities:

$$n_o = N_c^* \mathcal{F}_{1/2}(\eta_c), \qquad \eta_c = \frac{E_f - E_c}{kT} \tag{2.2.1}$$

and

$$p_o = N_v' \mathcal{F}_{1/2}(\eta_v), \qquad \eta_v = \frac{E_v - E_f}{kT} \tag{2.2.2}$$

$$\text{where} \quad \mathcal{F}_{1/2}(\eta_f) = \frac{\sqrt{\pi}}{2} \int_0^\infty \frac{\eta^{1/2} d\eta}{1 + e^{(\eta - \eta_f)}},$$

$$N_c^* = 8.63 \times 10^{13}\, T^{\frac{3}{2}} \left[(1 - 1.93 \times 10^{-4}\, T - 4.19 \times 10^{-8}\, T^2) + 21\, e^{\frac{-\Delta_{\Gamma L}}{kT}} + 44 e^{\frac{-\Delta_{\Gamma X}}{kT}} \right], \quad cm^{-3} \tag{2.2.3}$$

and

$$N_v' \simeq 1.83\times10^{15}\ T^{\frac{3}{2}}\quad cm^{-3} \tag{2.2.4}$$

Thus we readily see that:

$$n_i^2 = n_o p_o = N_c^*\ N_v'\, e^{-\frac{E_T}{kT}} \tag{2.2.5}$$

or

$$n_i(T) = \sqrt{N_c^*(T)\ N_v'(T)}\ e^{\frac{-E_T(T)}{2kT}} \tag{2.2.6}$$

Figures 2.2.1 and 2.2.2 compare the results for $n_i(T)$ assuming parabolic bands to those of the model presented here which includes non-parabolicity of the Γ - band and contributions from the upper conduction bands (X and L). As is evident from the figures, the extensive treatment of Blakemore is not required for GaAs at moderate to low temperatures (<1000 K). However, what we should recognize is that the method provides a means for analyzing materials such as $Al_xGa_{1-x}As$ over composition regions which support multi-band conduction.

np Product

In this section, we will discuss the **np** product as it relates to doping level and will show that the expression:

$$\mathbf{np} = n_i^2 \tag{2.2.7}$$

is not valid over a doping range which may be of interest to those working with photovoltaic devices. At high-doping levels a more rigorous calculation of the minority carrier density is required than is indicated by the simple

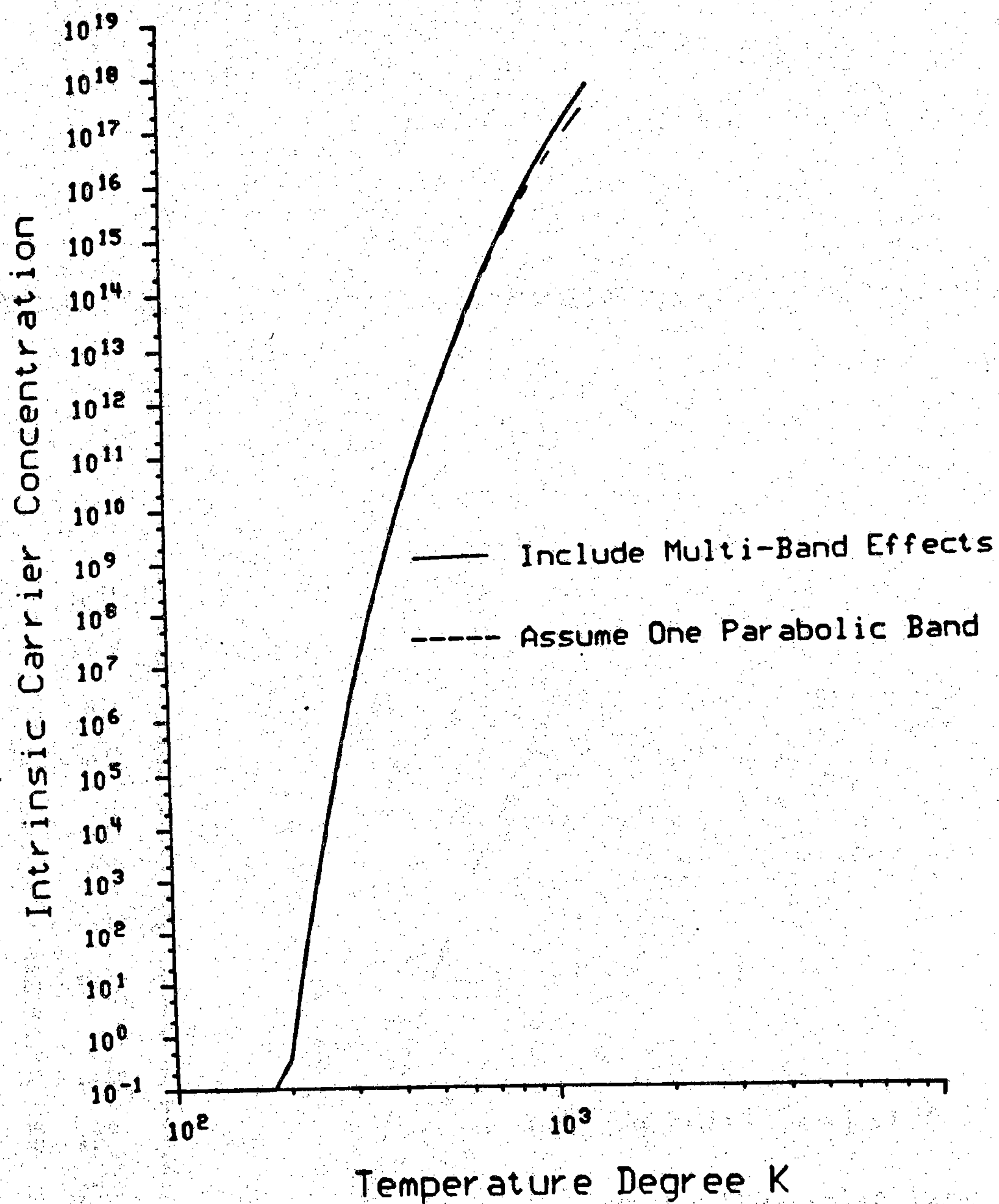

Figure 2.2.1 $n_i(T)$... T = 100 - 10 00 K

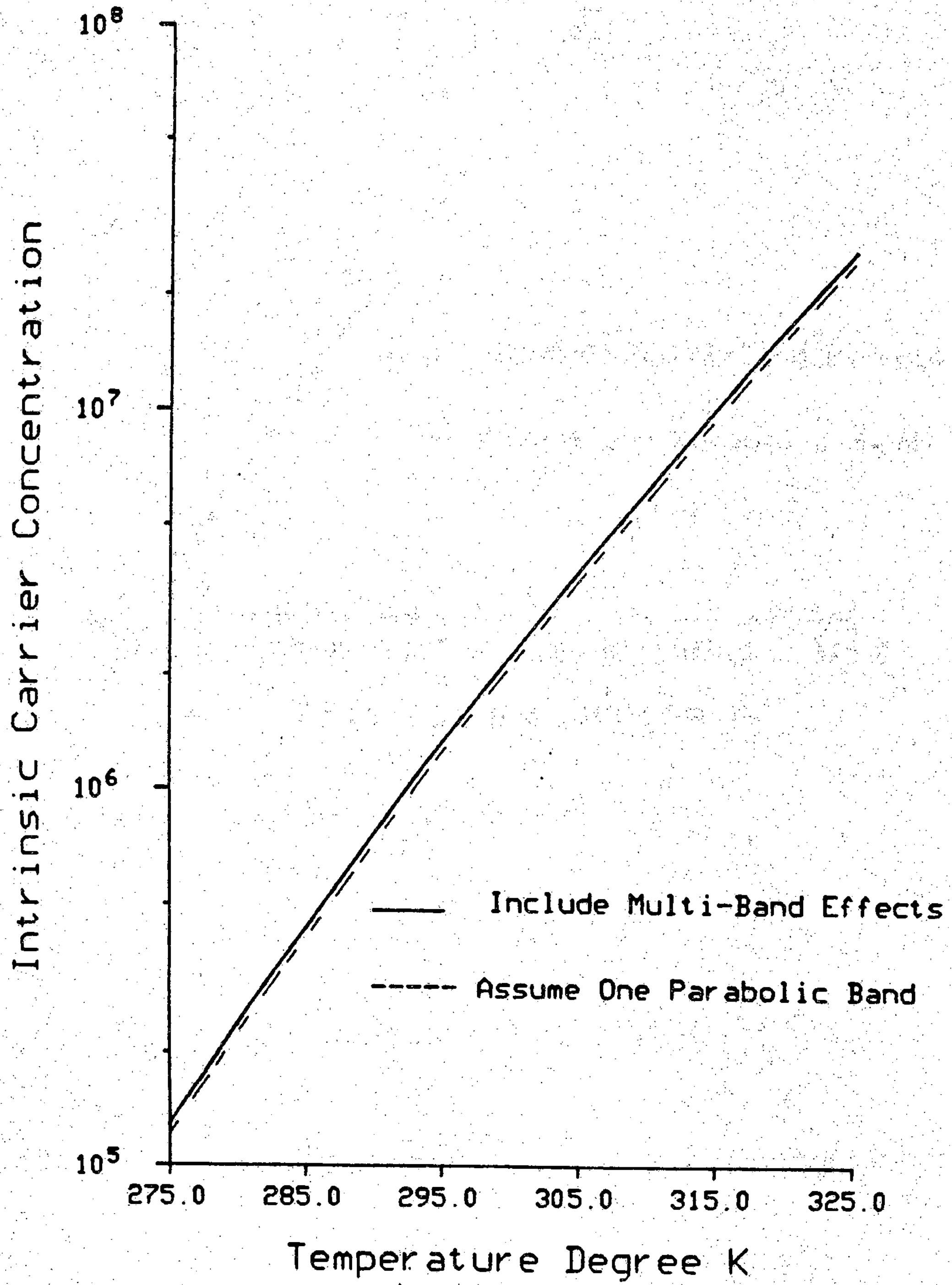

Figure 2.2.2 $n_i(T)$... T = 275 - 325 K

approximation:

$$p_{no} = \frac{n_i^2}{n_{no}}, \qquad n_{no} = N_D \tag{2.2.8}$$

The approximation $n_{no} = N_D$ is still valid assuming complete ionization and negligible compensation.

Heavy doping or high temperatures make consideration of the upper conduction bands necessary. For lack of data for these upper bands (and to simplify calculations) parabolic bands are assumed [31]:

$$n_\Gamma = N_{co}\left(\mathcal{F}_{1/2}(\eta_c) - \frac{15\alpha kT}{4E_\Gamma}\mathcal{F}_{\frac{3}{2}}(\eta_c)\right) \tag{2.2.9}$$

$$n_L = 2\left(\frac{2\pi\, m_L\, kT}{h^2}\right)^{\frac{3}{2}} e^{\frac{\eta_c - \Delta_{\Gamma L}}{kT}} \tag{2.2.10}$$

$$n_X = 2\left(\frac{2\pi\, m_X\, kT}{h^2}\right)^{\frac{3}{2}} e^{\frac{\eta_c - \Delta_{\Gamma X}}{kT}} \tag{2.2.11}$$

where N_{co} is the parabolic effective density of states for the Γ band:

$$N_{co} = 2\left(\frac{2\pi\, m_\Gamma\, kT}{h^2}\right)^{\frac{3}{2}} \tag{2.2.12}$$

and α is the non-parabolicity coefficient:

$$\alpha \simeq -(0.824 + 2.0\times10^{-5}\ T). \tag{2.2.13}$$

The total electron concentration in the conduction bands is simply:

$$n_o = n_\Gamma + n_X + n_L \tag{2.2.14}$$

For consideration at room temperature, the Boltzmann approximation for the upper conduction bands is quite reasonable, however, for higher temperatures, Fermi statistics may be required for the L-band. Figure 2.2.3 illustrates the distribution of the carriers over the Γ, X, and L bands, and Figure 2.2.4 shows the carrier concentration in each band.

Similarly for the valence band:

$$P_{lh} = 2\left(\frac{2\pi\, m_{lh} kT}{h^2}\right)^{\frac{3}{2}}\left[\mathcal{F}_{1/2}(\eta_v) - \left(\frac{15\beta kT}{E_\Gamma}\right)\mathcal{F}_{\frac{3}{2}}(\eta_v)\right] \tag{2.2.15}$$

$$P_{hh} = 2\left(\frac{2\pi\, m_{hh} kT}{h^2}\right)^{\frac{3}{2}}\mathcal{F}_{1/2}(\eta_v) \tag{2.2.16}$$

where

$$\beta \simeq -\left(3.87 - \frac{T}{1000}\right) \tag{2.2.17}$$

Equation 2.2.14 should not be interpreted as implying that the heavy-hole band is parabolic. In fact, the heavy hole band is quite anisotropic as well as being non-parabolic. This additional complication forces the approximation that m_{hh}^*, as experimentally determined is a measure of the average curvature of

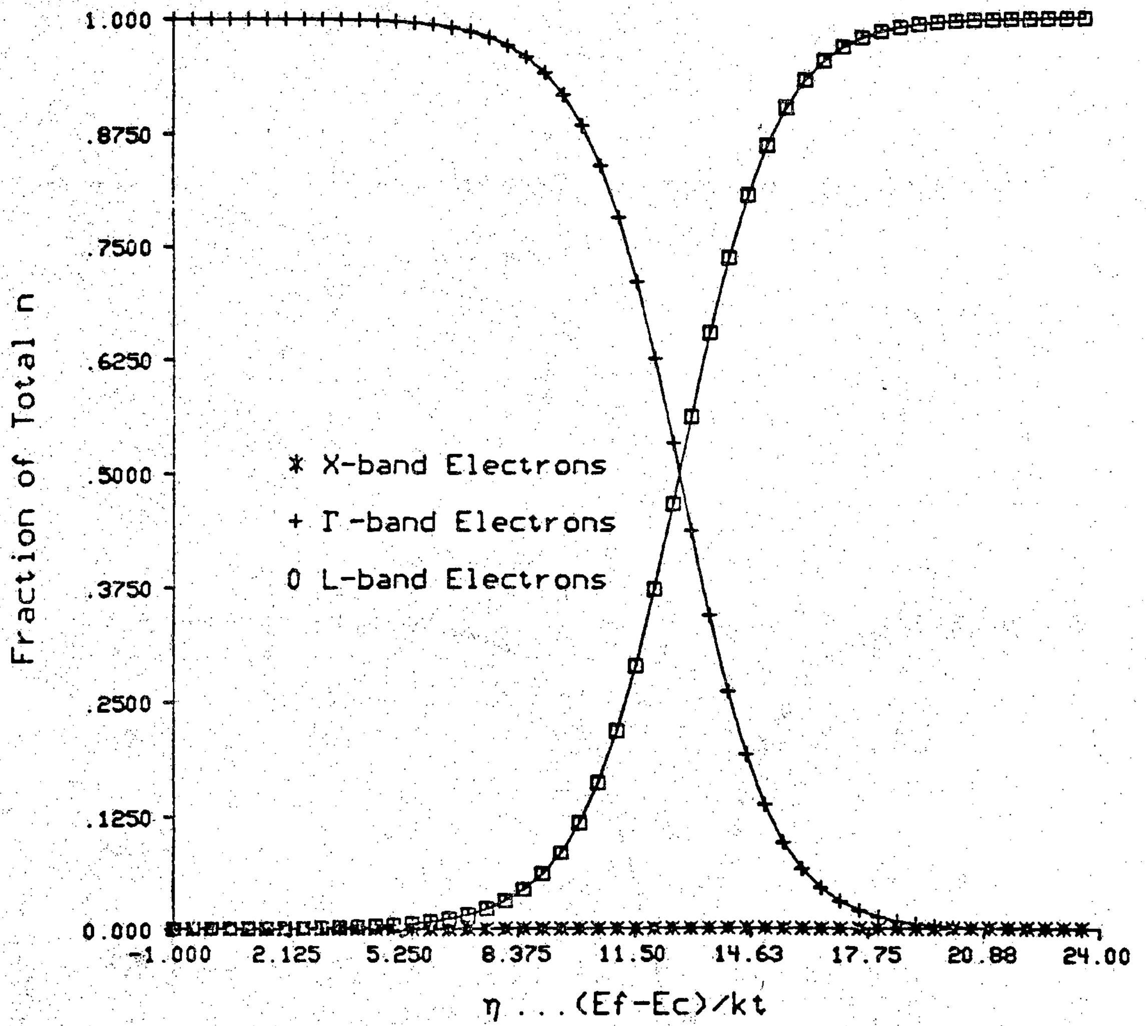

Figure 2.2.3 Distribution of Carriers Over the Γ, X, and L bands versus η_C

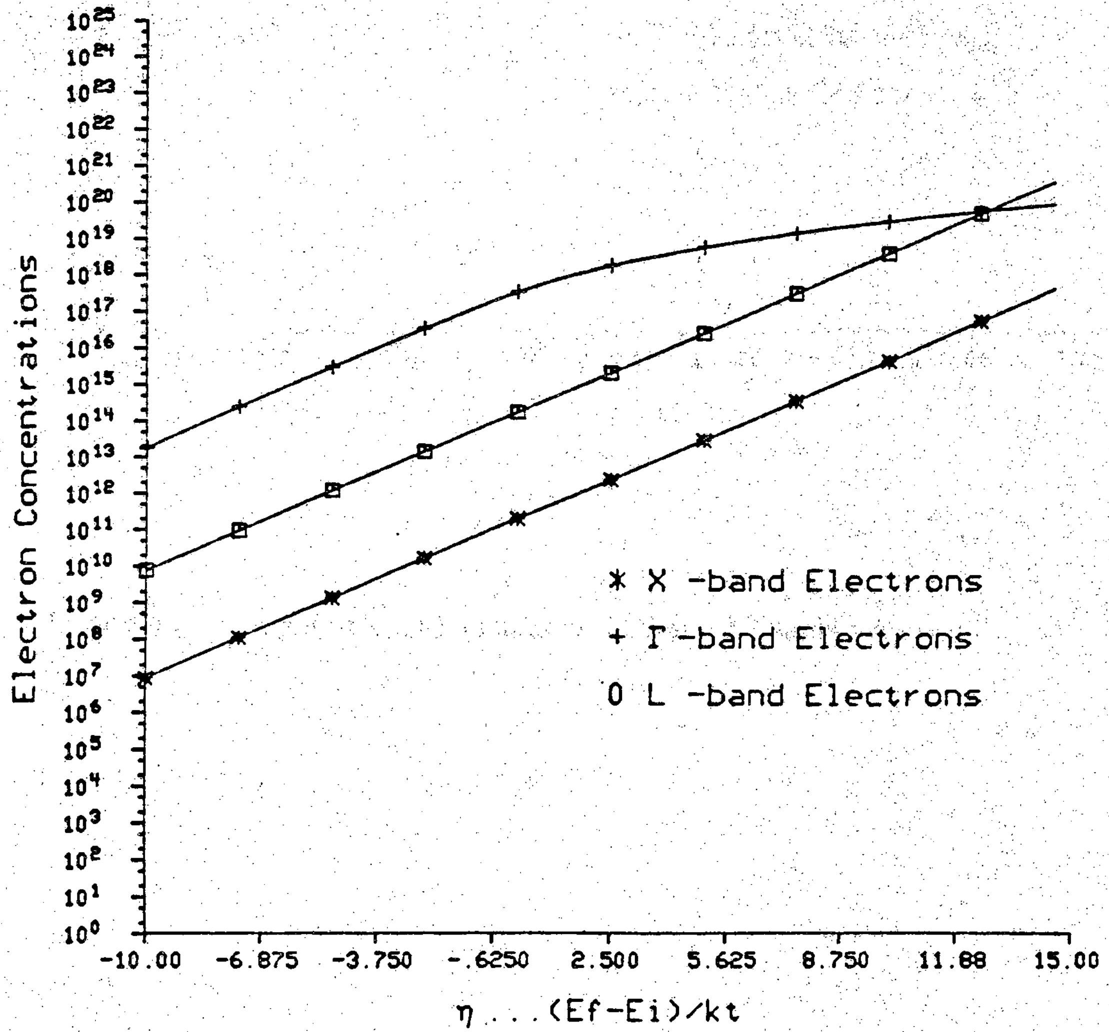

Figure 2.2.4 Carrier Concentrations in Γ,X and L bands versus η_C

the bands over the first 100 meV.

Making the assignment:

$$p_o = p_{hh} + p_{lh} \tag{2.2.18}$$

it is now a simple task (with the aid of a digital computer) to evaluate the variation of the **np** product with the Fermi level. The results are shown in Figure 2.2.5 for three different temperatures and compared with n_i^2 at those temperatures. This figure dramatically demonstrates the profound effect Fermi-Dirac statistics have on the **np** product. That is, Fermi-Dirac statistics serve to reduce the **np** product at heavy doping levels.

At present a model for n_i as discribed in eqs. (2.2.1-2.2.5) above is used in SCAP1D, however, no corrections have been made for Fermi statistics in the upper conduction bands for the GaAs code.

Bandgap Narrowing

It is well known that the analysis of Si solar cells containing heavily-doped regions is complicated by the necessity of considering the effect of heavy-doping on the band-gap. The current version of SCAP1D deals with this phenomenon for silicon cells. Are these effects observed in GaAs at room temperature? What effect does heavy doping have on the **np** product of GaAs?

Lee and Fossum [34] presented a recent treatment of band-gap narrowing in Si. In their calculations they included three major effects:

i) Many-body Effects- (optical gap shrinkage)

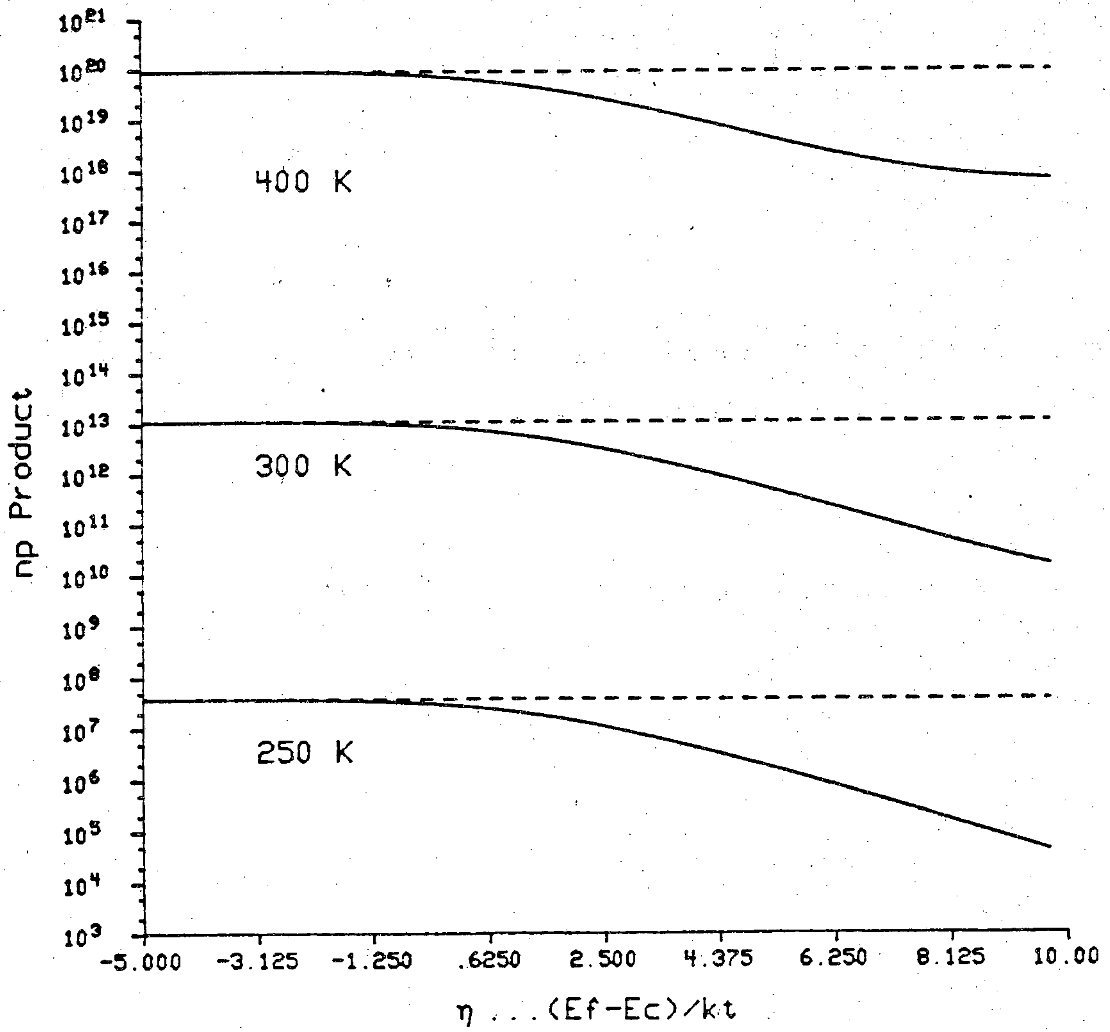

Figure 2.2.5 **np** Product versus η_C

ii) Kane Band-tails- accounts for change of local density of states

iii) Fermi-Dirac Statistics- required by the degeneracy of the majority carrier.

Recognizing that the Kane band-tails represent a worst case approximation for the distortion of the energy bands with heavy doping, we applied the model of Lee and Fossum [34] to GaAs.

The first step taken was to calculate the many body effects. The shift in the conduction band edge is given by:

$$\Delta E_{c_{mb}} = \frac{q^2}{4\pi^2 \epsilon_s} \Lambda K_{F_{ef}} \tag{2.2.19}$$

where

$$K_{F_{ef}}(T) = \left[\frac{8\pi^2 m_e^*(E_F - E_C)}{h^2}\right]^{1/2} \tag{2.2.20}$$

and Λ is chosen as 0.35.

Next the upward shift of the valence band was calculated using:

$$\Delta E_v^{mb} = \frac{5.07}{r_s^{3/4}} \left(\frac{m_{pc}^*}{m_e^*}\right)^{1/2} \tag{2.2.21}$$

where r_s is a dimensionless quantity determined by:

$$\frac{4}{3} \pi a_o^3 r_s^3 n_o = 1 \; ; \quad a_o = \frac{\epsilon_s h^2}{\pi q^2 m_e^*} \tag{2.2.22}$$

The sum of the two shifts was identified by Lee and Fossum as the optical gap shrinkage. These calculations agree well with the optically measured gap shrinkage for GaAs reported by Zverev et. al. [35].

The procedure for handling the Kane band-tails is a bit more involved. We can immediately write down the following relationship:

$$n_o = \int_{cb} \rho(E)\, f_{FD}(E-E_F)\, dE \simeq N_D \qquad (2.2.23)$$

$$p_o = \int_{vb} \rho(E) \left[1 - f_{FD}(E-E_F)\right] dE \qquad (2.2.24)$$

Kane [36] presented the following formula for the density of states in the band-tails:

$$\rho(E_{e,h}) \simeq \frac{8\pi(m_{n,p}{}^{*})^{\frac{3}{2}}\,(2^{\frac{3}{2}}\sigma)^{\frac{1}{2}}}{h^3}\; y\left(\frac{E_{e,h}}{2^{1/2}\sigma}\right) \qquad (2.2.25)$$

where

$$\sigma = q_2\left(\frac{n_o a_s}{8\,\pi\,\epsilon_s{}^2}\right)^{1/2} \qquad (2.2.26)$$

and

$$y(z) = \frac{1}{\pi^{1/2}} \int_{-\infty}^{z} (z-\xi)^{1/2}\, e^{-\xi^2}\, d\xi \qquad (2.2.27)$$

The screening length, a_s found in Eq. 2.2.25 is given by:

$$a_s = \left[\frac{q^2}{\epsilon_s}\,\frac{\partial n_o}{\partial(E_F - E_C)}\right]^{-1/2} \qquad (2.2.28)$$

and the function y(z) may be approximated by [34] :

$$y(z) \simeq \frac{1}{2\pi^{1/2}}\, e^{-z^2} \left\{1.225 - 0.906\left(1 - e^{2z}\right)\right\}; \qquad z \le 0.626 \qquad (2.2.29)$$

$$y(z) \simeq z^{1/2} \left[1 - \frac{1}{16z^2} \right]; \qquad z > 0.626 \tag{2.2.30}$$

In examining equations [2.2.22-2.2.29] it is evident that the Fermi level, E_F, must be determined. Since n_o is known, Eq. 2.2.22 seems a logical place to start. Note, however, that $\rho(E)$ depends on E_F through the screening length, a_s. Thus an iterative solution is required to determine E_F. Once E_F is found, calculation of p_o is straight-forward and the **np** product may be computed. Figure 2.2.6 illustrates our results and compares them to the **np** product ignoring band-gap shrinkage. Note the strong effect of Fermi-statistics on the **np** product. This effect is more pronounced in GaAs than for Si because of the large difference between the conduction and valence band density of states. From these results we predict that band-gap shrinkage should not be a source of degraded cell performance for GaAs cells with heavily doped n-type regions.

2.3 Mobility

In any discussion of material parameters in semiconductor device work, attention must be directed to a description of mobility. Stated simply, mobility is the ratio of the drift velocity of a carrier to the electric field which that carrier encounters:

$$\mu = \frac{E}{v_d} \tag{2.3.1}$$

and is measured in units of $cm^2/V{-}s$.

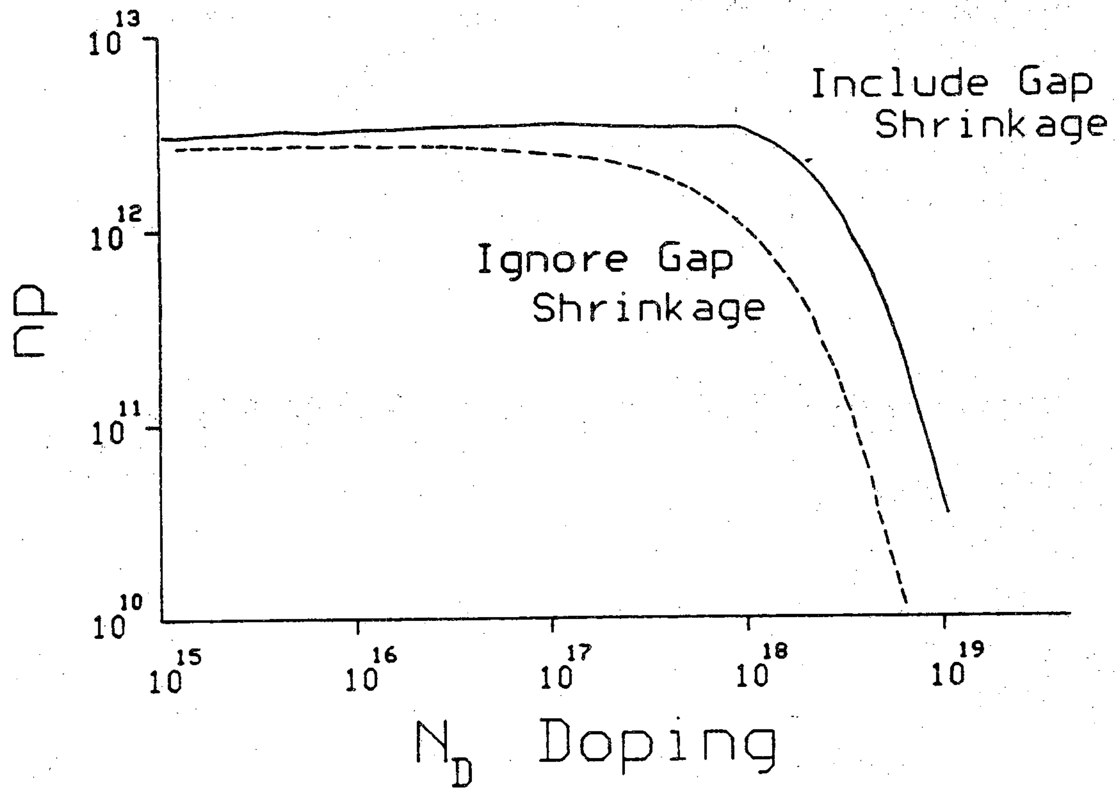

Figure 2.2.6 np Product versus N_D Including Heavy-Doping Effects

We usually work with two mobilities, the hole mobility, μ_p, and the electron mobility, μ_n. GaAs is a material with an exceptionally large electron mobility. This high mobility makes it particularly attractive for high-speed device work. A material parameter frequently specified by wafer suppliers is the resistivity of the sample. Resistivity, ρ, is related simply to the carrier mobilities by:

$$\rho = \frac{1}{e(\mu_n n + \mu_p p)} \qquad 2.3.2$$

Table 2.3 compares the electron and hole mobilities of GaAs with other frequently used semiconductors. A primary way in which mobility enters the equations modeling solar cells is through the minority carrier diffusion lengths:

$$L_n = \sqrt{D_n \tau_n} \qquad (2.3.3a)$$

or

$$L_p = \sqrt{D_p \tau_p} \qquad (2.3.3b)$$

Where D_n and D_p are the minority carrier diffusion constants and are related to the mobility through [30]:

$$D_{n,p} = \left(\frac{kt}{q}\,\mu_{n,p}\right) \frac{\mathcal{F}_{1/2}\left(\frac{E_F - E_C}{kT}\right)}{\mathcal{F}_{-1/2}\left(\frac{E_F - E_C}{kT}\right)} \qquad (2.3.4)$$

which reduces to the familiar Einstein equations for non-degenerate doping levels. From the equations above, its apparent that the small minority carrier lifetime could be a major factor in reducing the overall efficiency of a cell.

A more physical understanding of the phenomena of mobility is obtained

Table 2.3 Electron and Hole Mobilities of Common Semiconductors

Intrinsic Carrier Mobilities		
Semiconductor	Electrons	Holes
GaAs	8200	400
InAs	33000	460
InP	4600	150
Ge	4500	3500
Si	1300	500

Table 2.4 Caughey-Thomas Parameters Extracted from Walukiewicz

Electron Mobility (300 K) Caughey-Thomas Fit to Walukiewicz Calculations				
Θ	μ_{max}	μ_{min}	α	NREF
0.0	8200	2750	0.553	9.85e16
0.1	8200	2100	0.528	1.03e17
0.2	8200	1750	0.537	8.10e16
0.3	8200	1350	0.531	6.80e16
0.4	8200	1100	0.542	5.09e16
0.5	8200	800	0.539	3.89e16
0.6	8200	550	0.537	2.79e16
0.7	8200	400	0.554	1.74e16
0.8	8200	200	0.551	9.85e15
0.9	8200	100	0.594	4.02e15

from an examination of the following:

$$\mu = \frac{e}{m^*} <\tau_R> \tag{2.3.5}$$

where $<\tau_R>$, the effective momentum relaxation time is given by [125]

$$<\tau_R> = \frac{\int E\ \tau_R(E)\ g(E)\ f(E)dE}{\int E\ g(E)\ f(E)dE} \tag{2.3.6}$$

g(E)....density of states

f(E)....occupation probability

The momentum relaxation time is determined by several mechanisms, the most important of these are acoustical phonon scattering, impurity scattering and optical phonon scattering. Each scattering mechanism has a scattering rate dependent on energy and can be combined to determine $\tau_R(E)$ by the following:

$$\frac{1}{\tau_R(E)} = \frac{1}{\tau_{imp}(E)} + \frac{1}{\tau_{ac}(E)} + \frac{1}{\tau_{opt}(E)} \tag{2.3.7}$$

This expression should not be confused with Mathiesen's rule:

$$\frac{1}{\mu} = \frac{1}{\mu_{imp}} + \frac{1}{\mu_{ac}} + \frac{1}{\mu_{opt}} \tag{2.3.8}$$

It is well known that Mathiesen's rule for combining mobility contributions is inaccurate, but it is still frequently used and has been the subject of some disagreement in recent years [37-40]. Walukiewicz [41] showed that there was considerable error in using equation [2.3.8], particularly for a doping range of interest in solar cell work.

Each of the scattering mechanisms dominates over a particular range of temperature, impurity scattering at low temperatures and optical phonon scattering at high temperatures. In comparing the temperature dependence of mobility with that of silicon it has been observed that acoustical phonon scattering does not play the dominant role that it does in silicon. This is consistent with our knowledge of the polar nature of GaAs.

When considering experimental or published data it is important to determine if the mobility is the drift mobility or the Hall mobility. Frequently, Hall mobility data may be presented simply as the mobility without specifying whether it is drift or Hall mobility. Often Hall data is used in conjunction with resistivity measurements to determine doping levels. Great care must be exercised in the analysis of this data for GaAs because of the frequently high levels of compensation found in this material.

The Hall mobility is related to the drift mobility by the Hall factor r_H :

$$r_H \mu = \mu_H \tag{2.3.9}$$

The Hall factor is equal to 1.0 only when all of the carriers have the same velocity or energy. We can force r_H to 1.0 by using a large **B** field such that $\omega_c \tau >> 1$ where ω_c, the cyclotron frequency, is given by:

$$\omega_c = \frac{\mathbf{B}e}{m^*} \tag{2.3.10}$$

At these high **B** fields all carriers move in closed orbits and drift at right angles to both the **B** field and the Hall field, $\mathbf{E}_H$.

The Hall coefficient, R_H, is written as:

$$R_H = \frac{\frac{-r_n}{en}(ne\mu_n)^2 + \frac{r_p}{ep}(pe\mu_p)^2}{[ne\mu_n + pe\mu_p]^2} \tag{2.3.11}$$

$$= \frac{-r_n n\,(\mu_n)^2 + r_p p\,(\mu_p)^2}{e\,[n\mu_n + p\mu_p]^2}$$

Blakemore [31] gives $r_n = 1.175$ and $r_p = 1.25$. A commonly made approximation is that $r_n = r_p$ which yields the following expression:

$$R_H = \frac{-r}{e}\left(\frac{nb^2 - p}{nb^2 + p}\right), \quad b = \frac{\mu_n}{\mu_p} \tag{2.3.12}$$

This approximation leads to negligible error if the material is n-type or nearly intrinsic. Note that this expression includes only free carrier densities. Large impurity concentrations would cause the Hall measurement to indicate a smaller free carrier density than actually exists in the sample. This is clearly a possibility when we are working with near intrinsic or high resistivity samples.

Walukiewicz [41] addressed the problem of compensation and its effect on mobility. He used a variational technique and included piezo-electric, acoustic phonon, screened polar, and screened ionized impurity scattering. Although, Walukiewicz had good results in comparing his theoretical calculations with measured data, his technique is computationally unwieldy for device modeling.

Walukiewicz presented his calculated values for mobility versus free-carrier concentrations for ten different compensation ratios ($\Theta = N_A^+/N_D^-$). We extracted Caughey-Thomas [42] parameters from each curve and present them in Table 2.4. The Caughey-Thomas empirical mobility model is given as:

$$\mu = \frac{\mu_{max} - \mu_{min}}{1 + \left[\dfrac{n}{NREF}\right]^{\alpha}} + \mu_{min} \qquad (2.3.13)$$

where n is the free electron concentration and μ_{max}, μ_{min}, NREF, and α are the parameters which must be chosen to fit the data.

To test the validity of these expressions for the extracted parameters, it should be straightforward to regenerate the Walukiewicz curves using the Caughey-Thomas formula and expressions 2.3.14-2.3.16. Figure 2.3.1 illustrates our success in reproducing the Walukiewicz mobility curves. Note that Walukiewicz's calculations are fit quite well by the Caughey-Thomas expressions, even though one of the adjustable parameters, μ_{max}, was fixed at 8200. However, we still are left with a problem in using this model. How do we determine the compensation ratio? Walukiewicz suggests using his tabulated data for that purpose and that was the course which we followed. Appendix A contains a source listing for a program (COMP.CAL) external to SCAP1D which does a two dimensional interpolation of the Walukiewicz data using the IMSL routine ICSCCU. The user need only supply the free-carrier concentration and the mobility. It will be interesting to compare the results of the determination of Θ from Hall effect measurements to those obtained using the COMP.CAL program and Walukiewicz's data. Stillman [43] discussed some of the problems in determining doping levels in epitaxial layers and indicated that the use of Hall data could lead to sizeable errors for doping levels above 10^{16} cm^{-3} due to the contribution of impurity conduction.

All of the parameters were fit with relatively simple expressions, although we did use third order polynomials to fit the parameters for $\Theta \leq 0.2$.

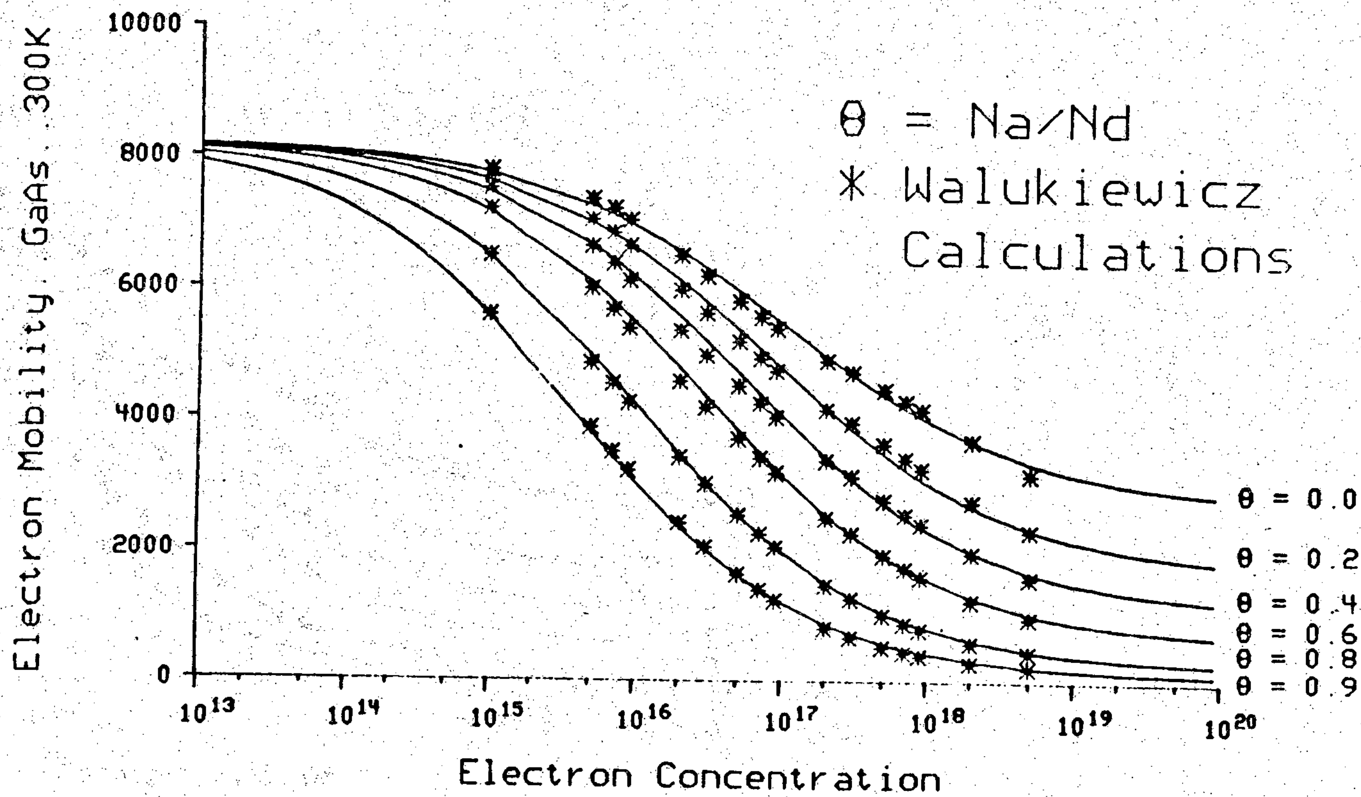

Figure 2.3.1 Electron Mobility versus Electron Concentration for Several Compensation Ratios

The parameter NREF was fit with the following set of equations:

$$\text{NREF} = 9.63\times10^{18}\,\Theta^3 - 4.2\times10^{18}\,\Theta^2 + 3.7\times10^{17}\,\Theta \qquad (2.3.14a)$$

$$+\ 9.85\times10^{16}; \qquad \Theta \leq 0.2$$

$$\text{NREF} = 10^{[17.07(1-\Theta)^{0.04}]}; \qquad \Theta > 0.2 \qquad (2.3.14b)$$

Figure 2.3.2 illustrates the quality of the fit to the extracted parameters.

The parameter μ_{min} was fit with:

$$\mu_{min} = -16500\,\Theta^3 + 17450\,\Theta^2 - 8080\,\Theta + 2750; \quad \Theta \leq 0.2 \qquad (2.3.15a)$$

$$\mu_{min} = 2349\,(1-\Theta)^{1.45}; \qquad \Theta \geq 0.2 \qquad (2.3.15b)$$

A plot of μ_{min} versus Θ is shown in Figure 2.3.3.

The parameter which shows the greatest amount of scatter (as seen in Fig. 2.3.4) is α. A simple least-squares linear fit yields:

$$\alpha = 0.53 + 0.03\,\Theta \qquad (2.3.16)$$

Walukiewicz's original paper [41] dealt with electron mobility in n-type material. He later extended his work to an analysis of electron mobility in p–type GaAs. The same equations may be used to determine the mobility in p-type GaAs if we make the following assignments:

$$p = \text{free–carrier concentration} \qquad (2.3.17a)$$

$$\Theta_p = \frac{N_D^{\ +}}{N_A^{\ -}} \qquad (2.3.17b)$$

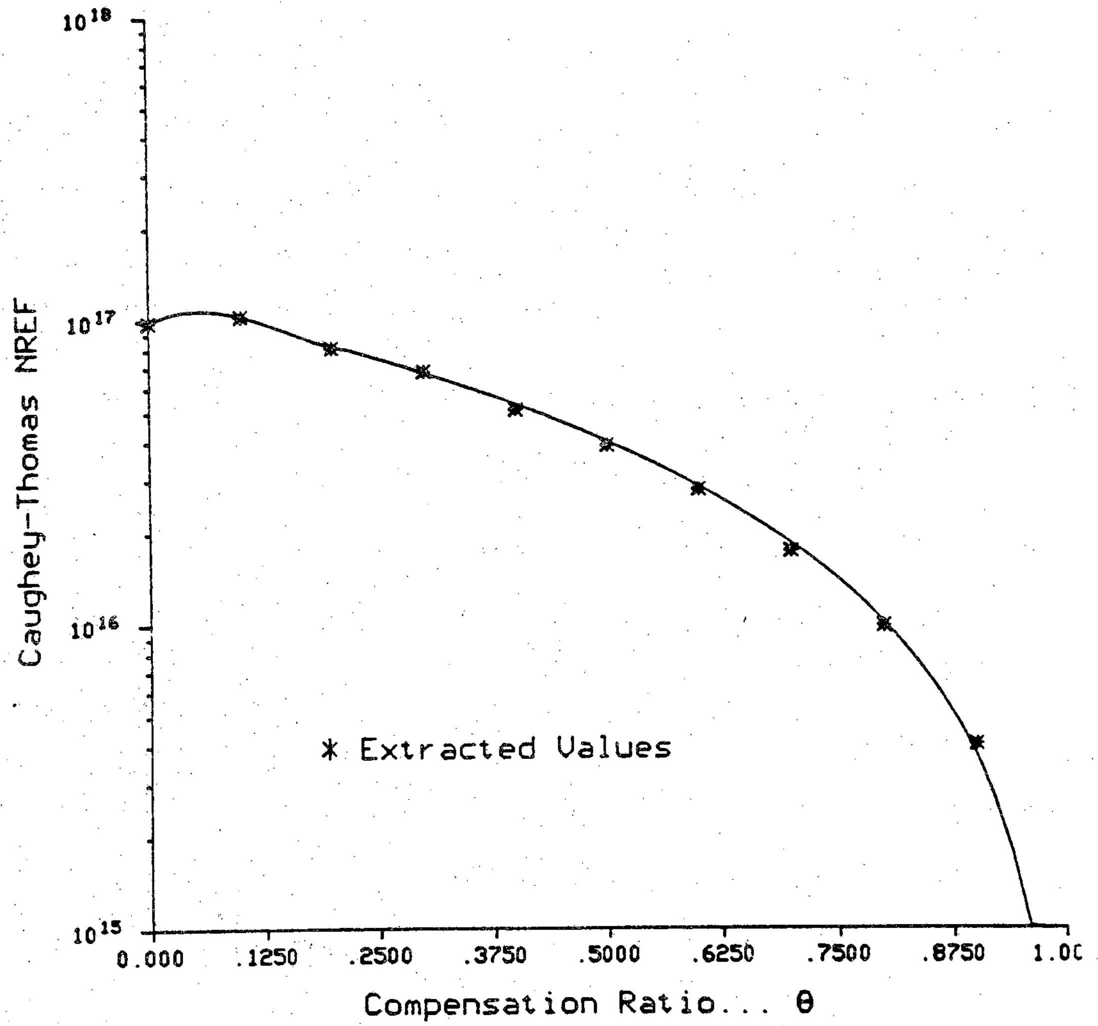

Figure 2.3.2 Fit of NREF (Θ) to Extracted Parameters

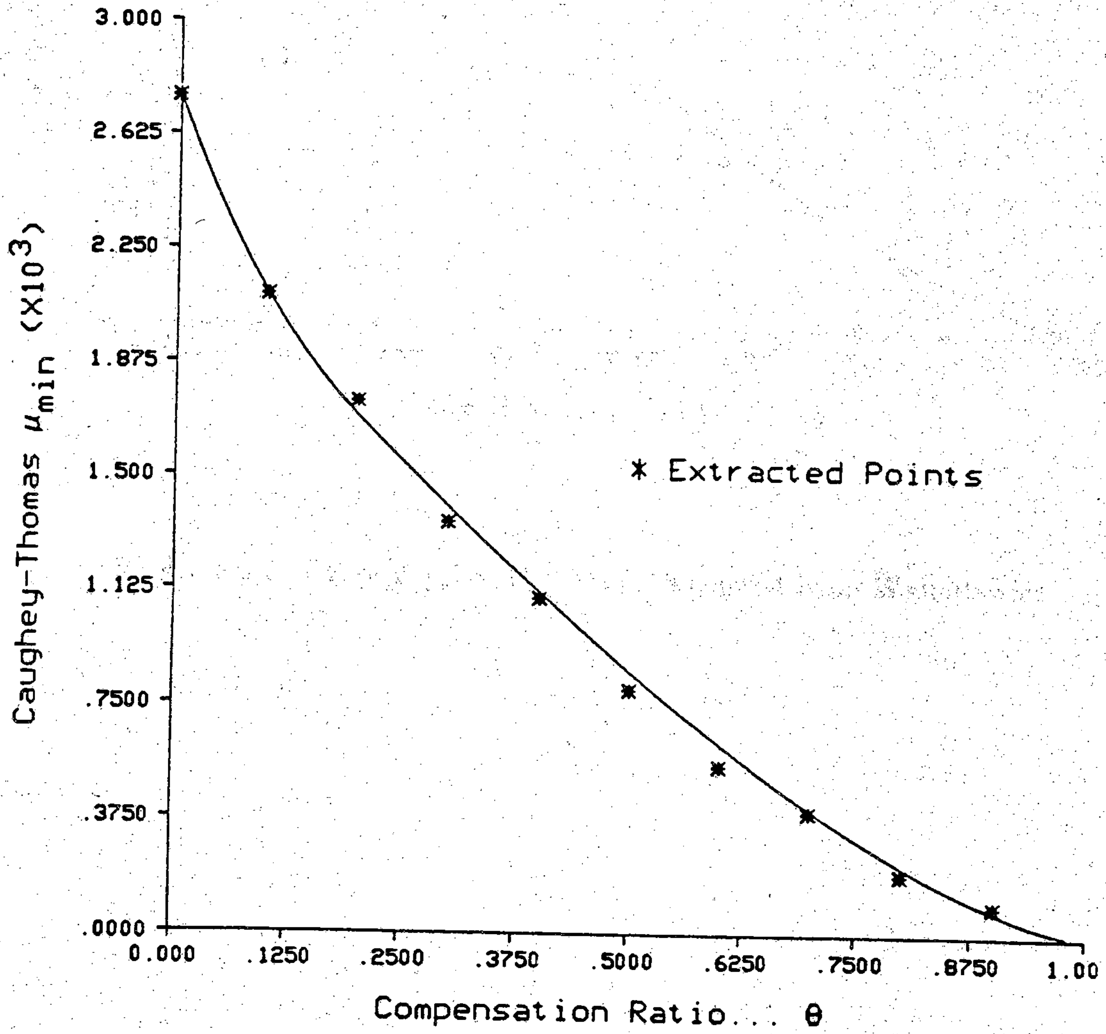

Figure 2.3.3 Fit of $\mu_{min}(\Theta)$ to Values Extracted from Walukiewicz

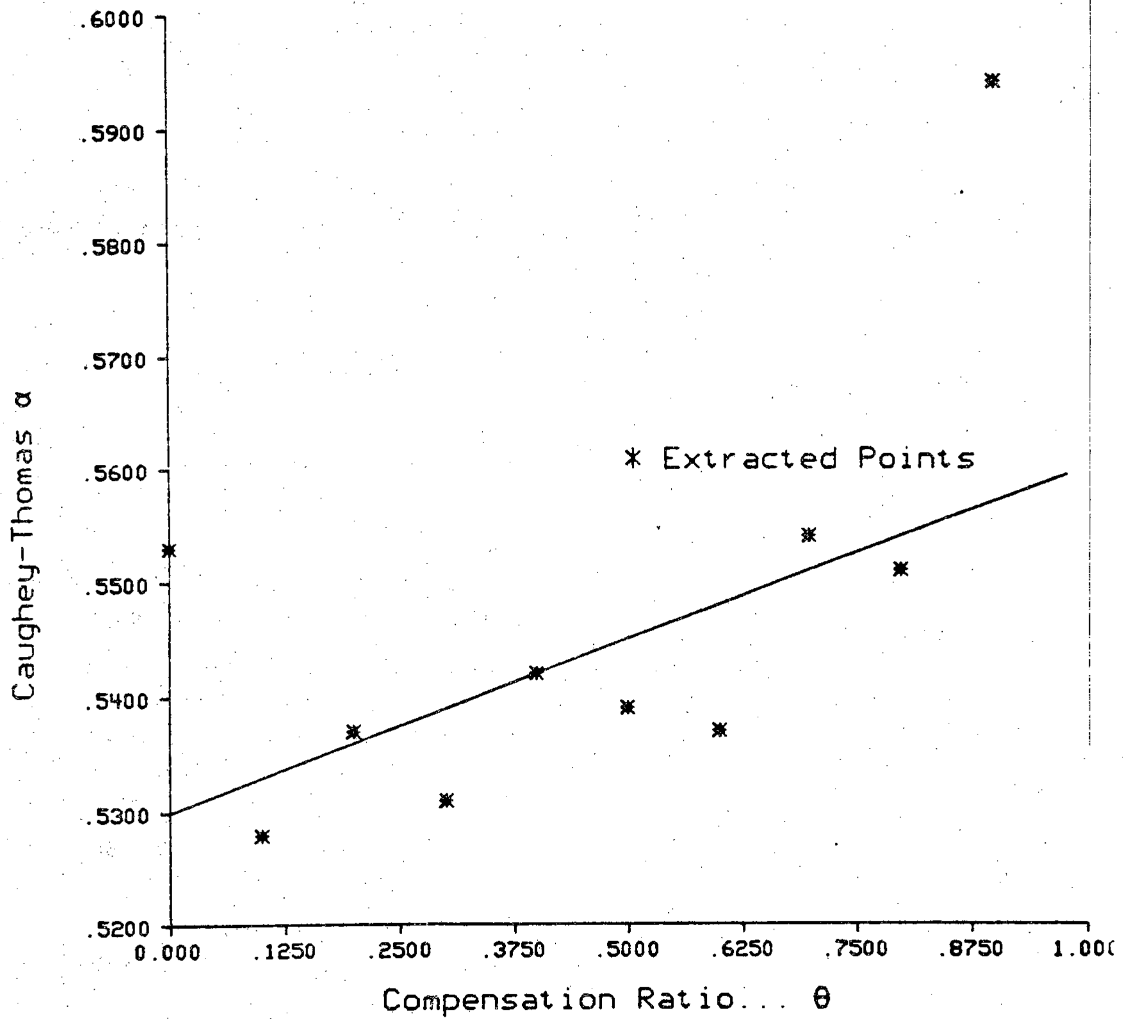

Figure 2.3.4 Fit of $\alpha(\Theta)$ to Values Extracted from Walukiewicz

$$\Theta = \frac{1 + \Theta_p}{3 - \Theta_p} \tag{2.3.17c}$$

The hole mobility in p-type GaAs is simply modeled using a Caughey-Thomas fit to data found in Sze [30].

$$\mu_p = \frac{\mu_{p_{max}} - \mu_{p_{min}}}{1 + \left(\frac{p}{PREF}\right)^{\alpha}} + \mu_{p_{min}} \tag{2.3.18}$$

$$= \frac{315}{1 + \left(\frac{p}{1.56 \times 10^{17}}\right)} + 70$$

Compensation was not considered in the model for hole mobility because of a lack of available data. In addition, the small range and magnitude of hole mobility as compared to electron mobility seems to justify this simplification. Finally, we must consider temperature effects on mobility. Blakemore [31] suggests using (as a first approximation):

$$\mu(T) = \mu(300\text{ K}) \left(\frac{300}{T}\right)^{2.3} \tag{2.3.19}$$

Although this is a crude approximation it should work reasonably well for temperatures near room temperature. A more careful study of the mobility limiting mechanisms should be made before applying the model to very high temperatures ($> \sim 400$ K).

2.4 Absorption

Certainly the absorption coefficient, one of the most important material parameters in the determination of a solar cell's performance characteristics, needs to be adequately described and modeled. For application to solar cell analysis, we require a model for the absorption coefficient which covers the spectral range 0.2μm - 6.0μm (6.2ev-0.21ev). This range represents the portion of the AM0 spectrum which has a flux density greater that 2.0 watts/m^2/μm . Portions of the spectrum outside of this range have an insufficient number of photons to contribute to the potential photocurrent. Examination of the dominant absorption mechanisms for GaAs will indicate that wavelengths longer than 1 μm may be disregarded with little impact on calculated cell performance.

If a monochromatic beam of light irradiates a homogeneous absorbing media and the intensity of that light is measured as a function of distance from the surface, the light intensity would be represented by:

$$\frac{-d\Phi(\lambda,x)}{dx} = \alpha(\lambda)\Phi_o(\lambda) \qquad (2.4.1)$$

which has the solution:

$$\Phi(\lambda,x) = \Phi_o(\lambda)e^{-\alpha(\lambda)x} \qquad (2.4.2)$$

where α is the absorption coefficient and is the reciprocal of the extinction length or the length in which the intensity of the radiation falls to 1/e of the incident radiation.

Generalizing Eq. 2.4.1 for cases involving position dependent absorption coefficients [22]:

$$\frac{-d\Phi(\lambda,x)}{dx} = \alpha(\lambda,x)\,\Phi(\lambda,x) \qquad (2.4.3)$$

or

$$\Phi(\lambda,x) = \Phi(\lambda,0)\, e^{-\int_0^x \alpha(\lambda,\xi)\, d\xi} \qquad (2.4.4)$$

It is readily seen that this position dependence of the absorption coefficient has a profound effect on the analysis of heterostructure devices.

The absorption coefficient is related to the extinction coefficient, $\mathbf{k}$, (the imaginary portion of the complex refractive index, n_c) by the following:

$$\alpha = \frac{4\pi\nu\mathbf{k}}{c} \quad cm^{-1} \qquad (2.4.5)$$

where c is the speed of light in vacuum.

When using the complex refractive index, n_c, it is often more convenient to work with the extinction coefficient, rather than the absorption coefficient, as is the case when describing reflection from surfaces of absorbing media.

Absorption Mechanisms

Because of GaAs's importance as an optoelectronic material, a great deal has been written about the various absorption mechanisms which are seen in this compound, such as lattice, phonon, free-carrier, impurity, and inter-band absorption. The most extensively studied regions of the spectrum appear to be the infra-red and near-bandgap. Although the mechanisms of absorption in the infra-red are interesting in and of themselves,we must beware of becoming too

involved in detail which has little bearing on the performance of photovoltaic devices.

In this spirit, we will limit our discussion to free-carrier, impurity, and interband absorption showing in the process that the interband process is by far the most important.

Free-Carrier Absorption

Free-carrier absorption is generally considered a loss mechanism in optoelectronic processes. This mechanism reduces the photon population without generating carriers. In this process, an electron absorbs a photon by making a transition to a higher energy state in the same conduction band valley as in Figure 2.4.1. It is obvious that another interaction is required to conserve momentum. This change in momentum can come about through the electrons' interaction with optical phonons, acoustical phonons and screened ionized impurities. It is interesting to note that these are also the primary interactions which determine a material's transport properties.

There have been several elaborate discussions of the interactions mentioned above and their relationship with free carrier absorption [44,45], but for our purposes free carrier absorption may be described by [31]:

$$\alpha_{FC} = A(n_o)\, n_o\, \lambda^3 \tag{2.4.6}$$

where n_o is the electron concentration. Casey and Panish [46] give the relationship for the free-carrier absorption near the bandgap as:

$$\alpha_{FC} \simeq 3\times10^{-18} n_o + 7\times10^{-18} p_0 \tag{2.4.7}$$

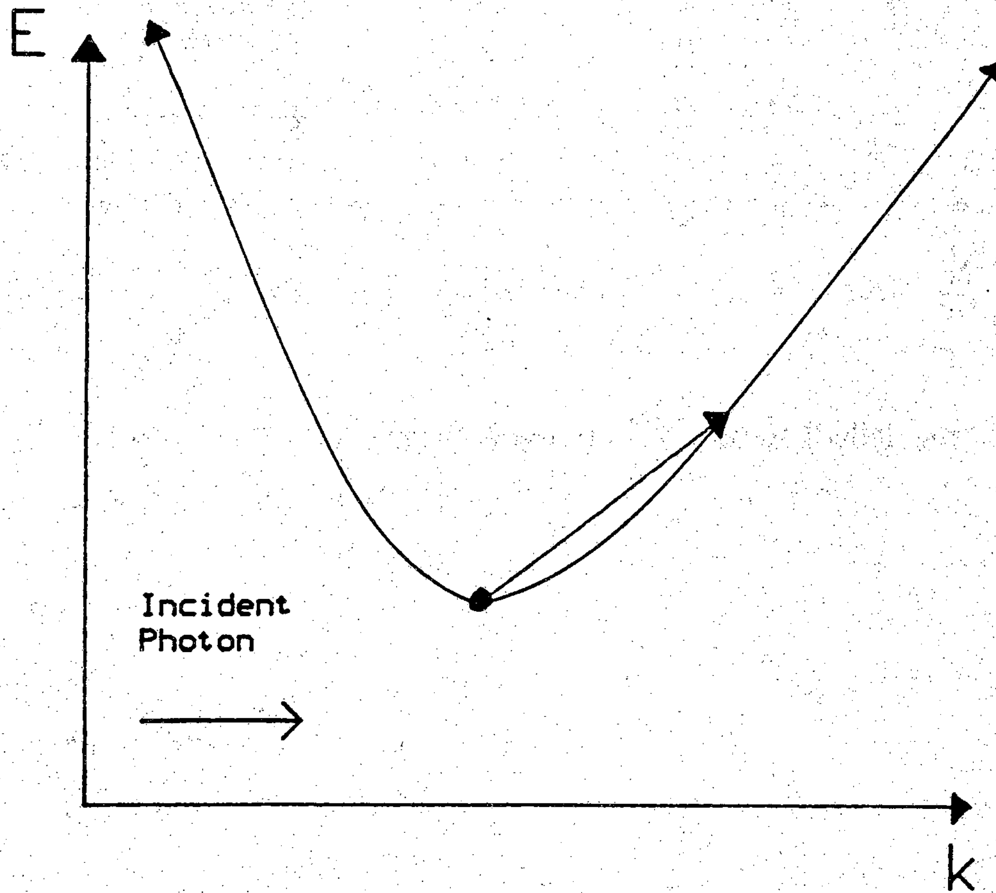

Figure 2.4.1 Free Carrier Absorption of Incident Radiation

Blakemore [31] suggests using:

$$\alpha_{FC} = 7.5\times10^{-20} n_o \lambda^3 \qquad (2.4.8)$$

for $\lambda > 4\mu m$.

Perhaps one of the most interesting approaches was that of Walukiewicz, et.al. [41]. Their interest in free-carrier absorption was in its potential application for determining the compensation ratio ($\Theta = N_A/N_D$) of a sample. They used an approach for calculating α_{FC} based largely on the work of Haga and Kimura [47] and had remarkable success in correlating their theoretical calculations with experiment.

The work of Spitzer and Whelen [48] illustrates not only the free-carrier absorption mechanism described above, but also the optically assisted transitions to upper conduction band minima. Those optically assisted transitions are indicated by the relatively constant absorption coefficients from ($1.0\mu m - 4.0\mu m$) in Figure 2.4.2. Note the expected increase in absorption with increased doping. Blakemore [31] observed that this phenomenon was readily described by:

$$\alpha_{Opt.Asst.} \simeq 6\times10^{-18}\, n_o \quad cm^{-1} \qquad (2.4.7)$$

This can be a significant mechanism for high doping levels and may be the dominant mechanism from the intrinsic absorption edge to $\lambda = 4\ \mu m$ where free carrier absorption becomes dominant.

Because, in GaAs, the first band-to-band transistions are direct ones with their associated high absorption coefficients (~ 1.0e4) and abrupt absorption edge, free carrier absorption is not found to be a competitive process. This is in contrast to the case of Si and Ge for which indirect transitions with their

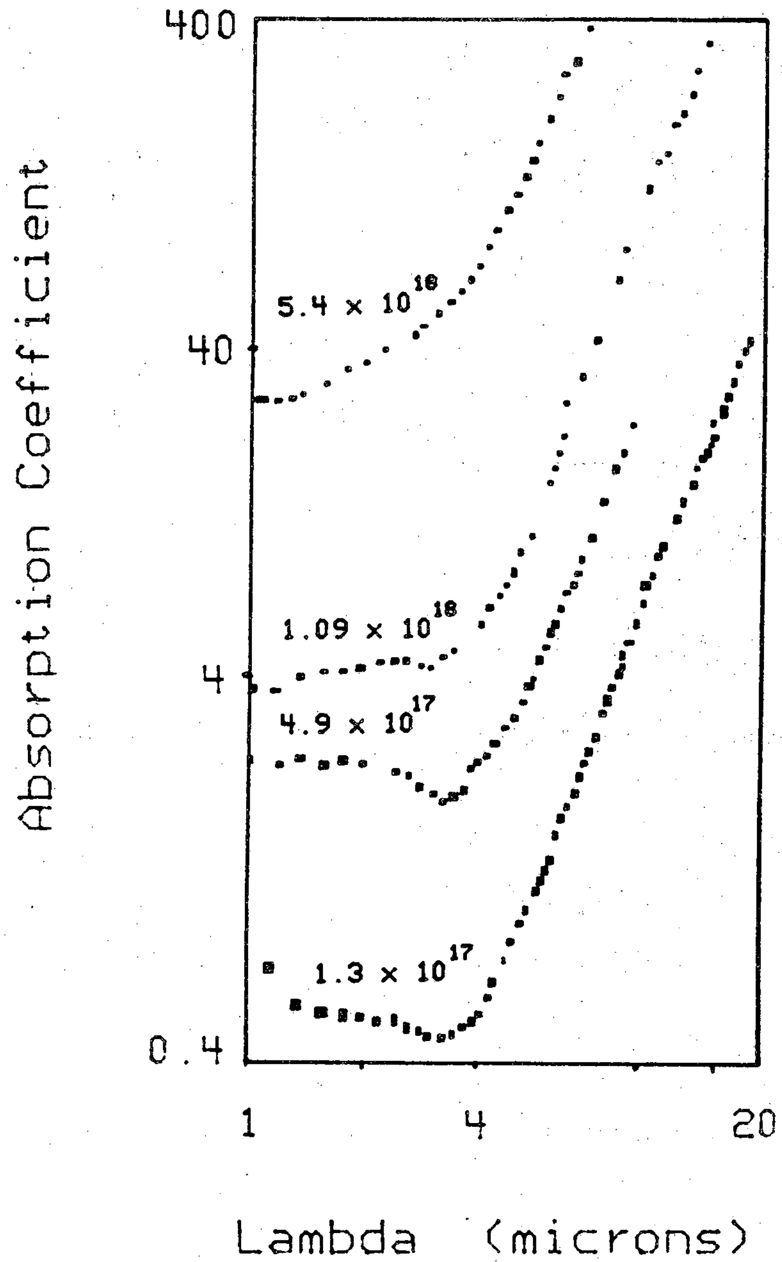

Figure 2.4.2 Absorption Coefficient versus λ Showing Effects of Free-Carrier Absorption

associated low absorption coefficients (~ 100) are the first transitions made.

Impurity Absorption

Although there is something intrinsically appealing about a well-ordered crystalline lattice, it is with the introduction of impurities or crystalline defects that we achieve some degree of control over the material's properties. The material can appear to be a microcosmic stew of potential absorbers and emitters. Several possible transistions from the valence band to localized impurity states and from acceptors to donors are illustrated in Figure 2.4.3.

Transitions from a neutral donor to the conduction band or from the valence band to a neutral acceptor could occur by the absorption of a low energy photon. This process could occur for electrons with energy equal to or greater than the impurity ionization energy. These transitions are of little concern to us, however, as we generally consider complete ionization of the impurities and in the case of incomplete ionization the energies involved are much less than the lower bounds of the spectral region of interest.

We might expect processes **b** and **d** to produce a bump in the fundamental absorption edge [Figure 2.4.4], however at doping levels large enough to produce a marked effect the additional complication of band-tailing causes a smearing of the edge and any structure due to **b** and **d** is obscured.

Our conclusion is that although the processes described above may be useful in locating impurity states in the bandgap, they have little impact on the absorption spectrum as it applies to solar cell operation.

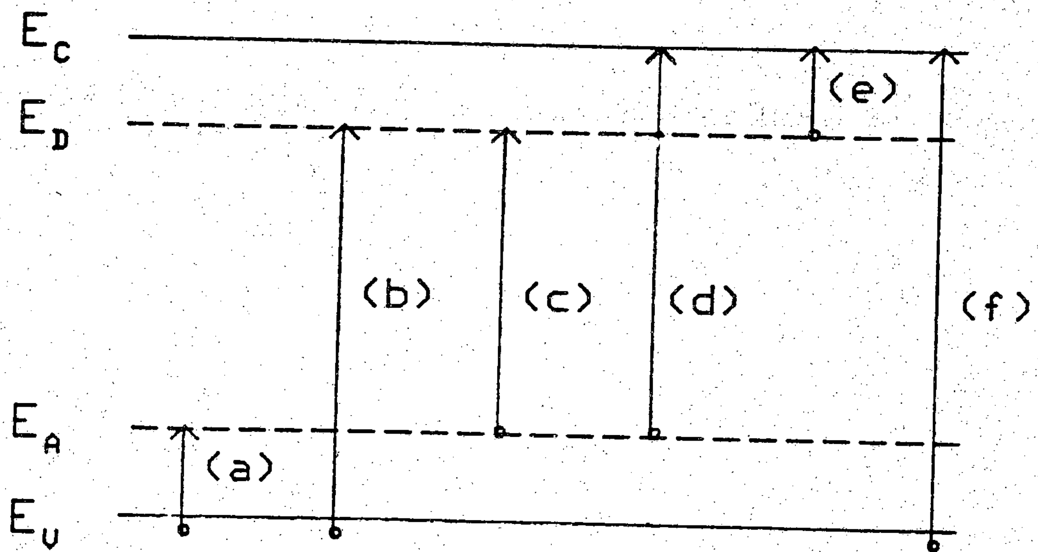

Figure 2.4.3 Optically Induced Transitions Between Bands and Impurity Levels

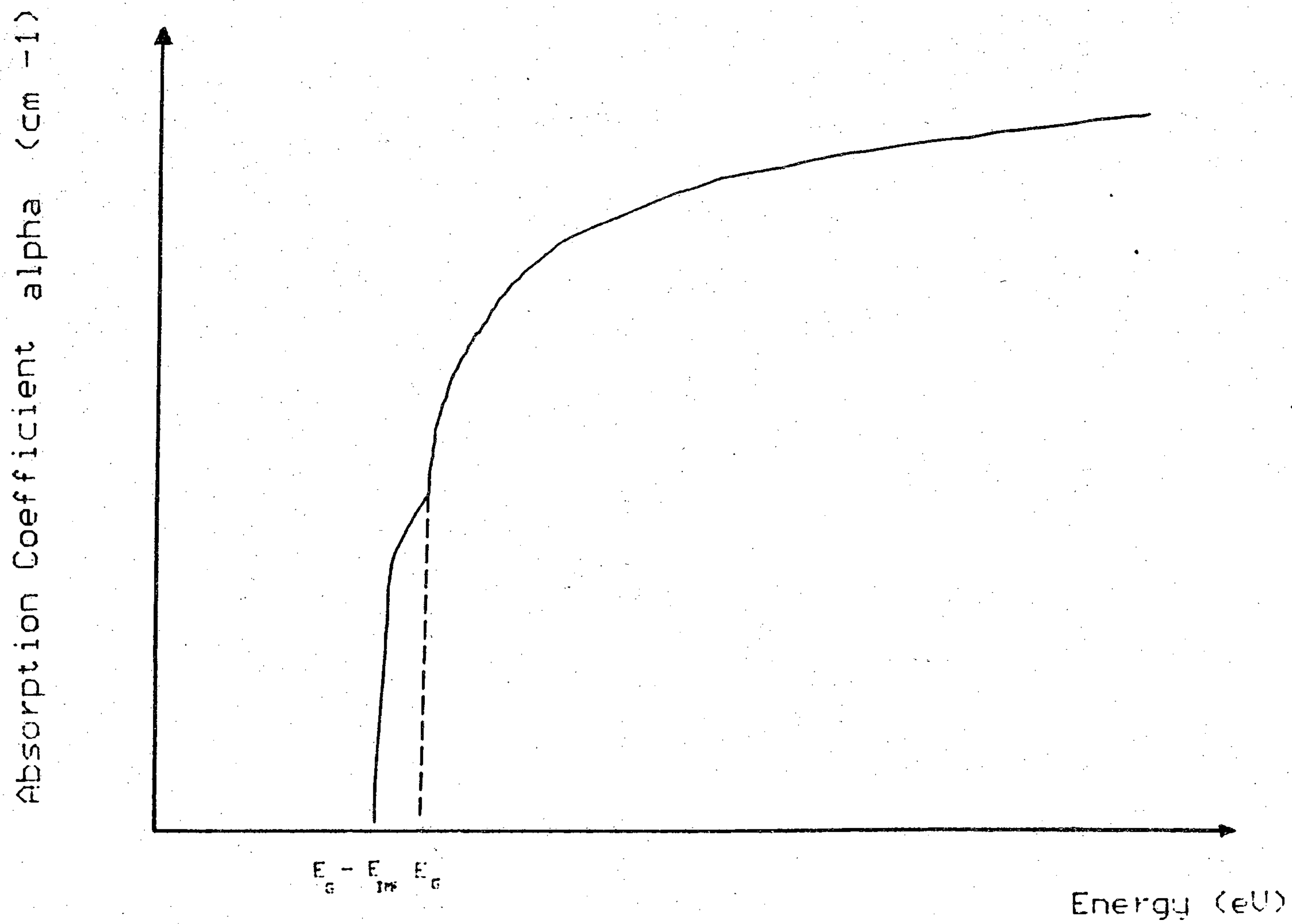

Figure 2.4.4 Idealized Fundamental Absorption Edge

Interband Transitions

At last we are at the heart of the matter. Interband transitions by the absorption of photons represents the most important process by which carriers are generated in the absorbing material. These transitions may be made between indirect-valleys (an important mechanism for Si and Ge) with the assistance of phonons and impurity scattering [Figure 2.4.5] or between direct valleys without the necessity of interaction with a third body to conserve momentum [Fig. 2.4.6].

Because GaAs has a direct band-gap it might be expected that its absorption spectra is simply modeled. The simplest model which considers only the initial and final density of states and the optical transition probability yields [31] :

$$\alpha(h\nu) = \frac{A}{(h\nu)}\,(h\nu - Eg)^{1/2}, \quad h\nu \geq Eg \tag{2.4.8}$$

Fitting this equation to the data of [49] yields A=7.5e4. This expression provides a temperature dependence for α through the temperature dependence of Eg. Comparing this model with the work of Sturge [49] we find that the expression adequately describes the shift for low-temperatures, however, it fails to show the peak due to exciton absorption which is readily observed at low temperatures. We will consider the impact of this shortcoming later.

In contrast to the region around the bandgap, available data for absorption in the region >2ev is derived from reflection data by a Kramer-Kronig analysis [50]. Casey et.al. [51] used a Kramer-Kronig analysis of reflectance data near the bandgap in their study of heavy-doping effects on absorption. Their work and that of Phillip and Ehrenreich [50] agree well in the region of overlapping wavelength.

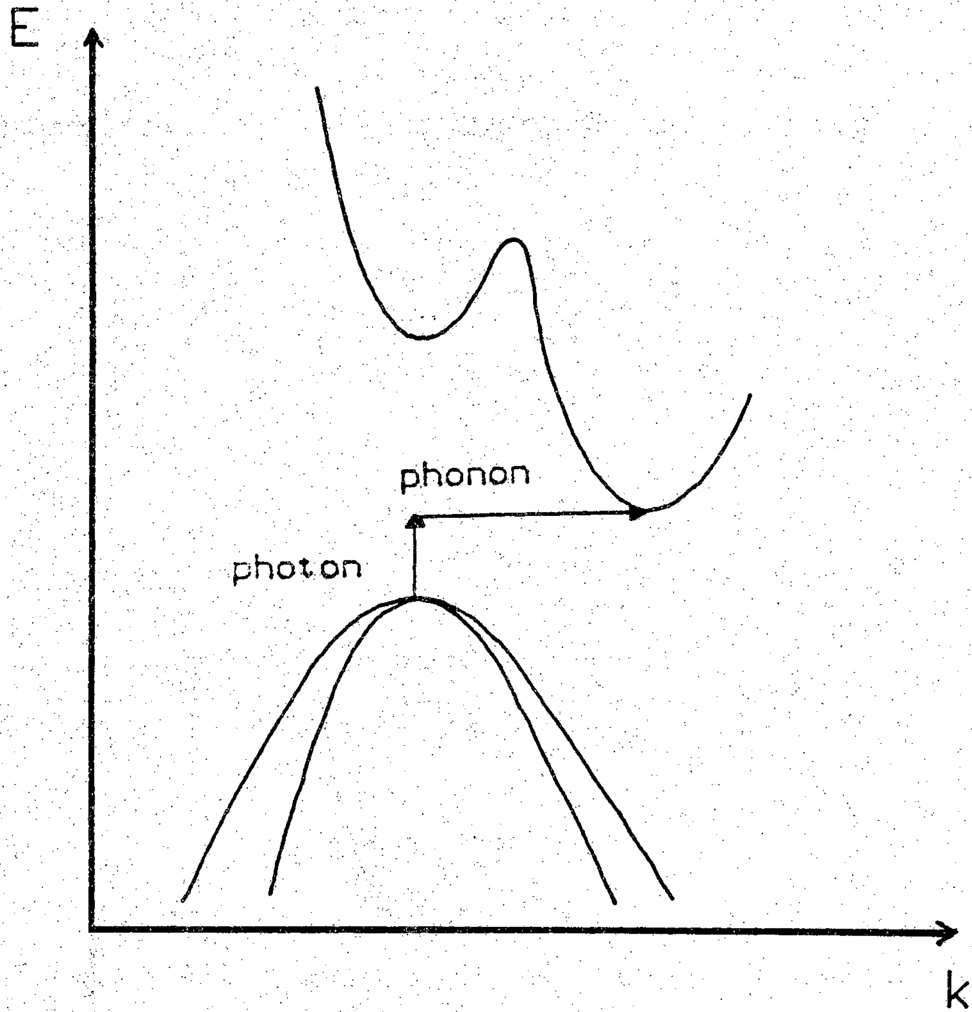

Figure 2.4.5 Transition Between Indirect Valleys

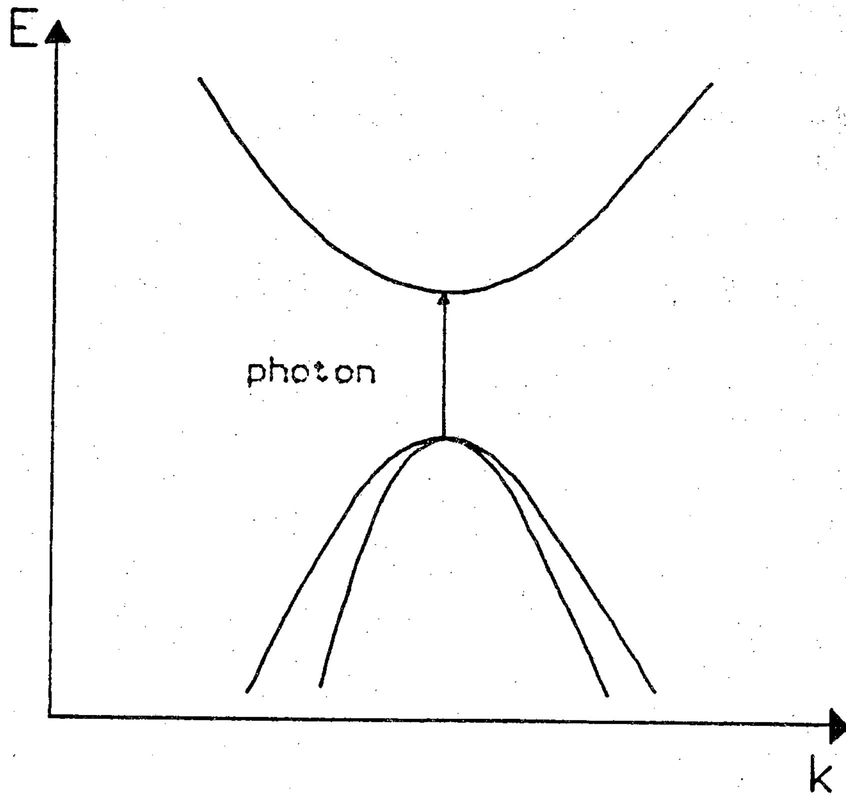

Figure 2.4.6 Transistion Between Direct Valleys

At higher photon energies (~ 1.75ev) a bump or shoulder appears in the absorption spectrum. This bump corresponds to the onset of transitions from the split-off valence band to the conduction band. If we use the same model form for the description of this additional absorption contribution, we have a total absorption spectra described by:

$$\alpha = \frac{A}{(h\nu)}(h\nu - Eg)^{1/2} + \frac{B}{(h\nu)}(h\nu - Eg - \Delta_{so})^{1/2} \tag{2.4.9}$$

Using our previous choice of 7.5×10^4 for A we find a best fit of the data with a B of 5.5×10^5. A comparison of the model with the data of Sutherland [51] is shown in Figure 2.4.7. Clearly, this model does not describe well the data near the fundamental edge. The experimental edge is not nearly so abrupt as the present model requires. This broadening of the edge is well known and is referred to as the Urbach tail [52-54]. The Urbach tail has a dependence on energy with a simple exponential form:

$$\alpha \simeq \beta e^{\gamma(h\nu - B)} \tag{2.4.10}$$

This exponential rule has been observed in many non-metallic materials and several theories have been proposed to explain its origin. Of these, theories resting on polaron interaction [55] and the Franz-Keldysh effect introduced by the local effective fields induced by impurities seem the most promising.

A good fit to the Casey data gives β=3.0e3, γ= 100, and B= Eg. Pankove [56] examined a doping dependence for γ in 1965 and found that γ generally increases with increased doping. Our overall model now gives a relatively good fit of the available experimental data for relatively pure samples [49-51] and can include some temperature effects through the variation in Eg, but what effect does heavy doping have? Casey [51] examined this question

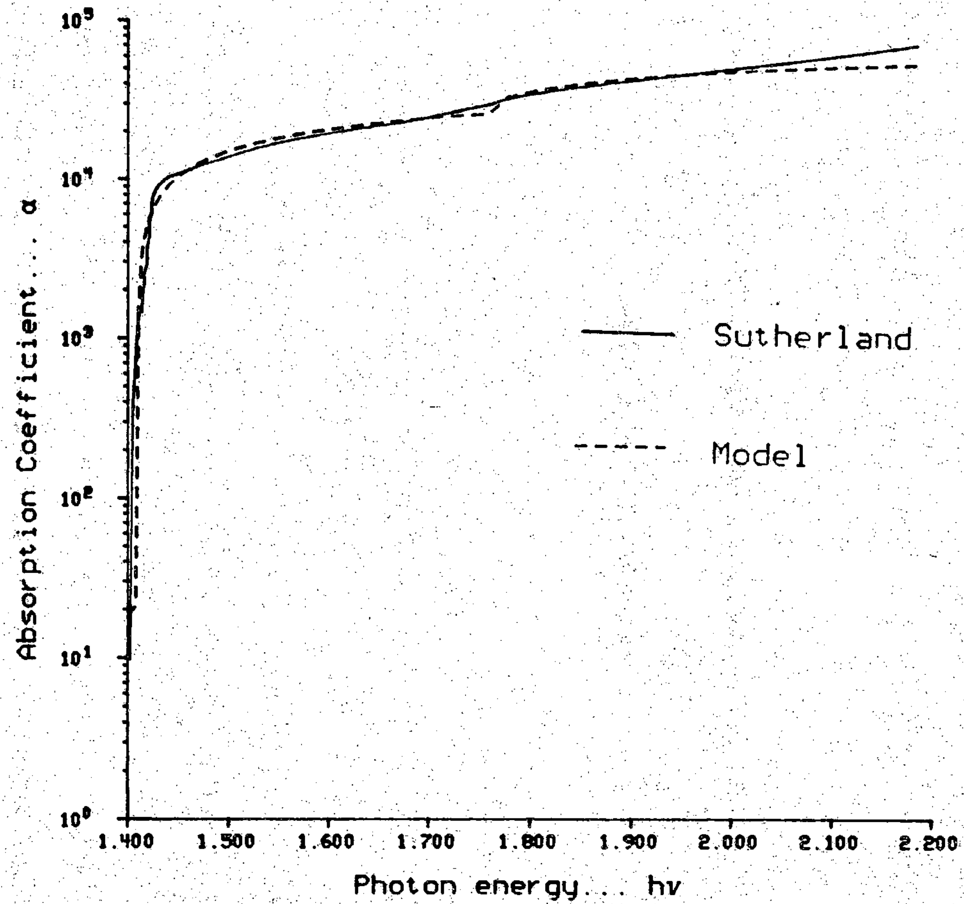

Figure 2.4.7 Comparison Between Absorption Coefficient Model and Experimentally Determined Results

experimentally in 1975 and developed a model to account for band-tailing in 1976 [57]. The shift to higher energies for n-type samples of heavy-doping is explained as a Moss-Burstein shift. The Fermi level goes into the conduction band at relatively low doping levels for n-type GaAs filling the conduction band states at lower energies, thus the available empty states for an optical interband transition lie at higher energy levels explaining the shift in the fundamental edge. The same effect is observed for heavily doped p-type GaAs, but at higher doping levels due to the higher density of states in the valence band. Initially, with heavy p-type doping a shift to lower energy is observed. This shift has been explained as a band-tailing effect. The heavy doping produces band-tail states which reduce the energy required for an optical transition. However, we should note the persuasive arguments which would attribute the phenomenon to many-body effects rather than band-tailing [34]. The nearly constant increase in absorption below the fundamental absorption edge is due to intra-band absorption and should be subtracted from the overall absorption coefficient when generation calculations are being made. Curves illustrating the results of Casey's work are found in Figure 2.4.8 and 2.4.9.

Now we have arrived at the crux of the problem. Which of the various phenomena associated with absorption in GaAs must be understood and accurately modeled to describe the performance of photovoltaic devices? Perhaps the best way to come to grips with this question is to examine the generation profile produced by the various absorption models in a solar spectrum. In Figs. 2.4.10 and 2.4.11 several curves representing the optical generation using several sets of experimental absorption data for highly doped GaAs are illustrated. For energies above 2.5ev, the work of Phillip and Ehrenreich [50] is routinely used since the absorption is too high for

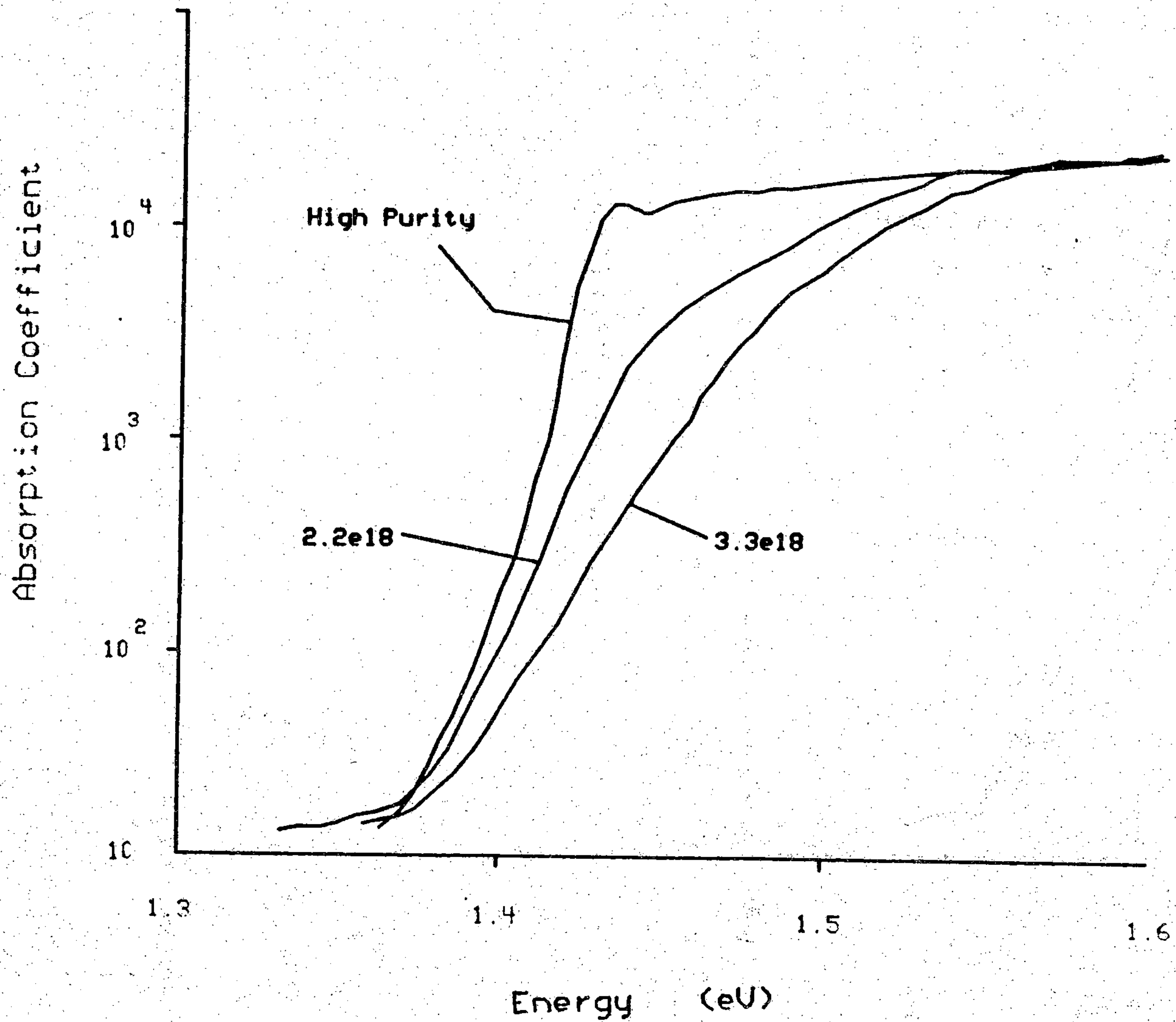

Figure 2.4.8 Absorption Coefficient for Heavily Doped n-Type GaAs

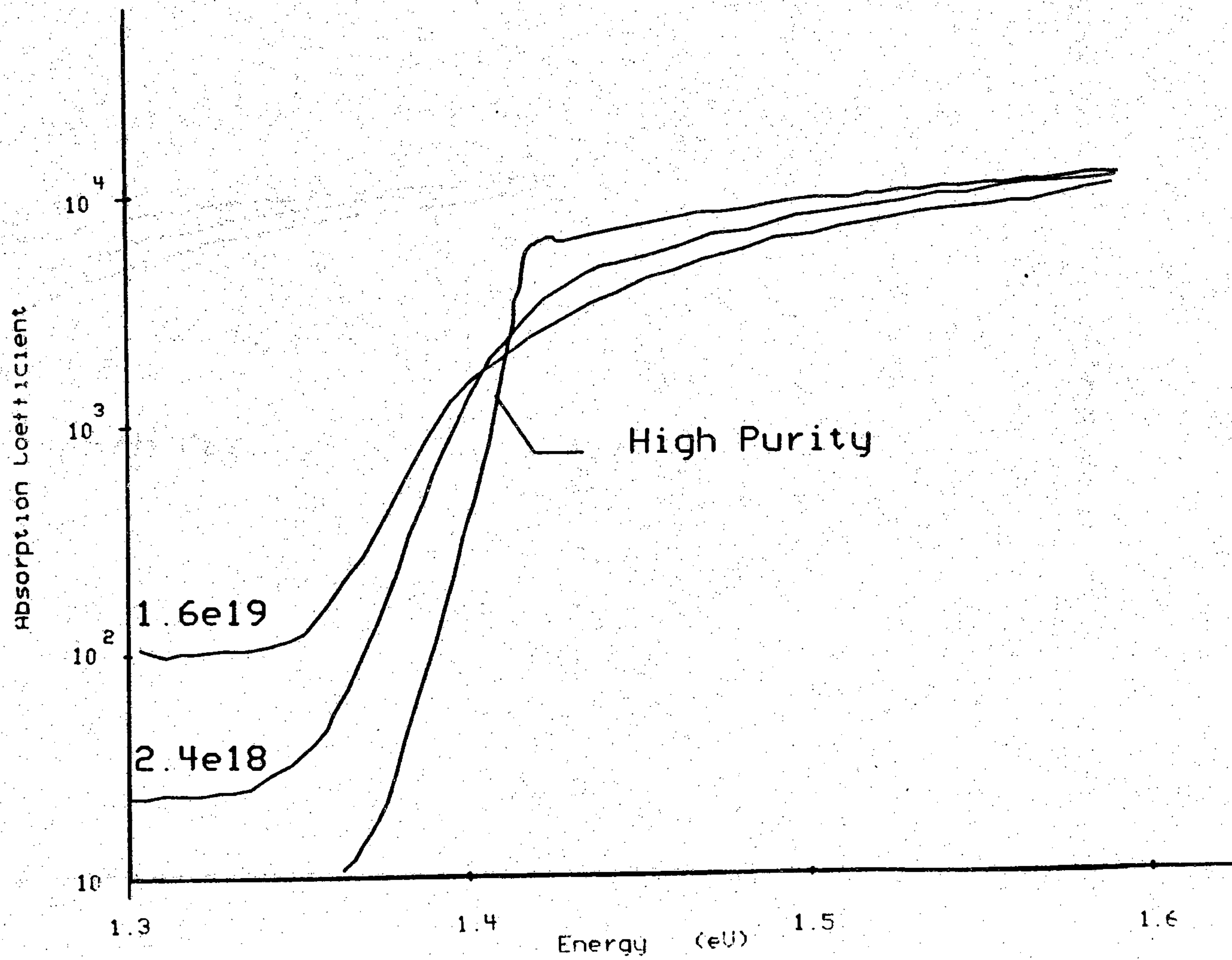

Figure 2.4.9 Absorption Coefficient for Heavily Doped p-Type GaAs

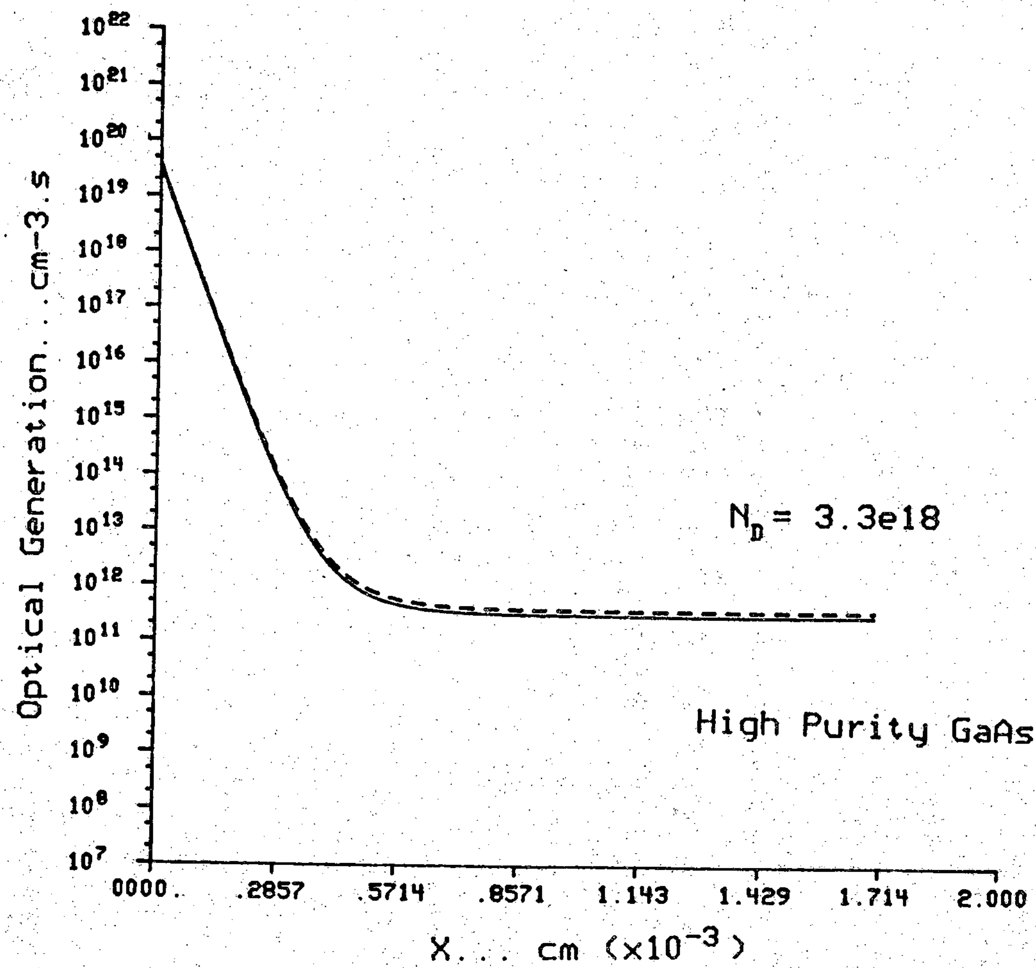

Figure 2.4.10 Optical Generation versus Distance for Heavily Doped n-Type GaAs

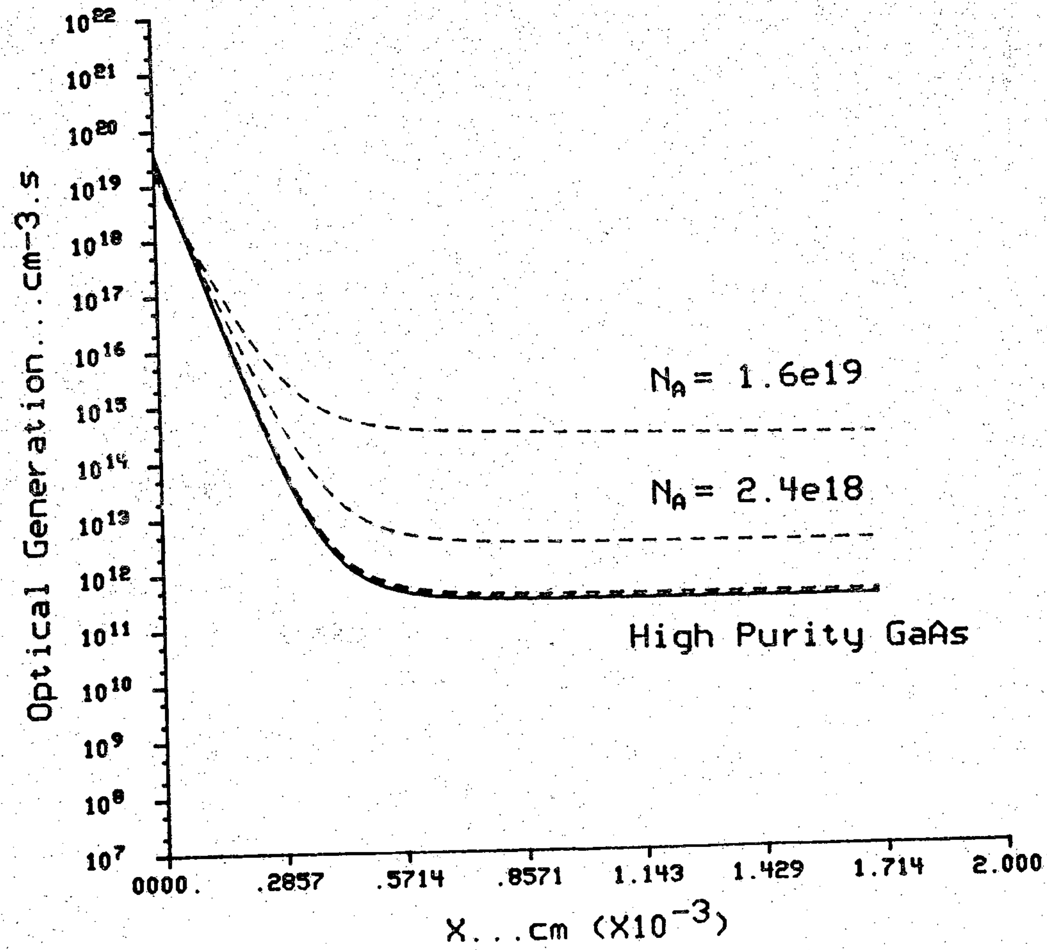

Figure 2.4.11 Optical Generation versus Distance for Heavily Doped p-Type GaAs

transmission techniques to be effective. It could be useful to perform ellipsometric measurements on GaAs in the ultraviolet region in order to verify the absorption data which is so frequently used.

Figs. 2.4.10 and 2.4.11 seem to indicate that in terms of optical generation over a solar spectrum heavy-doping effects are not critical for n-type material, however, they may lead to detectable effects in a photovoltaic device if a thick heavily doped p-type emitter is used.

2.5 Refractive Index

An optical parameter related to the absorption coefficient, the refractive index, has as its major application the evaluation of reflectance from a surface. It is common terminology to refer to the real part of the complex refractive index as simply the refractive index. We will use the following notation for the complex refractive index and its real and imaginary parts:

$$\mathbf{n}_c = \mathbf{n} - i\mathbf{k} \qquad (2.5.1)$$

The refractive index $\mathbf{n}$ is related to the extinction coefficient $\mathbf{k}$ through the Kramer-Kronig equations. Given a reflectance spectrum, the following set of equations is sufficient for solving for $\mathbf{n}$ and $\mathbf{k}$ [50]:

The Fresnel Equation:

$$r = \frac{\mathbf{n} - i\mathbf{k} - 1}{\mathbf{n} - i\mathbf{k} + 1} \qquad (2.5.2)$$

Reflectance:

$$R = r^2 = \frac{(n-1)^2 + k^2}{(n+1)^2 + k^2} \tag{2.5.3}$$

Phase:

$$\Theta = \tan^{-1}\left[\frac{-2k}{(n^2+k^2-1)}\right] \tag{2.5.4}$$

and the relationship between phase and reflectance:

$$\Theta(\omega_o) = \frac{1}{2\pi}\int_0^\infty \frac{d\ \ln R}{d\omega}\ \ln\frac{\omega+\omega_o}{\omega-\omega_o}\ d\omega \tag{2.5.5}$$

where ω_o is the frequency of interest. The equations above may be solved to obtain **n** and **k**.

Compared with the absorption coefficient there is relatively little data published concerning the refractive index of GaAs. The data is especially sparse for spectral regions above the band-gap. Once again the data of Phillip and Ehrenreich [58] derived from reflectance experiments is widely used. Figure 2.5.1 illustrates a curve which is a composite of data taken from Stillman [58] and Phillip and Ehrenreich [59]. Stillman's data is used for the spectral region $< E_g$ and agrees well with the data extracted from reflectance measurements over the same region. This data is fit well with a first-order Sellmeier-type equation [31]:

$$(n^2 - A) = \frac{(n_\infty{}^2 - A)}{[1 - B(h\nu)^2]}, \quad h\lambda \leq E_g \tag{2.5.6}$$

with the parameters at 300 K of:

$$\kappa_\infty = n_\infty{}^2 = 10.88 \tag{2.5.7a}$$

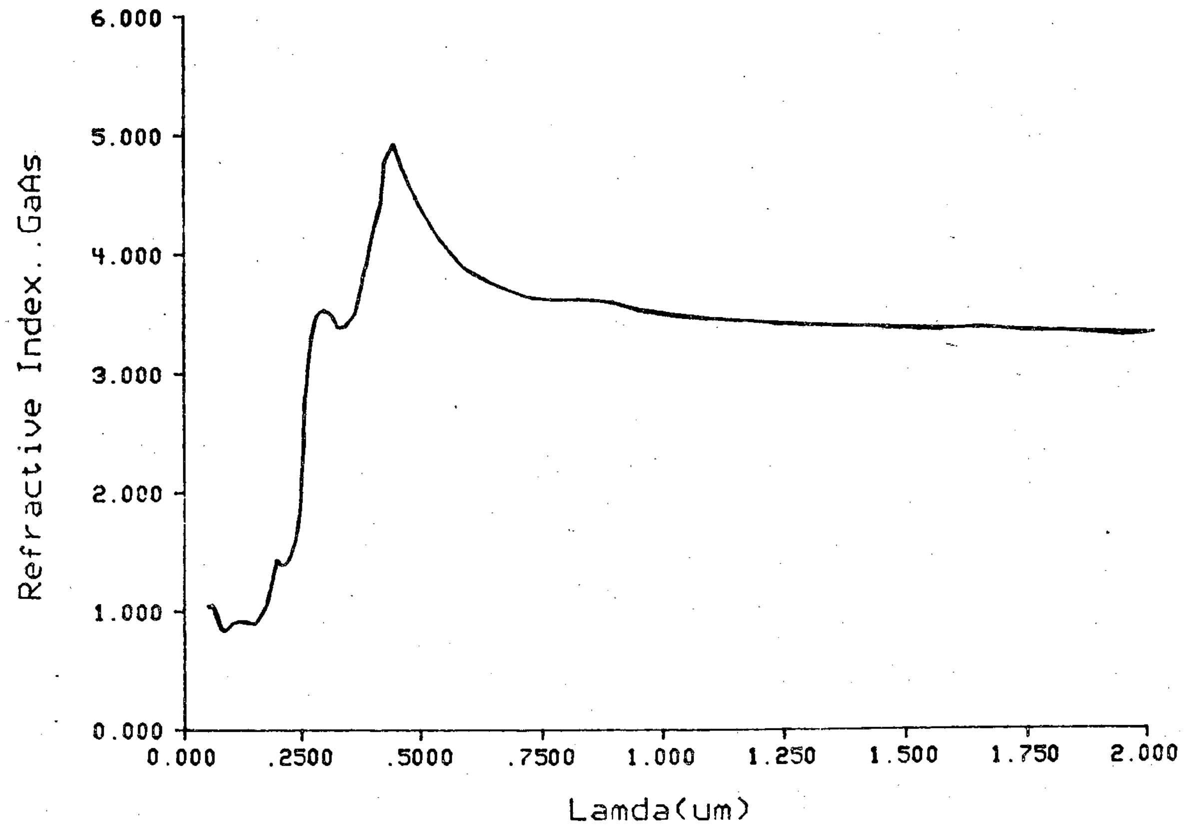

Figure 2.5.1 Refractive Index of GaAs

$$B = 0.18(\text{eV})^{-2} \tag{2.5.7b}$$

$$A = 7.10 \tag{2.5.7c}$$

Marple's [61] measurement of the variation of refractive index with temperature is commonly cited. His work showed a shift with temperature which is modeled well by:

$$n_\infty = 3.255\ (1.0 + 4.5\times10^{-5}\ T) \tag{2.5.8}$$

This shift was not unexpected in light of the temperature dependence of the energy-gap and the shift in the absorption curve.

What might affect the refractive index beside temperature and frequency? Perhaps we should consider free carriers, interband absorption and doping. Stern [62] provides an expression for the free-carrier effect on **n** :

$$\Delta n(h\nu) \simeq \frac{-9.6\times10^{-21}N}{\mathbf{n}E^2} \tag{2.5.9}$$

where N, **n**, and E are the electron concentration, index of refraction and photon energy. Stern also indicates that the interband absorption effect on the refractive index is negligible.

Sell, Casey, and Wecht [63] studied the doping concentration dependence of the refractive index for energies around the bandgap. Their results indicated that, as for the absorption coefficient, any change in refractive index due to doping, which might be evident near the bandgap, is absent at energies greater than 1.8eV.

Zoroofchi and Butler [64] described a numerical method for determining **n** both as a function of doping and of frequency, given **k** as function of doping

and frequency. Their results, however, did not match the experimental results of Sell et.al. [38] particularly well. Sell suggested that a large part of the error may have been due to a lack of good data for the absorption coefficient at high doping levels (Casey's paper dealing with the doping of the absorption coefficient [51] was not to come out for another year). It might be enlightening to apply the techniques of Zoroofchi and Butler to the Casey data.

However, we should review the role the refractive index plays in determining photovoltaic device operating characteristics before attempting to refine the refractive index model. The primary effect the refractive index has on a solar cells performance is through its determination of the reflectance from the surface (Eq. 2.5.5). It would be a mistake to look simply at the reflectance spectrum for doping effects since for some portions of the spectrum large variations in reflectance will have only marginal affects on the solar cell characteristics. Once again, we should look at the optical generation profile. Figure 2.5.2 shows the difference in the optical generation calculated when using the refractive index of a sample doped to $n = 5.9\times10^{17}$ cm^{-3} and with $n = 6.7\times10^{18}$ cm^{-3}. What we observe is essentially no dependence of the optical generation on the doping dependence of the refractive index. For the sake of comparison, curves are also shown for optical generation neglecting any reflection from the surface and for a uniform shadow factor of 0.5. This rather large shadow factor is used to account for effects of both shadowing and reflectance.

Although the variation of the refractive index with doping may be of great interest to workers in the laser area, it does not seem to be a major effect in photovoltaic devices.

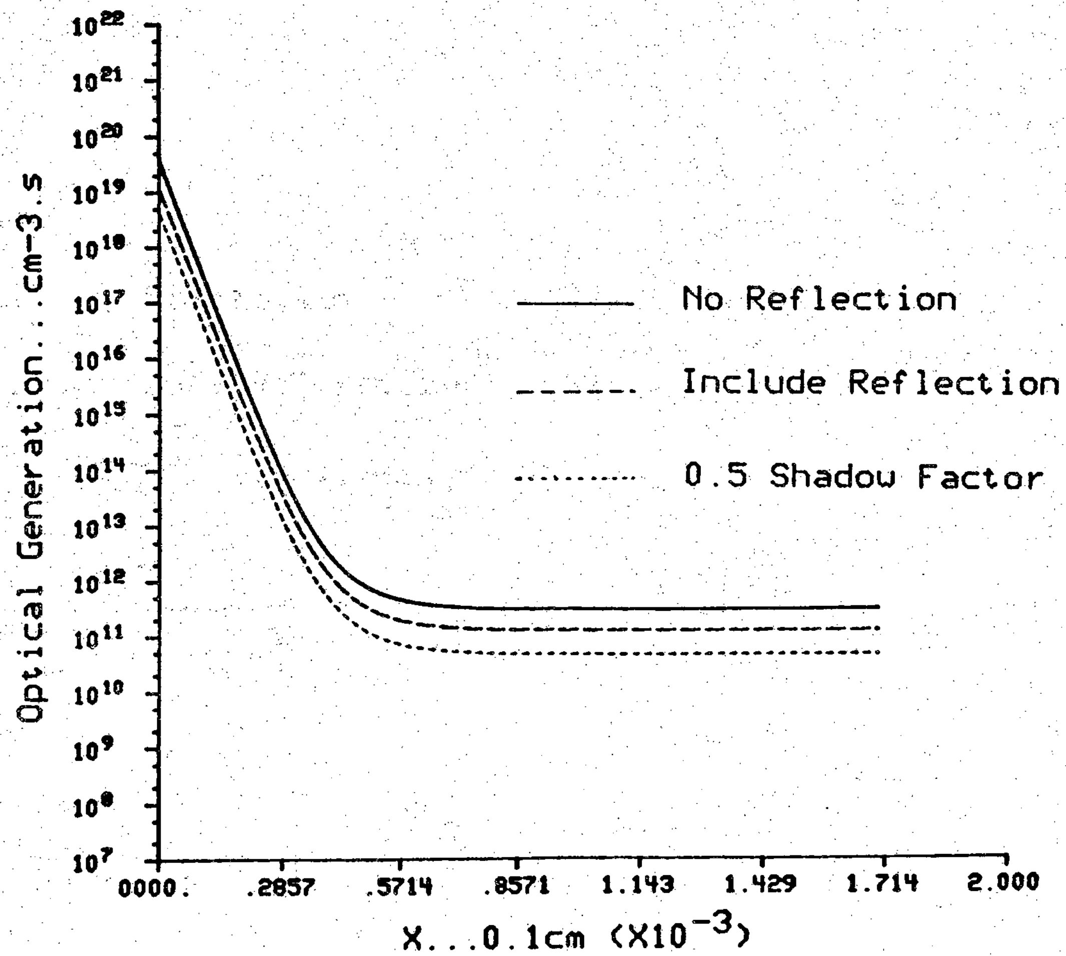

Figure 2.5.2 Optical Generation for Heavily Doped n-Type GaAs Considering Effects on the Refractive Index

We conclude that the refractive index for GaAs photovoltaic devices may be adequately modeled using a Sellmeier type equation [31] for energies below the bandgap and an interpolation of Phillip and Ehrenreich data [59] for energies above the bandgap. Temperature effects may be included by shifting the 300 K curves as directed by Eq. 2.5.8. When considering the refractive index for energies above the bandgap we must remember that the reflectance measurement from which the refractive index and extinction coefficient were derived is extremely sensitive to surface preparation and the data that we are using is nearly 20 years old. The analytical instrumentation available with a molecular beam epitaxy system could provide the means for characterizing the quality of a surface before reflectance measurements are made.

2.6 Minority Carrier Diffusion Length and Lifetime

The minority carrier lifetime, τ, is a parameter which varies widely from sample to sample. Fahrenbuch and Bube [1] give a typical to maximum range for τ_n of 1.0nS - 60.0nS and for τ_p of 3.0nS - 8.0nS. Although the minority carrier lifetime shows the general tendency to decrease with doping concentration, there is such a scatter in actual values of τ with various materials processing and handling techniques that it can almost be considered a fit parameter in SCAP1D. It is anticipated that as a particular process is characterized and τ's determined that an empirical expression for the lifetime's dependence on doping will be derived for that particular process.

A closely related parameter is the minority-carrier diffusion length. Clearly the magnitude of $L_{n,p}$ has a profound effect on the projected efficiency of a cell. However, as for τ, there is a great deal of scatter in the reported values of the

minority-carrier diffusion length as indicated in Figures 2.6.1 and 2.6.2 [3,66-81]. A reasonably good estimate for the data presented is:

$$L_p \simeq 2.0 \ \mu m \tag{2.6.1}$$

$$L_n \simeq 8.0 \ \mu m \qquad N_A \leq 5.0\times10^{16} \tag{2.6.2}$$

$$L_n \simeq 48.96 - 2.45 \left(\log N_A\right) \qquad N_A \geq 5.0\times10^{16} \tag{2.6.3}$$

Essentially, then, when modeling a cell an educated 'estimate' for τ is made and this choice is refined until agreement with experiment is obtained. The resulting $\tau_{n,p}$ or $L_{n,p}$ must then be compared with the scatter plot to insure that a reasonable value was used.

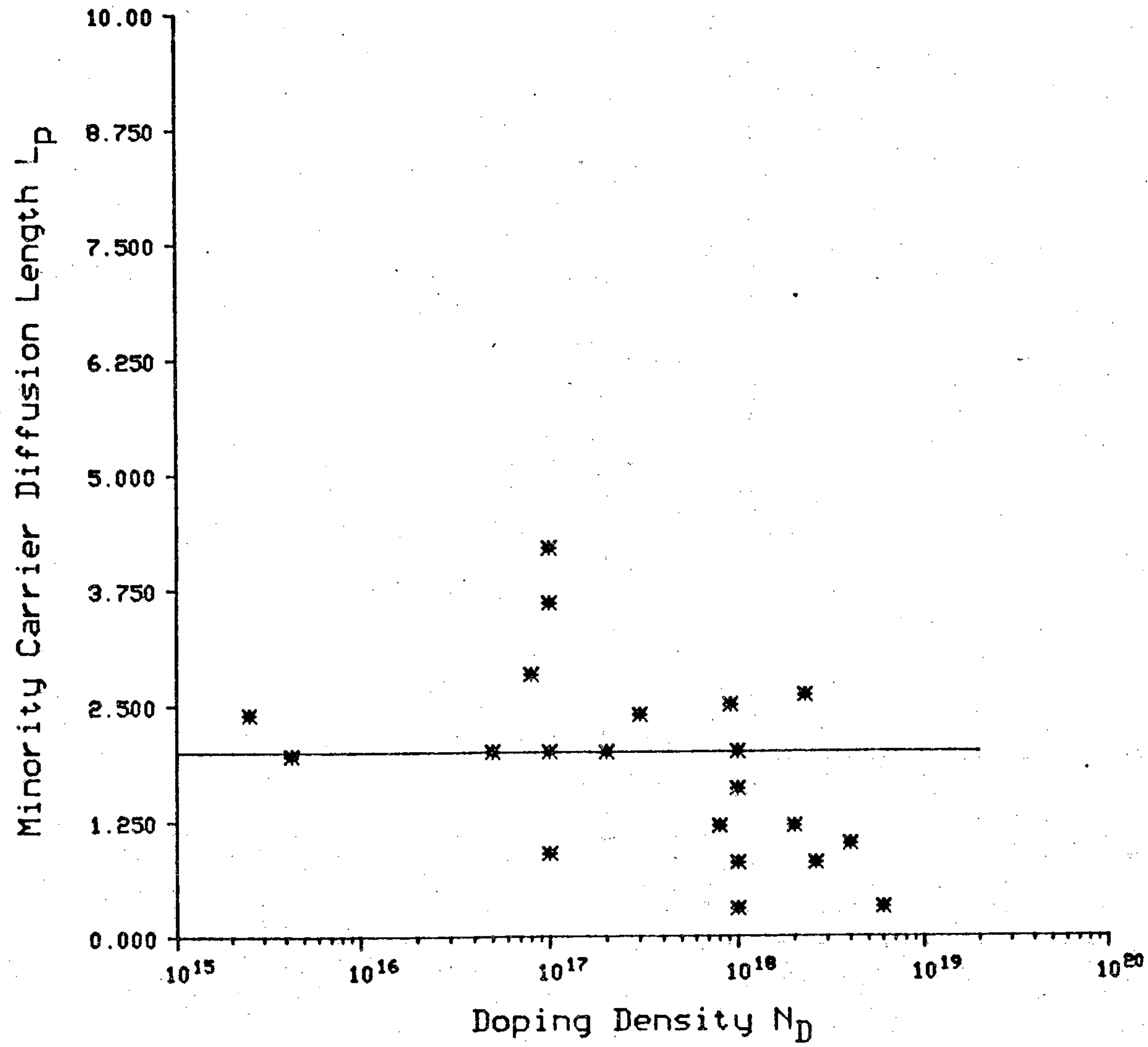

Figure 2.6.1 Minority Carrier Diffusion Length, L_p

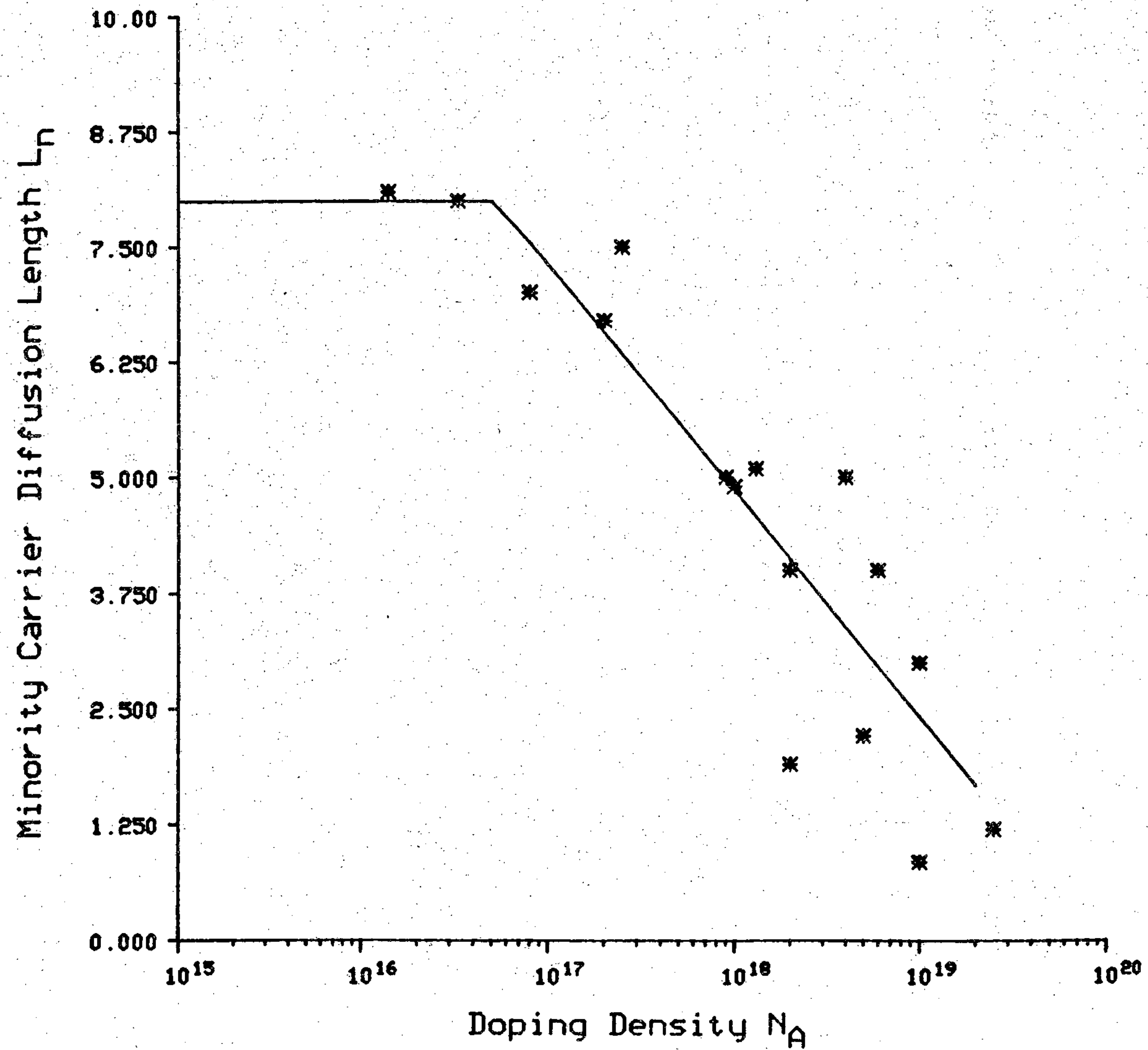

Figure 2.6.2 Minority Carrier Diffusion Length, L_n

CHAPTER 3
ANTI-REFLECTION COATINGS
MATERIALS AND MODELS

The purpose of this chapter is to examine two materials used as anti-reflection coatings for GaAs solar cells, $Al_xGa_{(1-x)}As$ and a native anodically grown oxide. The justification for treating $Al_xGa_{(1-x)}As$ as a material for anti-reflection coatings may be found in an examination of the heteroface cell. So few carriers are generated in the wide-band gap window that it may simply be treated as a component of the anti-reflection system.

To sufficiently characterize a material for use in an anti-reflection coating we must know both the refractive index, **n**, and the extinction coefficient, **k**, over the solar spectrum. For $Al_xGa_{(1-x)}As$ there is the additional complication that this information must be known over a broad compositional range.

3.1 $Al_xGa_{1-x}As$

Bandgaps

Knowledge of the positions of the three conduction band edges is required for our models of the absorption coefficient and refractive index. An examination of the models for GaAs indicate why the need for this information naturally arises.

Casey and Panish [46] used the following equations to describe the variation of the energy gaps with composition:

$$E_\Gamma(x) = 1.424 + 1.266x + 0.26x^2 \qquad (3.1.1a)$$

$$E_L(x) = 1.708 + 0.642x \qquad (3.1.1b)$$

$$E_X(x) = 1.9 + 0.125x + 0.143x^2 \qquad (3.1.1c)$$

These equations are plotted in Figure 3.1.1.

Energy gap as a function of temperature [31]:

$$E_\Gamma(T) = 1.519 - \frac{5.405\times 10^{-4}\,T^2}{(T + 204)} \qquad (3.1.2a)$$

$$E_L(T) = 1.815 - \frac{6.05\times 10^{-4}\,T^2}{(T + 204)} \qquad (3.1.2b)$$

$$E_X(T) = 1.981 - \frac{4.6\times 10^{-4}\,T^2}{(T + 204)} \qquad (3.1.2c)$$

From the equations above we readily see that the 'crossover' composition increases with increasing temperature.

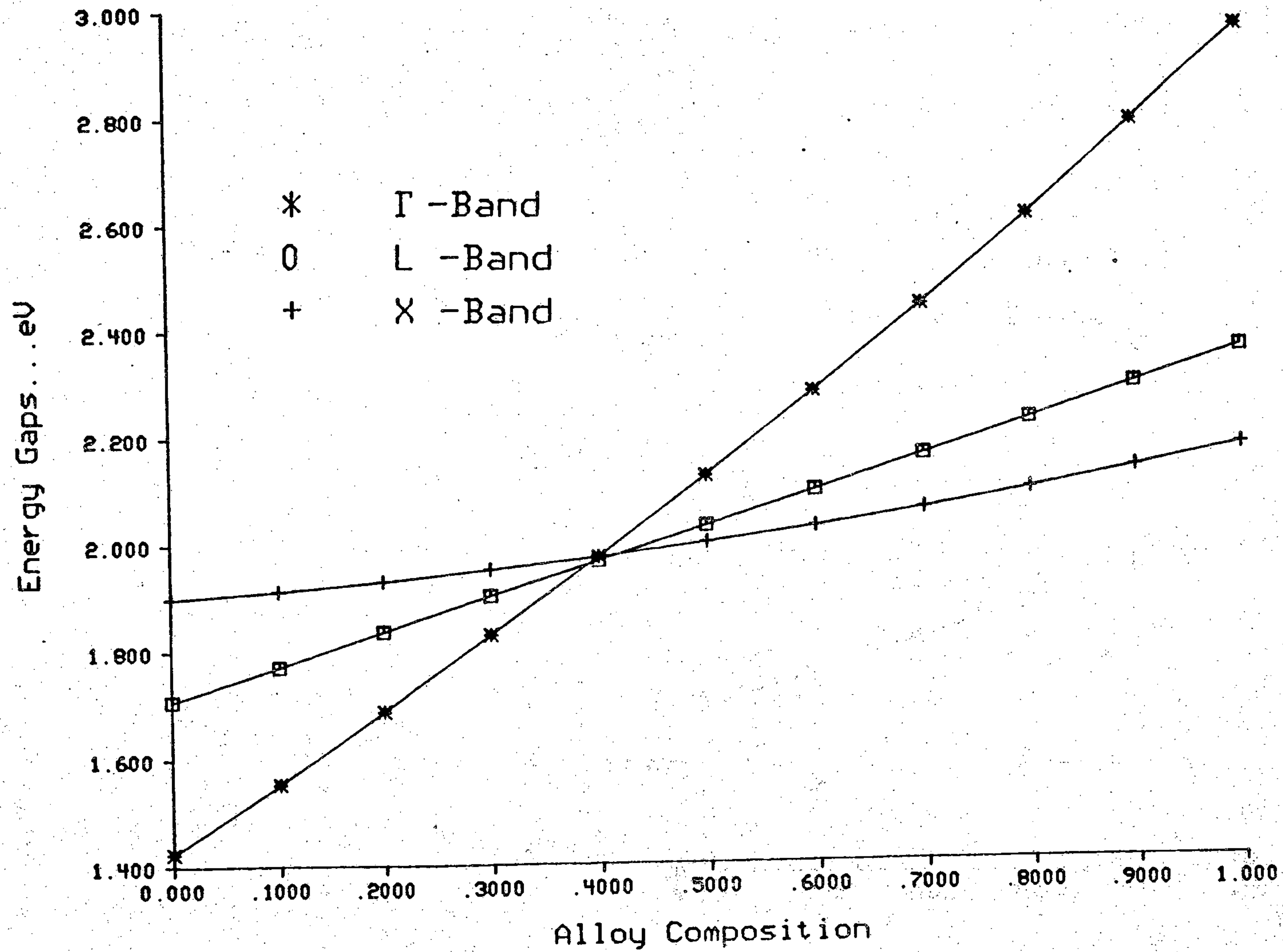

Figure 3.1.1 $Al_xGa_{1-x}As$ Bandgaps versus Composition

Assuming that a shift in temperature has the effect of shifting the E_{Gap} vs x function rather than changing its shape enables us to write:

$$E_{\Gamma}(x,T) = 1.519 - \frac{5.405\times10^{-4}\,T^2}{(T + 204)} + 1.266x + 0.26x^2 \qquad (3.1.3a)$$

$$E_{L}(x,T) = 1.815 - \frac{6.05\times10^{-4}\,T^2}{(T + 204)} + 0.642x \qquad (3.1.3b)$$

$$E_{X}(x,T) = 1.981 - \frac{4.6\times10^{-4}\,T^2}{(T + 204)} + 0.125x + 0.143x^2 \qquad (3.1.3c)$$

An additional parameter required for our models is the effective mass. The composition dependence of the density of states effective masses at room temperature are given by Casey and Panish [46] as:

$$\frac{m_{e_\Gamma}^*}{m_o} = 0.067 + 0.083(x) \qquad (3.1.4a)$$

$$\frac{m_{e_L}^*}{m_o} = 0.55 + 0.12(x) \qquad (3.1.4b)$$

$$\frac{m_{e_X}^*}{m_o} = 0.85 - 0.07(x) \qquad (3.1.4c)$$

$$\frac{m_h^*}{m_o} = 0.48 + 0.31(x) \qquad (3.1.4d)$$

With these band models in hand we may proceed to the determination of the absorption coefficient.

Absorption Coefficient

The determination of a model for optical absorption in $Al_xGa_{1-x}As$ is complicated by the variation of the bandgaps with composition (Figure 3.1.1) and the transition of the material from a direct-gap to an indirect-gap semiconductor. In addition, any model developed thus far has yet to be experimentally verified. Data is especially sparse for alloys with a large Al content, $x>0.45$. These high Al alloys are of particular importance in solar cell applications because of their use as heterofaces or window layers due to the low level of absorption associated with their indirect gaps.

Hutchby and Fudurich [82] used a simple model which involved shifting the portion of the GaAs absorption curve which corresponded to transitions involving the direct band-gap and the portion of the AlAs curve which corresponded to the indirect band-gap. The shift was determined by the change in the direct and indirect band-gaps with compensation. Sutherland and Hauser [22] adopted this approach in developing an absorption model for their heterostructure solar cell work. Although this technique may provide good results near the compositional end points (and as stated previously there has not been enough experimental data published to verify even this limited claim) the total disregard of the L- conduction band and the dependence of the density of states effective mass on composition causes the validity of this model

to be somewhat suspect for compositions in the range $0.2 \leq x \leq 0.8$.

The model proposed here and the one implemented in SCAP1D retains such desirable features of the Hutchby model as:

1) easy computability
2) easily adjusted parameters
3) reasonable agreement with experimental data at the compositional endpoints

while including

4) contributions to absorption by the L- conduction band
5) compositional dependence of the effective density of states mass

Our approach is to introduce expressions for the contribution to absorption by the three primary bands, Γ, X and L. We will retain our expression for absorption in GaAs to model the contribution by direct interband transitions to the Γ band:

$$\alpha_\Gamma(x) = \frac{A_\Gamma}{h\nu}[h\nu - E_\Gamma(x)]^{1/2} + \frac{B_\Gamma}{h\nu}(h\nu - E_\Gamma(x) - \Delta_{so})^{1/2}; \quad h\nu > E_\Gamma \tag{3.1.5a}$$

$$\alpha_\Gamma(x) = \beta e^{\gamma[h\nu - E_\Gamma(x)]} \qquad h\nu < E_\Gamma \tag{3.1.5b}$$

where E_Γ is a function of the composition variable x as indicated in equation [3.1.1a]. In addition, A_Γ and B_Γ vary with composition through their dependence on the reduced electron-hole effective mass:

$$m_{r}^{*} = \frac{m_{e_\Gamma}^{*}(x)\ m_h^{*}(x)}{m_{e_\Gamma}^{*}(x)\ +\ m_h^{*}(x)} \tag{3.1.6a}$$

and

$$A_\Gamma(x),B_\Gamma(x) = A_\Gamma(0),B_\Gamma(0)\left[\frac{m_\Gamma^{*}(x)m_e^{*}(0)}{m_\Gamma^{*}(0)\ m_e^{*}(x)}\right]^{\frac{3}{2}} \tag{3.1.6b}$$

The effective mass relationships are given in equations [3.1.4a-3.1.4b]. Since the model for α_Γ reduces to our model for α_{GaAs}, we are guaranteed agreement at the GaAs compositional endpoint.

A scarcity of data for the absorption coefficient for AlAs and a lack of quantitative agreement for the available data justifies a simplistic approach to modeling the absorption at the AlAs compositional extreme. Sources of experimental data are Yim [83], Mead and Spitzer [84] and Lorenz et.al.[85]. Hutchby used Yim's data for the extraction of fit parameters in the indirect portion of his model and we did the same.

Johnson [86] gives a simple expression for the form of the contribution to absorption of interband transitions through an indirect band-gap:

$$\alpha = \frac{B}{h\nu}(h\nu - E_{ind})^2; \qquad h\nu > E_{ind} \tag{3.1.7}$$

$$= 0.0; \quad h\nu < E_{ind}$$

where

$$B \propto N(m_e^{*}\ m_h^{*})^{\frac{3}{2}} \tag{3.1.8}$$

where N is the number of equivalent minima for that band. Since in AlAs the

X band contains the absolute minima which should govern the first or lower energy portion of the absorption spectrum, we used $E_{ind} = E_X(x = 1.0)$ and found $B_X\ (x=1.0) \simeq 5000$. The composition dependence of B_X arises through the dependence of the effective mass on composition. Our expression for the contribution by the X-band has the form:

$$\alpha_X(h\nu,x) = \frac{B_X(x)}{h\nu}\left[h\nu - E_X(x)\right]^2; \qquad h\nu > E_X(x) \tag{3.1.9}$$

$$= 0.0; \qquad h\nu < E_X(x)$$

where

$$B_X(x) = 5000\left[\frac{0.85 - 0.07x}{0.78}\right]^{\frac{3}{2}} \tag{3.1.10}$$

Similarly, the contribution by the L-band is given by:

$$\alpha_L(h\nu,x) = \frac{B_L(x)}{h\nu}[h\nu - E_L(x)]^2; \quad h\nu \geq E_L(x) \tag{3.1.11}$$

where

$$B_L(x) \simeq 2650\left[\frac{0.55 + 0.12x}{0.67}\right]^{\frac{3}{2}} \tag{3.1.12}$$

The prefactor in equation 3.1.12 was estimated from our knowledge of the number of conduction band minima, effective masses, and the extracted parameter $B_X(x)$. The absorption coefficient spectra for ten different compositions is shown in Fig. 3.1 2.

Clearly this simplistic model leaves much room for refinement, but until more experimental data is available for absorption throughout the compositional range, this model at least makes use of our knowledge of the

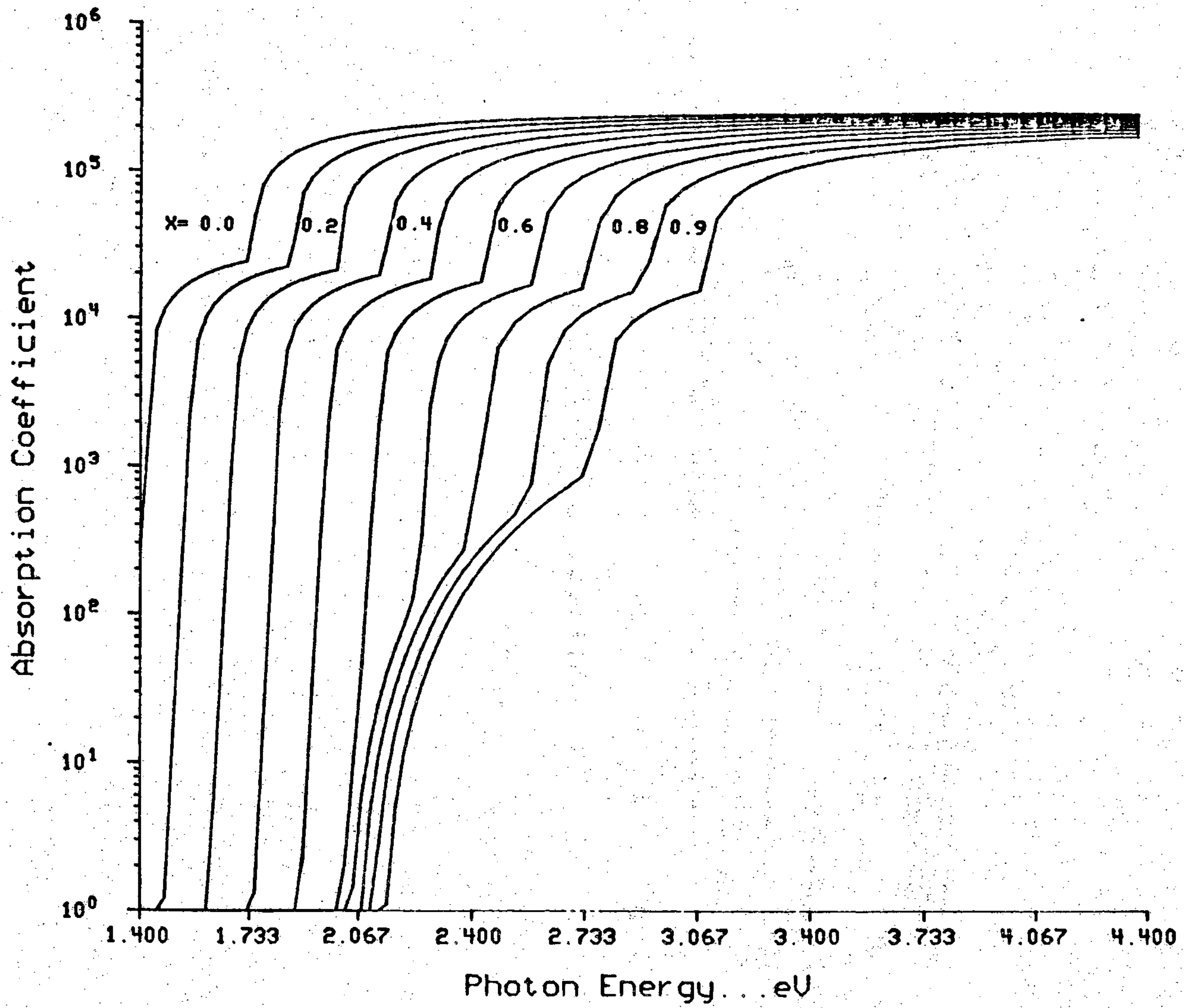

Figure 3.1.2 $Al_xGa_{1-x}As$ Absorption Coefficient for Several Compositions

band structure and its influence on absorption.

Refractive Index

As for GaAs, the primary role which the refractive index of $Al_xGa_{1-x}As$ plays in determining solar cell characteristics is through its effect on reflectance. Once again the primary treatment of the refractive index for $Al_xGa_{1-x}As$ in the literature is for spectral regions near and below the band-gap.

Several attempts have been made to model the variation of refractive index with composition. The simplest approach and one taken by Sutherland [22] is to simply shift the GaAs refractive index curve by an amount indicated by the change in bandgap with composition. This is clearly inadequate since the results obtained for AlAs are in substantial disagreement with the experimental results of Fern and Onton [87].

A plausible approach is to make a linear interpolation between the refractive index of GaAs and that of AlAs based on the samples composition. This is a considerably better approximation than a simple shift of the refractive index curve, but Kuphal and Dinges [88] published experimental data which indicates that the linear interpolation scheme is in considerable error for energies near the band-gap.

Aframowitz [89] developed a model based on the work of Wemple and DiDomenico [90] which uses a simple function as an approximation for ϵ_2, the imaginary part of the dielectric constant, one of the Kramer-Kronig relationships, and a simple single oscillator model. Aframowitz's model worked quite well for $Al_xGa_{1-x}As$, however, when he attempted to extend the

technique to $GaAs_{1-x}P_x$ system the results were not as good. Normally, this failure to model a parameter in another alloy system would not disturb us, but another model is available which has demonstrated its applicability not only to $Al_xGa_{1-x}As$ but also to $GaAs_{1-x}P_x$ and $Ga_{1-x}Al_xP$.

Pikhtin and Yas'kov [91] developed a model based on a uniform distribution of oscillators which has the form:

$$n^2(h\nu) - 1 = \frac{A}{\pi} \ln \frac{E_1{}^2 - h\nu^2}{E_0{}^2 - h\nu^2} + \frac{<\epsilon_2>}{\pi} \ln \frac{E_2{}^2 - h\nu^2}{E_1{}^2 - h\nu^2} \qquad (3.1.13)$$

where:

$$E_0 \simeq E_T = \Gamma_1{}^c - \Gamma_{15}{}^v$$

$$E_1 \simeq \Lambda_1{}^c - \Lambda_3{}^v$$

$$E_2 \simeq X_1{}^c - X_5{}^v$$

$$A \simeq \frac{0.7}{\sqrt{E_0}}$$

and $<\epsilon_2>$ is an adjustable parameter. The composition dependence is included in a straightforward manner by:

$$E_i(x) = E_i(0) + \left[E_i(1) - E_i(0)\right]x + c_i x(x-1); \quad i = (0,1,2) \qquad (3.1.14)$$

where c_i =0.0 for GaAs.

$$<\epsilon_2(x)>\left[E_2(x) - E_1(x)\right] = <\epsilon_2(0)>\left[E_2(0) - E_1(0)\right] + \qquad (3.1.15)$$

$$x\left\{<\epsilon_2(1)>\left[E_2(1)-E_1(1)\right]-<\epsilon_2(0)>\left[E_2(0)-E_1(0)\right]\right\}$$

Values for E_i and $<\epsilon_2>$ were given by Pikhtin and Yas'kov in an earlier paper [92] and appear in Table 3.1.

The problem remains as to how to model the refractive index above the band-gap. In lieu of experimental data or plausible theoretical models, we will simply 'graft' the GaAs refractive index data to the curves calculated by the Pikhtin and Yas'kov model.

Figure 3.1.3 illustrates curves for the refractive index as generated by the model installed in SCAP1D. Together with the model for absorption in $Al_xGa_{1-x}As$, the refractive index model provides us with the means to calculate the reflectance spectrum from alloy layers of uniform composition or with a composition profile.

3.2 Native Oxide

From our knowledge of the refractive index of GaAs and of the spectral distribution of the solar spectrum, we can calculate a total reflection coefficient for GaAs of ~.29 (AM0 spectrum). Clearly, reflection could be a major loss mechanism and an anti-reflection (AR) coating is in order.

Fortunately, an anti-reflection coating is readily obtained by the anodic oxidation of GaAs. Fan and Bozler [4] used this oxide for just this purpose in their work with shallow homojunction GaAs solar cells.

Table 3.1 Parameters for Refractive Index Model

Table 3.1				
Material	E_o	E_1	E_2	$<\varepsilon_2>$
GaAs	1.48*	3.0	5.1	28.57
AlAs	3.03**	3.7***	5.1	33.855

* SCAP1D uses 1.424 as a better fit for $E_{o_{GaAs}}$

** SCAP1D uses 2.95 as a better fit for $E_{o_{AlAs}}$

*** SCAP1D uses 3.68 as a better fit for $E_{1_{AlAs}}$

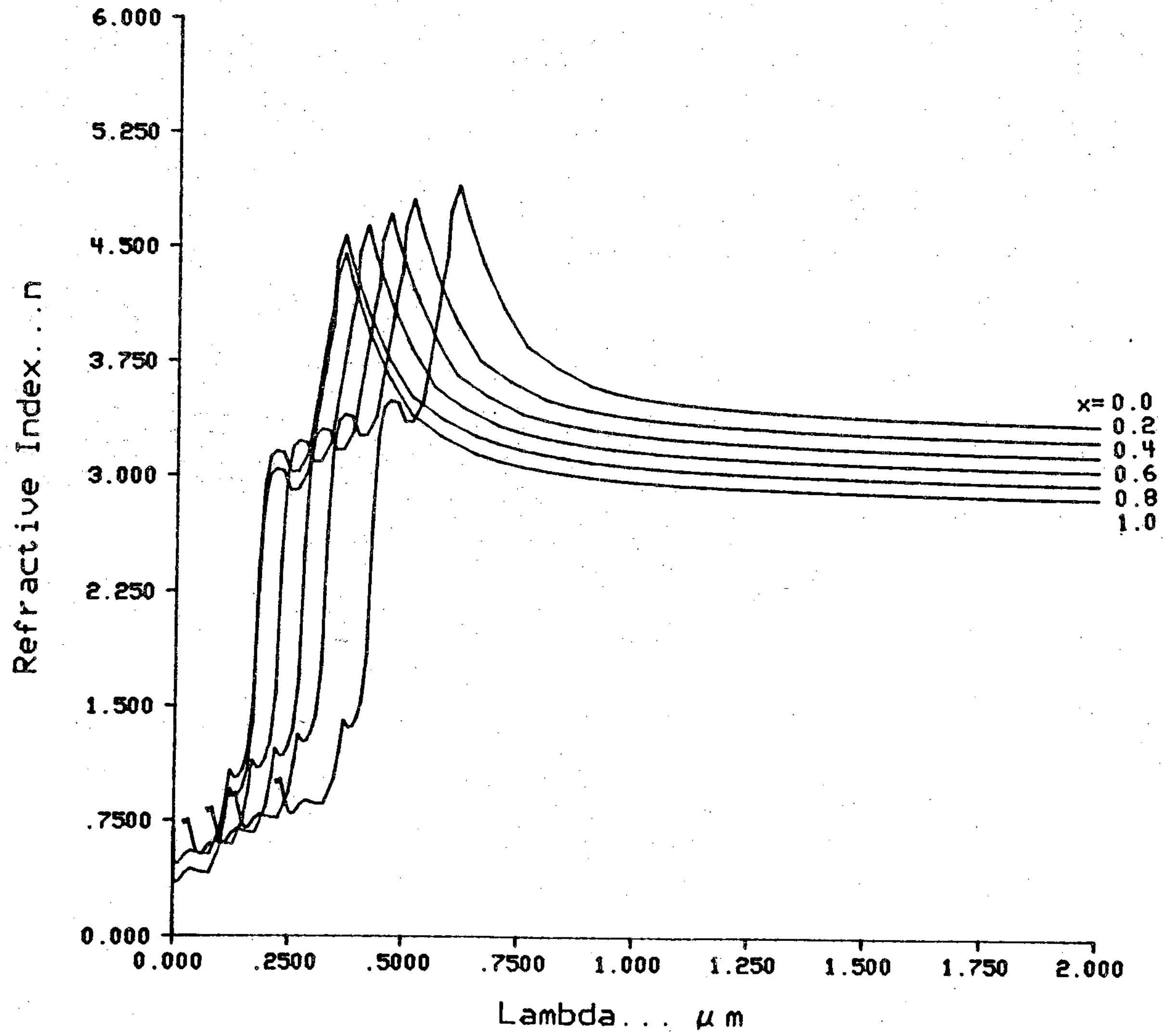

Figure 3.1.3 $Al_xGa_{1-x}As$ Refractive Index for Several Compositions

Barnes and Schink [93] investigated the refractive index for the oxide over the spectral range 0.4 μm – 1.2μm (3ev-1ev). They found a fairly wide range of refractive index values, but had success in using a least-squares fit of the data to a single oscillator Sellmeier equation of the form:

$$n^2-1 = \frac{S_o\lambda^2}{(\lambda^{2-}\lambda_o^2)} \tag{3.2.1}$$

with S_o = 1.914 and λ_o = 152.4nm. Barnes and Schink suggest annealing the oxide at 250 °C for one hour in a nitrogen ambient to improve the reproducibility of the optical characteristics.

Ishii and Jeppsson [94] also observed a variation in the refractive index with annealing. After a one hour heat treatment at 600 °C the refractive index became nearly constant at 1.5 for wavelengths from 0.5 μm through the infrared. Ishii and Jeppson examined the refractive index in the ultraviolet region and found it to vary strongly with wavelength. The oxide, which was virtually transparent throughout the visible and infrared portions of the spectrum, begins to absorb radiation at ~2.8μm. The additional complication of absorption in the oxide may be overlooked in a first approximation because of the extreme thinness of the oxide in anti-reflection applications and because of the small contribution to optical generation for the portion of the spectrum $<$ 2.8μm. An excellent discussion of the growth and etching of the oxide may be found in Ishii and Jeppsson as well.

Essentially, SCAP1D uses the simple Sellmeier equation to model the refractive index for this oxide, however, the user should be aware of potential

disagreement induced by process variation.

3.3 Reflection from Multiple-Layer Structures with Complex Refractive Indices

A potentially large source of loss for solar cells is reflection. A bare GaAs surface will reflect up to 30% of the power incident on it. Thus, some time should be spent in modeling potential anti-reflection (AR) coatings to determine the optimum AR system for a particular application. An approximation which is frequently made is that the AR layers are non-absorbing. This has been a reasonable approximation for most dielectrics used as anti-reflection coatings. Our interest in extending the calculations to layers composed of materials with complex refractive indices stems from the interest in the use of $Al_xGa_{1-x}As$ as a window layer for GaAs cells. The approach presented here is similar to that of Koltun [60] and is computationally quite simple. Essentially it is simply the solution of the following recursive formula:

$$r_{(j-1)} = \frac{f_{j-1} + r_j e^{-i2\phi_j}}{1 + r_j f_{j-1} e^{-i2\phi_j}} \tag{3.3.1}$$

Where f_{j-1} is the Fresnel coefficient and is given by:

$$f_{j-1} = \left[\frac{N_{j-1} - N_j}{N_{j-1} + N_j}\right] \tag{3.3.2}$$

Where the N_j's are complex refractive indices:

$$N_j = n_j - ik_j \tag{3.3.3}$$

The complex phase thickness, ϕ_j, is computed with:

$$\phi_j = N_j \frac{2\pi}{\lambda} l_j \tag{3.3.4}$$

The enumeration of the layers as shown in Figure 3.3.1 is the most convenient for writing code for the solution of Eq. 3.1.1 on the computer. If we set:

$$r_j = \left[\frac{N_j - N_{j+1}}{N_j + N_{j+1}} \right] \tag{3.3.5}$$

the calculation proceeds in a straightforward fashion. The reflection coefficient, R, is computed from the reflection amplitude coefficients, r_1 with:

$$R = r_1 r_1^* \tag{3.3.6}$$

All of the difficulty in modeling reflection from a multi-layered structure is associated with finding the refractive index, n, and the extinction coefficient, k, as functions of λ and possibly material composition.

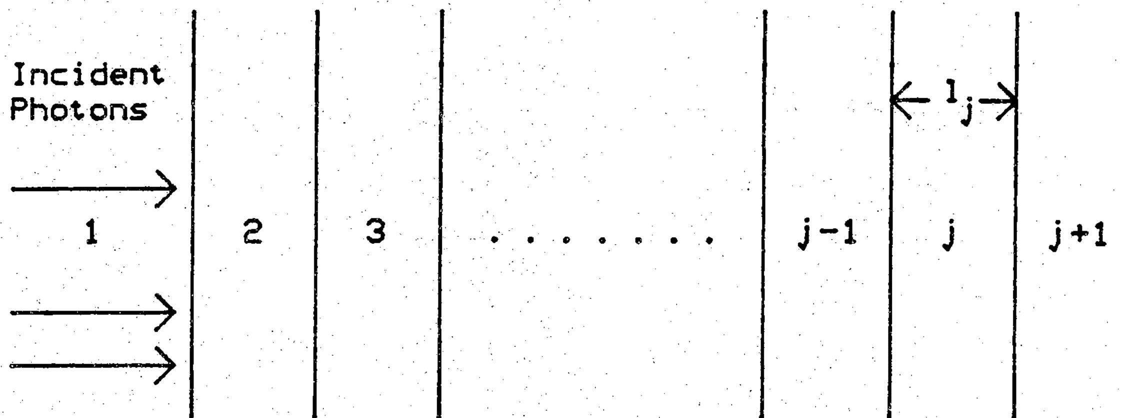

Figure 3.3.1 Enumeration of Layers for Multi-Layered Structure

CHAPTER 4
COMPARISON OF SCAP1D/GAAS TO EXPERIMENT

To convince ourselves that SCAP1D with GaAs extensions can simulate real devices, it is necessary to compare the results of the computer simulation to those determined experimentally. This requires descriptions of experimental cells which are complete not only in the description of the cell, but also in the description of the cell analysis. A logical beginning was the thorough analysis of a homojunction GaAs cell. The results presented in this chapter demonstrated that SCAP1D can, indeed, be applied to GaAs solar cells with a fair degree of success. This chapter also indicates the importance of including a reflection model within the code rather than simply relying on a lumped shadow factor.

4.1 Fan-Bozler Shallow Homojunction

The cell which we have examined most closely and the one which will be given the most emphasis in this chapter is the shallow homojunction of Fan and Bozler [4]. The general philosophy behind shallow homojunction cells was outlined in Chapter 1. A particularly attractive feature of these cells is the

relatively simple techniques used to fabricate them. Fan and Bozler point out that no vacuum processing steps were required for the $n^+/p/p^+$ structure. The base and emitter layer are grown by chemical vapor deposition (CVD) on a p^+ substrate. The anti-reflection coating was produced by anodically oxidizing the n^+ surface of the cell. Table 4.2 summarizes the parameters used to model this device. Note especially the shallowness of the junction, high surface recombination velocity, and short minority carrier lifetime. Essentially the surface recombination velocity, S_F, and the minority carrier lifetimes, τ_n and τ_p, are used as fitting parameters since their values are strongly dependent on material preparation. Results of the simulations were sensitive to variations of S_F from 10^4 cm/s to 6×10^6 cm/s and to variations of τ_n below 6.0 nS.

Because the base and emitter were grown by CVD techniques a step junction doping profile was used in the simulation (plots of the energy-band diagram appear in Figure 4.1.1). A choice of $S_F= 1.0\times10^6$ cm/s, $\tau_n= 4.75$ns and $\tau_p= 2.0$ns produced the best agreement with the experimental analysis of Fan and Bozler (Table 4.1).

Table 4.1 Results of SCAP1D Simulation of Fan-Bozler Cell

	J_{SC}	V_{OC}	η	FF
Fan & Bozler	25 mA	0.97 V	20%	.81
SCAP1D	24.6mA	0.98V	21%	.83

Note that the short circuit current, J_{SC}, and open-circuit voltage, V_{OC}, results agree with the values cited by Fan and Bozler to within 1.6%. These results compare favorably to the best of the minority carrier current equation models [20]. A comparison of the photocurrent versus applied voltage characteristics appears in Figure 4.1.2. Again, good agreement was obtained between the model and published experimental results. A representative sample of device plots generated by PLOT1D/SCAP1D are presented in Appendix B.

Two parameters frequently discussed in association with diodes and solar cells are the diode ideality factor, n, and the saturation current density, J_o, found in the ideal diode equation:

$$J = J_o\left(e^{\frac{qV}{nkT}} - 1 \right) \tag{4.1.1}$$

Table 4.2 **Parameters Used to Simulate Fan-Bozler Shallow Homojunction**

Parameter	Value
Temperature	$25^{\circ} C$
PN Junction Depth	$0.045\ \mu m$
High-Low Junction Depth	$2.045\ \mu m$
Device Length	8.0
Emitter Doping	$5.0\times10^{18} cm^{-3}$
Base Doping	$1.0\times10^{17} cm^{-3}$
Substrate Doping	$1.0\times10^{18} cm^{-3}$
Surface Recombination Velocity, S_F	$1.0\times10^{6}\ cm/sec$
Electron Minority Carrier Lifetime, τ_n	2.0 ns
Hole Minority Carrier Lifetime, τ_p	4.75 ns
Oxide Thickness	$0.085\ \mu m$
Solar Spectrum	AM1

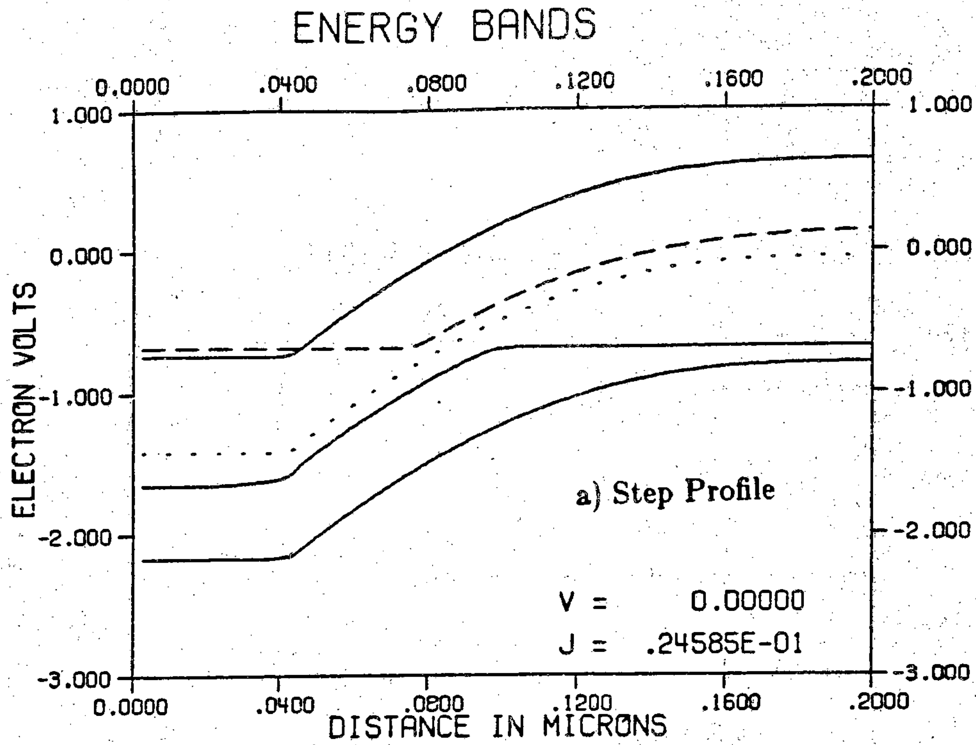

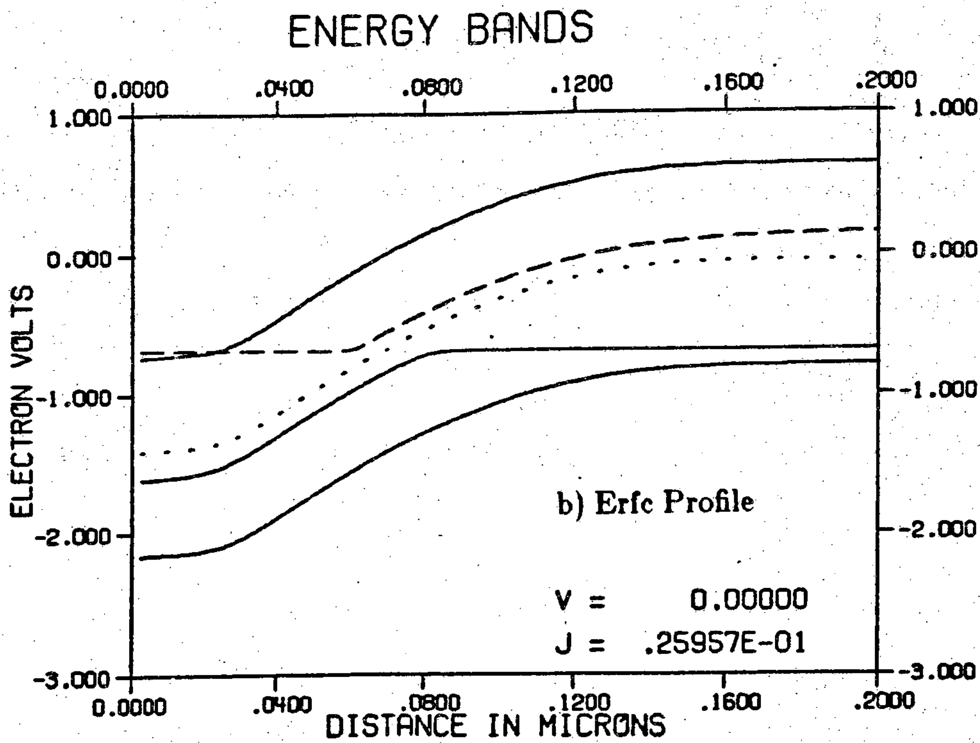

Figure 4.1.1 Energy Band Diagrams a) Step Profile, b) Erfc Profile

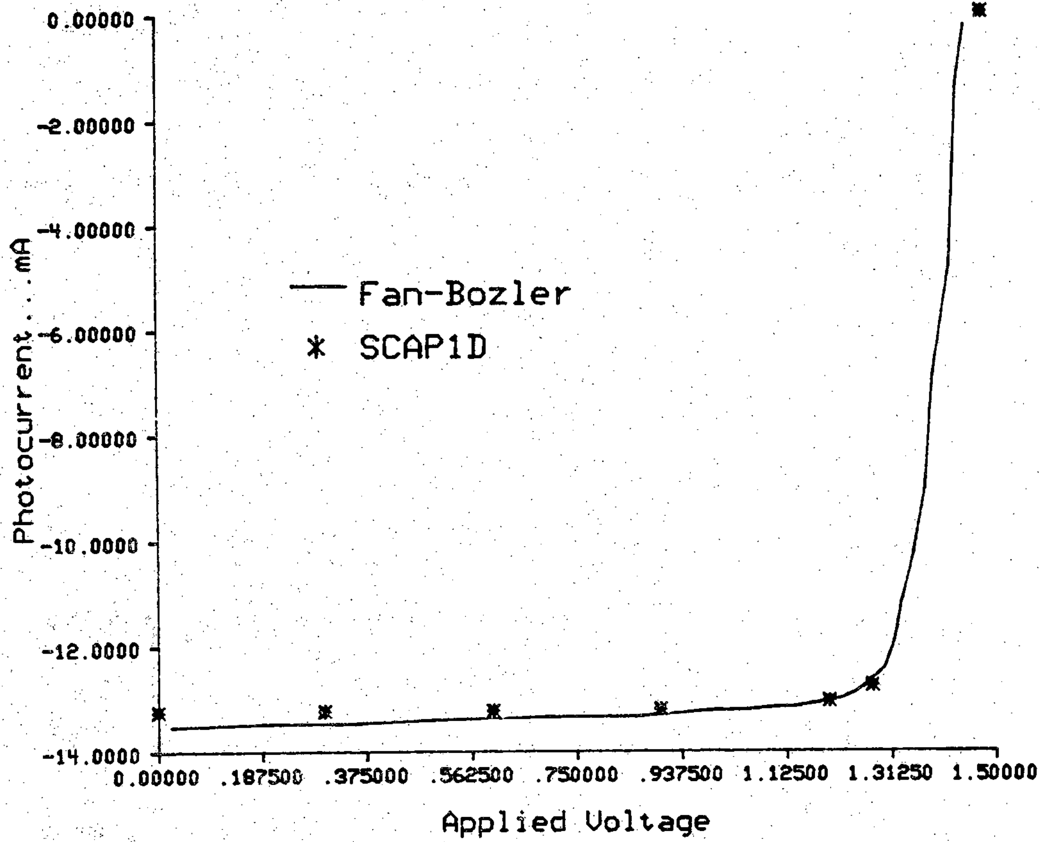

Figure 4.1.2 Photocurrent versus Applied Voltage...Fan and Bozler Shallow Homojunction

To extract the diode parameters, Fan and Bozler measured J_{SC} and V_{OC} for their cell at several levels of solar concentration. To compare our results to theirs, simulations were run for concentrations between 1 and 500 suns (Table 4.3). The values for these two parameters extracted from the simulations are compared to those obtained experimentally in Table 4.4.

Because of the abrupt absorption coefficient characteristic and high surface recombination velocity, the spectral response of these cells is of special interest. Figure 4.1.3 illustrates the initial results obtained from SCAP1D for the spectral response. Although agreement was improved somewhat by introducing reflectance, it was by no means satisfactory. These results were most disconcerting in light of the excellent agreement obtained in the other comparisons. All attempts to vary the adjustable parameters, S_F, τ_n and τ_p, were futile. Even new absorption models, although having a dramatic effect on the spectral response, could not improve the agreement. A change in the thickness of the anti-reflection coating could, however, produce the desired results. An increase of 0.01 μm in the thickness of the oxide produced the results of Figure 4.1.4. Varying the thickness of the oxide to obtain agreement is not satisfactory as oxide thickness is a parameter which lends itself to accurate measurement. However, the good agreement for all other facets of the comparison seem to indicate that the spectral response curve found in Fan and Bozler's paper [4] was not that for the cell with an oxide layer of 0.085 μm.

What if no reflection model is included within SCAP1D? Table 4.5 compares the results of a simulation with reflection turned on to one using a 10% shadow factor and reflection turned off. Figure 4.1.5 compares the optical generation rate for these two simulations. An examination of this figure indicates that agreement between the two generation rates could probably be

Table 4.3 J_{SC}, and V_{OC} for Several Solar Concentrations

Concentration	J_{SC}	V_{OC}
1 sun	0.0245 A	0.984 V
5 suns	0.1229 A	1.035 V
15 suns	0.3668 A	1.066 V
100 suns	2.4586 A	1.118 V
500 suns	12.295 A	1.161 V

Table 4.4 Ideal Diode Parameters

	J_o	A
Fan and Bozler	$1.4 \times 10^{-17}\ A/cm^2$	1.1
SCAP1D	$1.8 \times 10^{-17}\ A/cm^2$	1.1

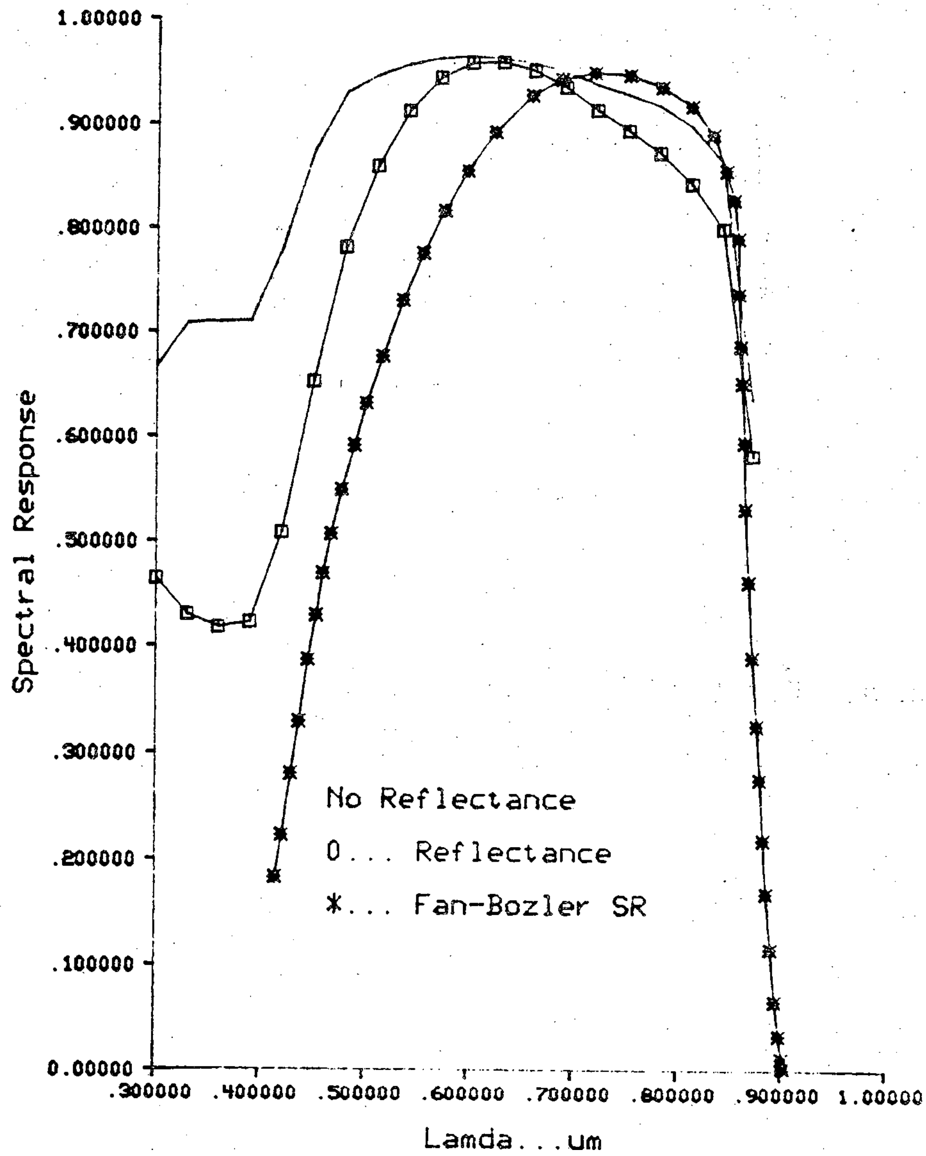

Figure 4.1.3 Spectral Response of Fan and Bozler Cell. Simulations Run for Oxide of 0.085 μm.

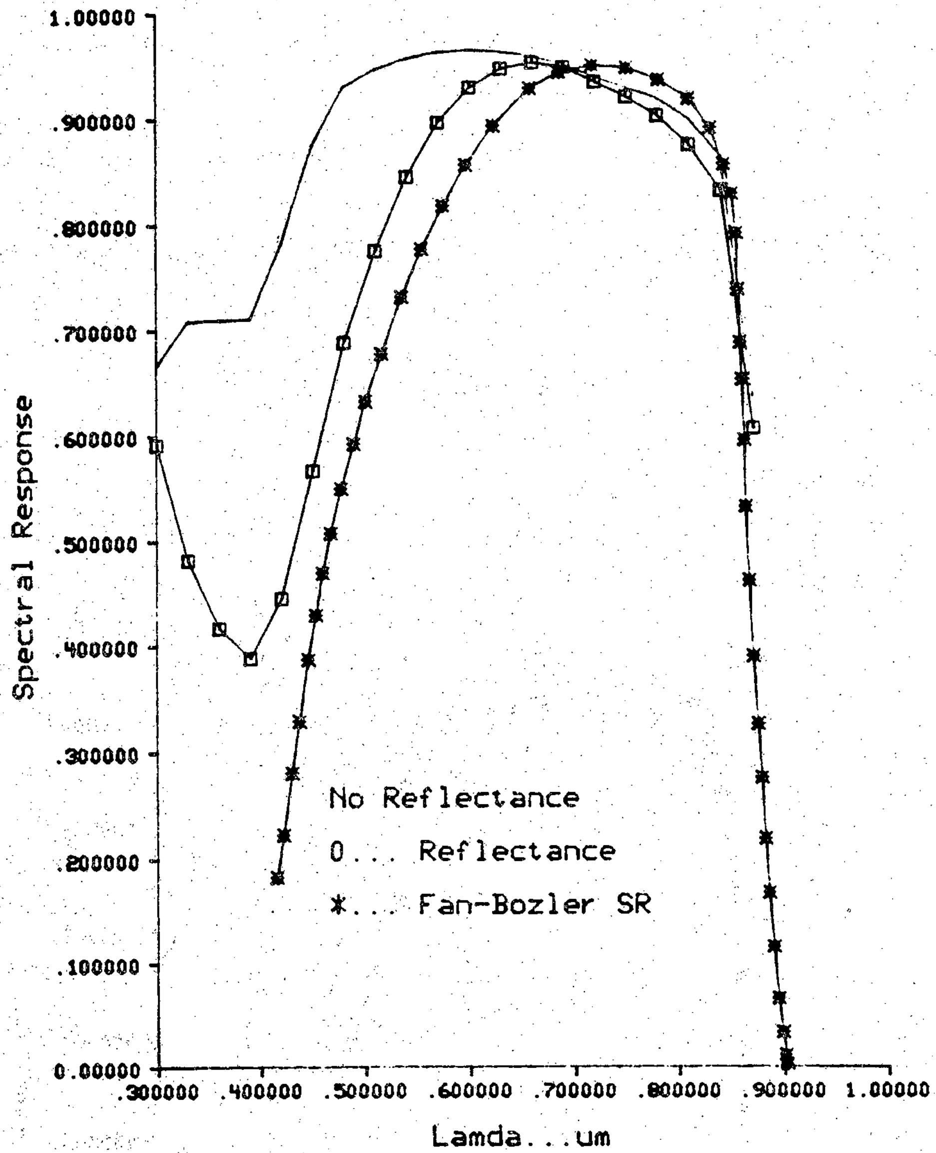

Figure 4.1.4 Spectral Response of Fan and Bozler Cell. Simulations Run for Oxide of 0.095 μm.

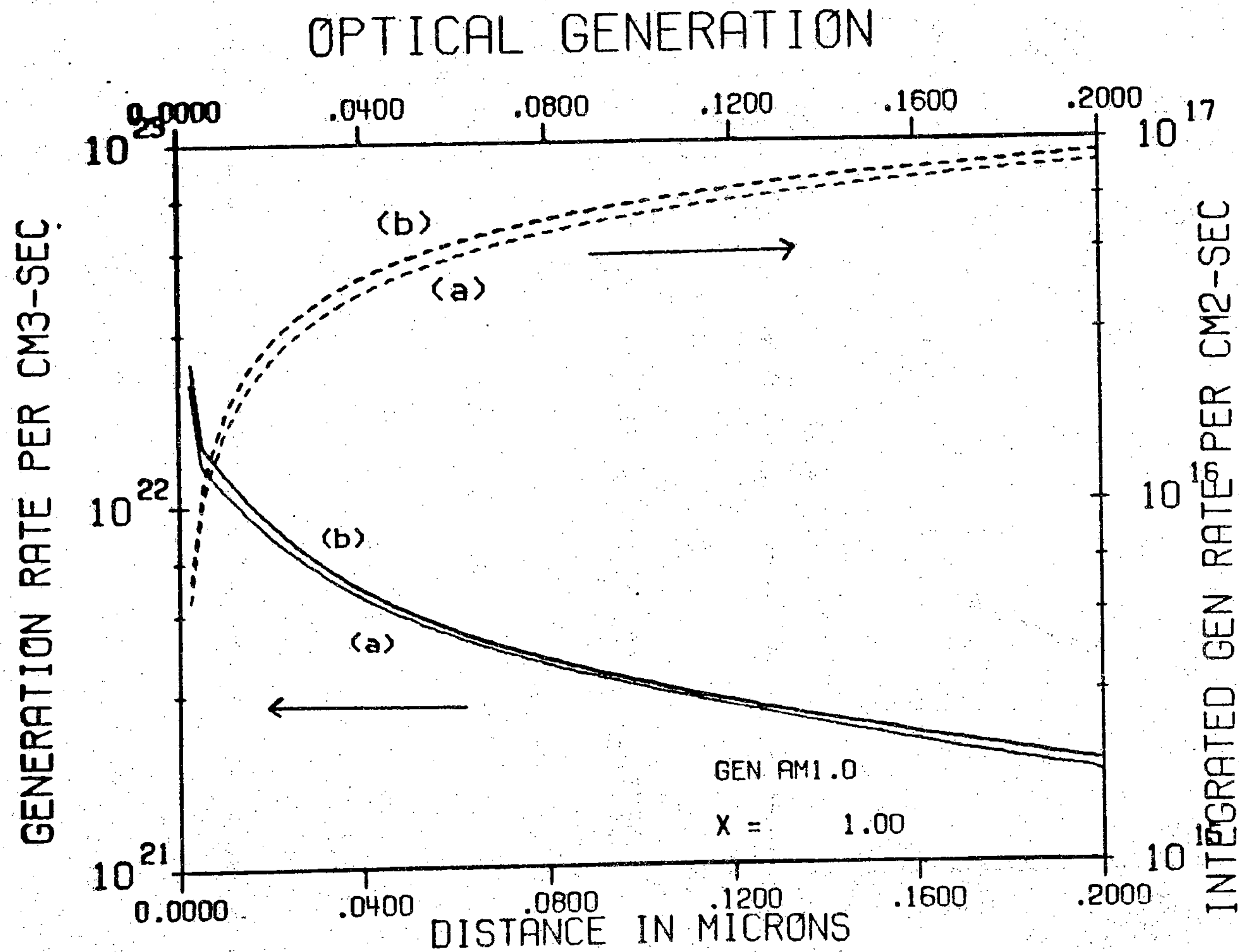

Figure 4.1.5 Optical Generation Rate, a) Include Reflection in SCAP1d, b) Lump Reflection in a 10% Shadow Factor

obtained with a different choice of shadow factor, however this introduces one more adjustable parameter in the simulations. As indicated in Section 3.3 the calculation of the reflection coefficient is computationally trivial. Therefore if the models for refractive indices and extinction coefficients are relatively simple, the software overhead of including reflection within the program is minimal.

Table 4.5 Results of SCAP1D Simulations Using Internal Reflectance Routine and Lumped Shadow Factor

	J_{SC}	V_{OC}	η	FF
SCAP1D Reflection	24.6 mA	0.98 V	21%	.83
SCAP1D No Reflection	26.1 mA	0.986	22.4%	.83

A modeling program such as SCAP1D displays its greatest value when it allows a cell designer to make an observation about a cells operation, use that observation to make a design change, and test that change by simulating the new structures. An observation that can be made of the shallow homojunction cell is that the spectral response curve indicates that there is still substantial loss due to surface recombination at the shorter wavelength (< 0.55 λm)

portion of the spectrum. Intuitively, a field built into the emitter should improve the short wavelength response and could be obtained relatively easily by an erfc doping profile. Results of a simulation using parameters identical to those employed in simulating the step junction are displayed in Table 4.6. The only difference was that an erfc doping profile was specified.

Table 4.6 Results of SCAP1D Simulations Using a Step Junction Profile and an Erfc Profile

	J_{SC}	V_{OC}	η	FF
SCAP1D step	24.6 mA	.98 V	21.1%	.83
SCAP1D erfc	26.0 mA	.97 V	22.1%	.84

What we observe is not only an improvement of roughly 5%, but but also the promise for further optimization since the field in the front layer could allow the use of a thicker emitter. This change would not only increase the absorbing volume, but would also reduce the sheet resistance of the emitter layer.

4.2 Fan-Bozler Cell /No AR Coating

Following the somewhat unsatisfactory treatment of the spectral response for the Fan-Bozler homojunction and the uncertainty about the oxide thickness, a very similar cell was found in the literature [75]. Fortuitously, this cell was also fabricated by the Fan and Bozler group and the cell parameters are given in Table 4.8. Note the lower base doping levels and deeper pn junction. Because of the free emitter surface, a slightly higher surface recombination velocity was used (4.0×10^6 cm/s), but the minority carrier lifetimes remained the same as those for the previous cell. Results of the solar cell simulation are found in Table 4.7.

Table 4.7 Results of SCAP1D Simulation of Fan-Bozler Cell Without an AR Coating

	J_{SC}	V_{OC}	η	FF
Fan & Bozler	19.2 mA	0.95 V	10.9	.81
SCAP1D	19.1 mA	0.92 V	10.7	.82

All simulated values are within 3% of those of the cited experimental work. These results are most encouraging since they clearly demonstrate that the

Table 4.8 **Parameters Used to Simulate a Fan-Bozler Cell Without an AR Coating**

Parameter	Value
Temperature	$25° C$
PN Junction Depth	$0.10\ \mu m$
High-Low Junction Depth	$1.1\ \mu m$
Device Length	8.0
Emitter Doping	$5.0\times10^{18} cm^{-3}$
Base Doping	$1.0\times10^{16} cm^{-3}$
Substrate Doping	$5.0\times10^{16} cm^{-3}$
Surface Recombination Velocity, S_F	$4.0\times10^{6}\ cm/sec$
Electron Minority Carrier Lifetime, τ_n	2.0 ns
Hole Minority Carrier Lifetime, τ_p	4.5 ns
Oxide Thickness	$0.0\ \mu m$
Solar Spectrum	AM0

code can be readily applied within a given family of cells. The crucial test was an examination of the spectral response characteristics. With the elimination of the uncertainty introduced by the oxide layer, excellent agreement was obtained (Figure 4.2.1). These results further indicate that there may have been some error in the specification of the spectral response curve for the previously discussed cell.

4.3 Borrego p^+n Cell

Although SCAP1D has been shown to perform quite well in the simulation of a family of shallow homojunctions [4,75], it is desirable to show that the model also works well for cells built by other researchers. Toward that end a p^+n cell built by Borrego, et. al. [76] was examined. This cell was built using an entirely different fabrication technology. The emitter was formed by a zinc diffusion into a tellurium doped LEC n-GaAs substrate. An interesting feature of Zn diffusion into GaAs is that it approximates a step junction quite well [95]. Parameters used for the device model appear in Table 4.9, and results of the solar cell simulation appear in Table 4.10. Part of the discrepancy between the simulated and the experimental values can be attributed to the fact that an accurate model for the Sb_2O_3 anti-reflection coating has not yet been installed in SCAP1D.

Borrego did give us a useful point of reference, however. The internal quantum efficiency which they calculated from their measured external quantum efficiency corresponds to the spectral response computed with

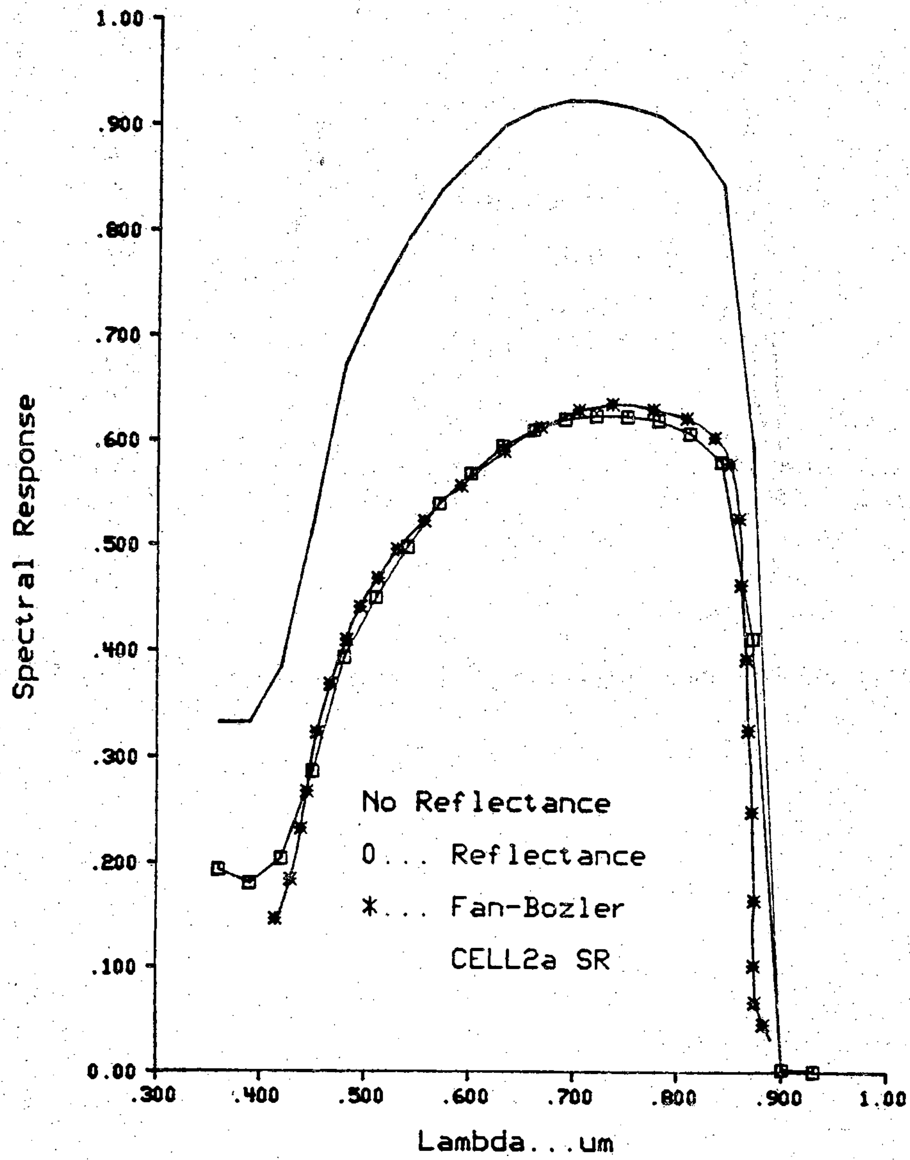

Figure 4.2.1 Spectral Response of Fan and Bozler Cell with no Anti-Reflection Coating

Table 4.9 Parameters Used to Simulate the Borrego p^+n Cell

Parameter	Value
Temperature	$25^{\circ} C$
PN Junction Depth	$0.10\ \mu m$
Device Length	8.0
Emitter Doping	$5.0\times10^{18} cm^{-3}$
Base Doping	$5.0\times10^{16} cm^{-3}$
Substrate Doping	$5.0\times10^{16} cm^{-3}$
Surface Recombination Velocity, S_F	$5.0\times10^{6}\ cm/sec$
Electron Minority Carrier Lifetime, τ_n	2.5 ns
Hole Minority Carrier Lifetime, τ_p	1.75 ns
Shadow Factor	10%
Solar Spectrum	AM1

Table 4.10 Results of SCAP1D Simulation of the Borrego Cell

	J_{SC}	V_{OC}	η	FF
Borrego	19.1 mA	0.921 V	12.6%	0.75
SCAP1D	19.2 mA	0.935 V	15.1%	.80

SCAP1D when shadowing and reflection are ignored. Figure 4.3.1 illustrates the excellent aggreement between our computed results and those of Borrego. It is encouraging to note that the code was able to reproduce the spectral response characteristics even though they differed considerably from those of the Fan and Bozler n^+p cells.

4.4 Sahai Heteroface

One of the most popular cells in the literature is the heteroface cell described in Chapter 1. For the purpose of modeling, it was desirable to find a heteroface cell with an anodic oxide AR coating. Unfortunately, all of the cells described in the literature had more sophisticated anti-reflection systems.

A cell which has been given an introductory treatment by SCAP1D is the cell of Sahai, et. al. [6]. For this particular cell the $Al_xGa_{1-x}As$ layer may be simply treated as an element of the anti-reflection system and the analysis may proceed as it did for the GaAs homojunction cells discussed earlier. Parameters describing the cell are found in Table 4.11. Note the extremely low value for reflectivity loss, 3%. Without the AR layers the loss due to reflection would be close to 30%. The preliminary solar simulation results for this cell appear in Table 4.12. Clearly, some work must be done to introduce loss mechanisms that would be responsible for reducing V_{OC}. Until other cells are investigated, however, it is unclear whether this discrepancy is related to the heteroface or to some process related phenomena. It will be interesting to see if this pattern for overestimating V_{OC} for p^+n cells persists, and if the code is able to model with

Table 4.11 Parameters Used to Simulate the Sahai Heteroface Cell

Parameter	Value
Temperature	$25^{\circ} C$
PN Junction Depth	1.50 μm
Device Length	8.0
Emitter Doping	$2.0\times10^{18} cm^{-3}$
Base Doping	$1.0\times10^{18} cm^{-3}$
Substrate Doping	$1.0\times10^{18} cm^{-3}$
Surface Recombination Velocity, S_F	1.0×10^{4} cm/sec
Electron Minority Carrier Lifetime, τ_n	1.75 ns
Hole Minority Carrier Lifetime, τ_p	1.0 ns
Shadow Factor	3%
Solar Spectrum	AM0

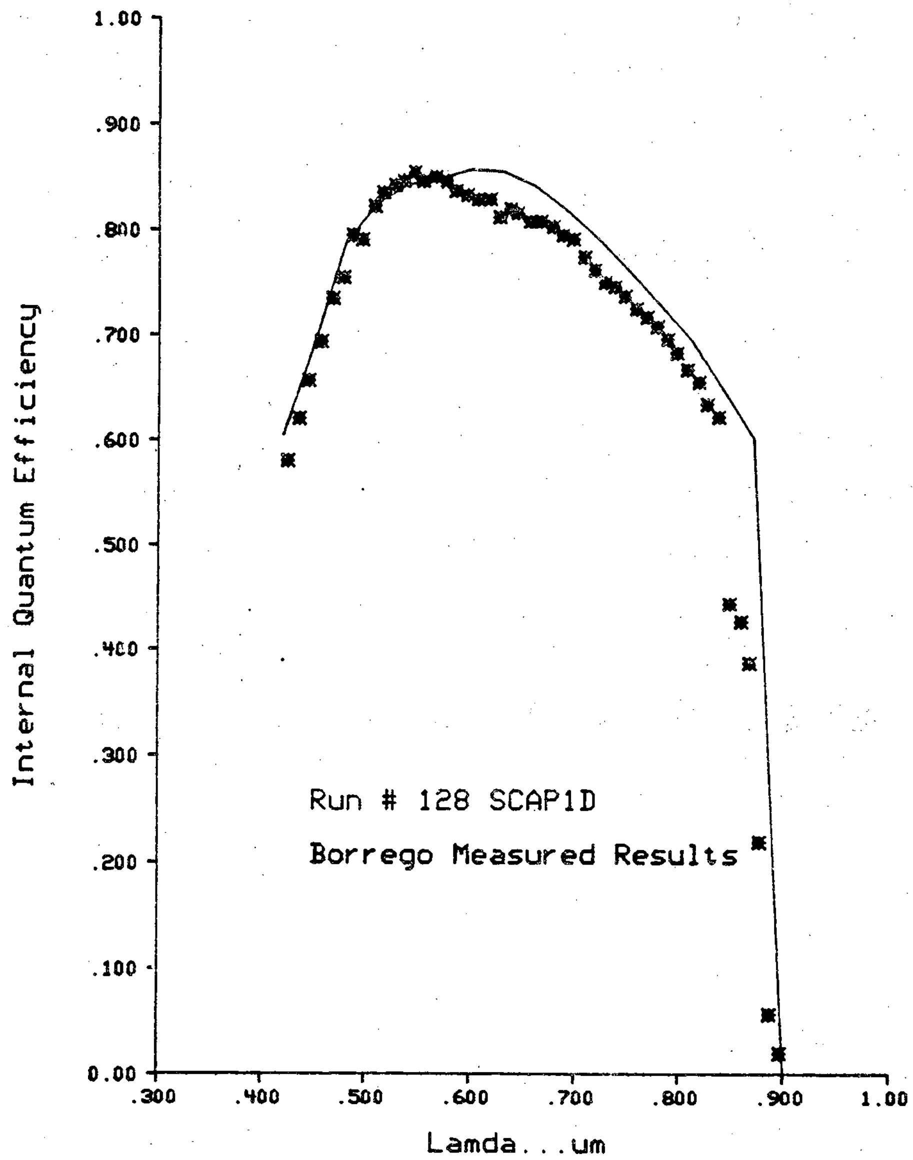

Figure 4.3.1 Internal Quantum Efficiency of Borrego Cell

better accuracy n^+p heteroface cells. If this is the case an in depth investigation of heavily doped p-type material may be in order.

Table 4.12 Results of SCAP1D Simulation of the Sahai Heteroface Cell

	J_{SC}	V_{OC}	η	FF
Sahai	30.3 mA	0.96 V	17.2%	.803
SCAP1D	30.4 ma	1.02 V	19.2%	.833

4.5 Summary

This chapter has illustrated some of the results from SCAP1D simulations of four GaAs solar cells described in the literature. It was shown that SCAP1D, with extensions, models a family of GaAs homojunctions quite well and has the potential to treat a class of heteroface cells, as well. The work on the Sahai cell indicates that other heteroface cells need to be examinined before the success of the model may be evaluated. It also suggests that further work on heavy-doping effects in p-type material needs to be considered. A brief discussion of the effects of introducing a built-in field in the emitter of the shallow homojunction cell of Fan and Bozler was also presented.

CHAPTER 5
OPEN-CIRCUIT VOLTAGE ENHANCEMENT IN GRADED GAP CELLS

5.1 Introduction

The application of graded bandgap materials to the design of efficient photovoltaic devices has generated considerable interest since the late 1950's[96, 97]. The success achieved in gallium arsenide (GaAs) homojunction[98, 99] and heteroface[100, 101, 102] solar cells has encouraged investigations of structures using the aluminum gallium arsenide/gallium arsenide ($Al_xGa_{1-x}As/GaAs$) material system. The evolution of fabrication technologies such as liquid phase epitaxy (LPE)[103], molecular beam epitaxy (MBE)[104], and organometallic vapor phase epitaxy (OMVPE)[105, 106] has reached a level where proposed device structures may be routinely investigated. In evaluating these structures, however, it is important to bear in mind that the increased complexity of fabrication and the associated high costs make these cells most appropriate for concentrator applications.

There are two advantages to be gained from a graded bandgap structure. The first of these is an increase in collection efficiency through field-assisted collection[107]. The majority of the graded-gap cells presented in the literature have been designed to take advantage of this effect[103, 107, 108, 109, 110, 111].

The second advantage is the enhancement of the open circuit voltage resulting from an additional photovoltage produced across the graded region[96]. This paper examines the criteria associated with the production of such V_{oc}–enhancement.

While this phenomenon has been experimentally observed for compositionally graded p-type $Al_xGa_{1-x}As$ structures[112] and for graded mercury cadmium telluride ($Hg_{1-x}Cd_xTe$)[113], its application to anisotype heterostructure solar cells has not been realized. Although numerous authors have analytically analyzed the problem[96, 97, 108, 109, 110, 113, 114, 115], no consensus regarding the magnitude of the V_{oc} enhancement has been reached. Some authors[108, 109, 110] view the chief advantage of a graded bandgap solar cell to be its ability to increase the collection efficiency and have predicted only minor increases in V_{oc} resulting from the grading. Other authors[96, 97, 113, 114, 115] predicted that properly designed cells will display a significant increase in V_{oc} leading to very high conversion efficiencies. The disparity in these results is a consequence of the differing approximations each author used in his device model.

In this study, numerical methods are used in order to remove as many simplifications as possible. Similar numerical techniques have already proven themselves to be useful in examining silicon[116] and GaAs[117] homostructure and $Al_xGa_{1-x}As$ heterostructure[118, 119, 120] solar cells. The latter work, however, has not addressed the enhanced V_{oc} effect. It is the goal of this work to realistically assess the possibility of using the V_{oc} enhancement provided by the graded bandgap to achieve high conversion efficiencies.

In the following section a simplified analytical treatment of a graded bandgap cell is used to establish the conditions under which open circuit voltage enhancement is possible. Next, a numerical simulator is described and used to examine the performance of an idealized graded bandgap $Al_xGa_{1-x}As$ heterostructure solar cell. This analysis shows that V_{oc}–enhancement occurs, but in Sec. 4 we show that for a practical cell design, V_{oc}– enhancement is minimal. Furthermore, to optimize the cell, one is driven to designs that further reduce the V_{oc} enhancement. Consequently, it is concluded that the preferred use of bandgap grading is to enhance photocollection not V_{oc}.

5.2 Origin of the Graded Bandgap Photovoltage

Figure 5.2.1 is an equilibrium band diagram for a linearly graded P–$Al_xGa_{1-x}As$/n–GaAs structure for which the doping profiles are assumed to be uniform and the metallurgical junction is coincident with the compositional junction. Because of the difference in diffusion constants for holes and electrons the carriers diffuse at different rates creating charge separation that is responsible for the well-known Dember potential. In addition to diffusion, the electrons also experience a field due to the gradient in the conduction band ($\vec{\mathcal{E}}_n = \partial E_C/\partial x$). The holes, however, experience no field since the valence band edge is essentially flat. As the junction is forward biased and minority carrier electrons are injected into the graded gap region, the gradient of the conduction band is moderated and a photovoltage develops. As demonstrated below, the photovoltage occurs across that portion of the graded gap region that is in high-level injection.

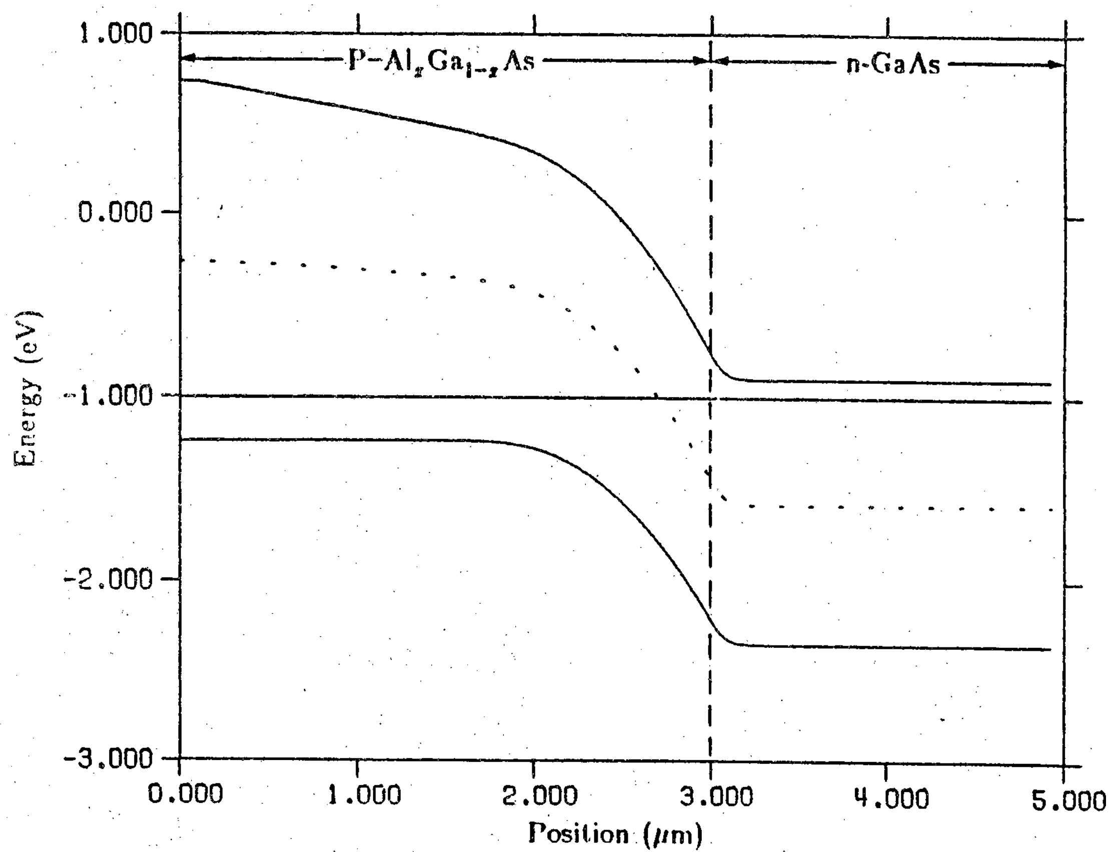

Figure 5.2.1 Graded bandgap solar cell equilibrium energy band diagram.

The electron and hole current densities in a material with a position dependent composition are given by[121, 122, 123]

$$J_n = -nq\mu_n \nabla(V+V_n) + kT\mu_n \nabla n \quad (5.2.1)$$

and

$$J_p = -pq\mu_p \nabla(V-V_p) - kT\mu_p \nabla p \quad (5.2.2)$$

where V is the electrostatic potential, n and p are the electron and the hole concentrations, q is the magnitude of the charge on an electron, and μ_n and μ_p are the electron and hole mobilities. The position dependence of the composition is reflected in the band parameters, V_n and V_p. They are calculated from the material parameters (assuming Boltzmann statistics) as

$$qV_n(x) = \chi(x) - \chi_{ref} + kT \ln\left[\frac{N_C(x)}{N_{Cref}}\right] \quad (5.2.3)$$

and

$$qV_p(x) = -(\chi(x) - \chi_{ref}) - (E_G(x) - E_{Gref}) + kT \ln\left[\frac{N_V(x)}{N_{Vref}}\right] \quad (5.2.4)$$

where χ is the electron affinity, N_C and N_V are the conduction and valence band effective density of states, E_G is the bandgap, and the subscript "ref" refers to the value of that material parameter in an intrinsic reference material in which the zero of potential is defined. The gradients of the band parameters, $-\nabla V_n$ and ∇V_p, yield the quasi-fields which result from the variation of the composition. The carriers will experience these quasi-fields in addition to the normal electric field, $-\nabla V$.

Consider the device structure depicted in Fig. 5.2.2 corresponding to a P–$Al_xGa_{1-x}As$/n–GaAs structure. In equilibrium $J_p = 0$ and $dp/dx=0$ in the

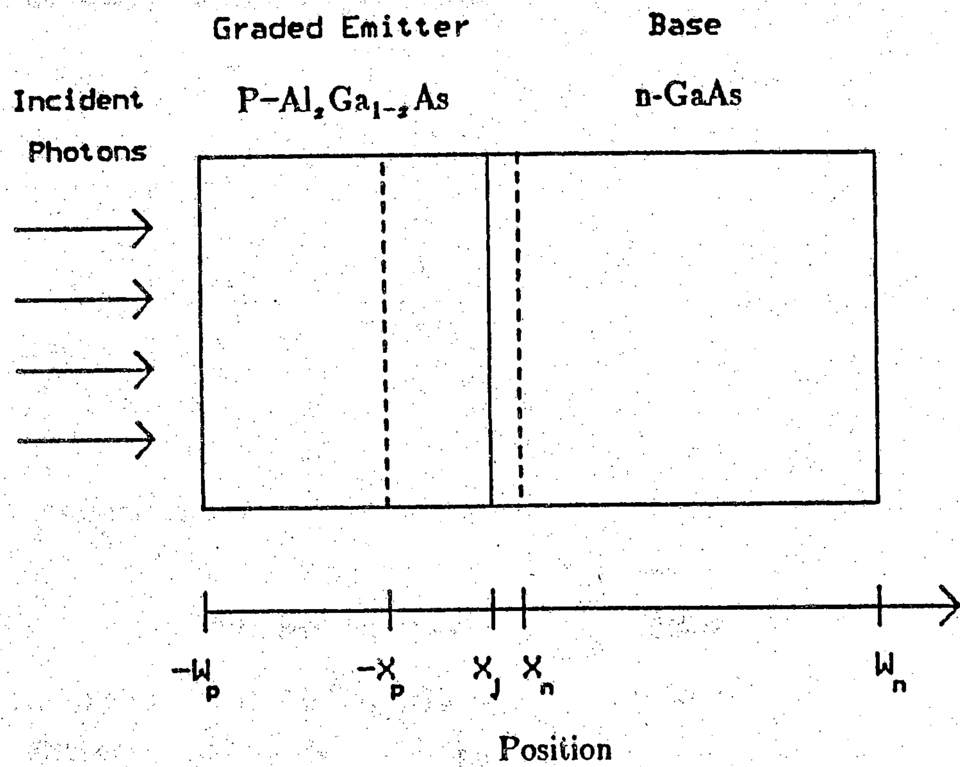

Figure 5.2.2 Schematic device representation.

uniformly doped P-region so that (5.2.2) can be solved for

$$\frac{\partial V_o}{\partial x} = \frac{\partial V_p}{\partial x} \tag{5.2.5}$$

where V_o is the equilibrium potential. Consequently, the equilibrium voltage drop across the p-type quasi-neutral region can be expressed as

$$\Delta V_o = V_o(-W_p) - V_o(-x_p) = V_p(-W_p) - V_p(-x_p)\ . \tag{5.2.6}$$

Under non-equilibrium conditions the total current is given by

$$J_T = J_n + J_p$$

$$= -q(n\mu_n + p\mu_p)\frac{\partial V}{\partial x} - qn\mu_n\frac{\partial V_n}{\partial x} + qp\mu_p\frac{\partial V_p}{\partial x}$$

$$+ kT(\mu_n\frac{\partial n}{\partial x} - \mu_p\frac{\partial p}{\partial x})\ . \tag{5.2.7}$$

Solving this expression for the non-equilibrium electric field results in

$$-\frac{\partial V}{\partial x} = \frac{J_T}{\sigma} + \frac{1}{1 + \frac{p}{nb}}\frac{\partial V_n}{\partial x} - \frac{1}{1 + \frac{nb}{p}}\frac{\partial V_p}{\partial x}$$

$$- \frac{kT}{q}\left[\frac{\frac{1}{n}\frac{\partial n}{\partial x}}{1 + \frac{p}{nb}} - \frac{\frac{1}{p}\frac{\partial p}{\partial x}}{1 + \frac{nb}{p}}\right] \tag{5.2.8}$$

where $\sigma = q(n\mu_n + p\mu_p)$ and $b = \mu_n/\mu_p$. *Assuming high-level injection* (n=p) and constant mobilities, the integral of (5.2.8) over the p-side quasi-neutral region yields the potential difference

$$\Delta V = \int_{-x_p}^{-W_p} \frac{\partial V}{\partial X}\, dx$$

$$= J_T R - \frac{1}{1+b}\left[V_p(-x_p) - V_p(-W_p)\right]$$

$$+ \frac{1}{1+\frac{1}{b}}\left[V_n(-x_p) - V_n(-W_p)\right]$$

$$+ \frac{kT}{q}\left[\frac{1}{1+b} - \frac{1}{1+\frac{1}{b}}\right] \ln\frac{p(-x_p)}{p(-W_p)}$$

$$= J_T R + \frac{b}{b+1}\left[V_G(-x_p) - V_G(-W_p)\right]$$

$$- \frac{kT}{q}\left(\frac{b-1}{b+1}\ln\frac{p(-x_p)}{p(-W_p)}\right) \qquad (5.2.9)$$

where $R = \int_{-x_p}^{-W_p} \frac{dx}{\sigma}$ and $V_G = V_p + V_n$. The photovoltage across the region is given by the difference of the equilibrium voltage drop and (5.2.9). Thus,

$$\Delta V_{photo} = \Delta V - \Delta V_o$$

$$= J_T R + \frac{\Delta V_G}{1+\frac{1}{b}} - \frac{kT}{q}\,\frac{b-1}{b+1}\int\frac{dp}{p}\,. \qquad (5.2.10)$$

Following a similar development for an N–$Al_xGa_{1-x}As$/p–GaAs structure results in a photovoltage of

$$\Delta V_{photo} = J_T R + \frac{\Delta V_G}{1 + b} + \frac{kT}{q}\,\frac{b - 1}{b + 1}\int \frac{dn}{n} . \qquad (5.2.11)$$

In both (5.2.10) and (5.2.11) the first term on the right hand side represents resistive losses in the bulk, the second term denotes the photovoltage available from the bandgap grading, and the third represents the usual Dember potential. An examination of (5.2.10) and (5.2.11) reveals that the Dember potential is unlikely to contribute significantly to the photovoltage across the region since its magnitude is on the order of only a few kT/q 's. However, it is apparent that the graded-gap photovoltage may be significant, particularly for materials with larger electron to hole mobility ratios. It is also clear from these equations that this effect is more important for P–$Al_xGa_{1-x}As$/n–GaAs structures than for N–$Al_xGa_{1-x}As$/p–GaAs structures. Furthermore, since this cell-type is being considered for concentrator applications for which the current densities may be quite large, the resistive terms in (5.2.10) and (5.2.11) could adversely effect the performance of the cell.

The necessity of high-level injection and the detrimental effects of series resistance were established in the analytical model described above. This model is limited, however, by the assumption of high-level injection throughout the graded gap region and by the difficulty of evaluating the conductivity-modulated resistance. In order to accurately assess cell performance, the device simulation program described in the next section was applied to this problem.

5.3 Numerical Simulation of Heterostructures

The graded bandgap $Al_xGa_{1-x}As/GaAs$ solar cell examined in this study was simulated using a one-dimensional numerical device model called PUPHS (Purdue University Program for Heterostructure Simulation)[121, 122, 123]. This program uses the technique of finite differences on a variable mesh and Newton-Raphson iteration [124] to solve Poisson's equation and the two current continuity equations. These equations have been appropriately modified to account for the position dependent material parameters. A detailed description of the material models, which are similar to Sutherland and Hauser's[118, 119, 120], can be found in[123]. Although the models have generally been updated, one important improvement lies in the calculation of the optical generation rate (optical generation is the only generation mechanism considered). This includes improved models for the optical parameters and a generation calculation scheme which considers not only the position dependence of the coefficient of absorption, but internal reflection (resulting from the variation of the index of refraction) as well.

While different material grading profiles are available as options in the program, the particular one used in this analysis assumes a linear variation of the aluminum content (this does not necessarily imply a linear variation of the bandgap). As a result, the variation of the composition is slow and prevents the formation of spikes in the band edges. As a consequence, the effective fields encountered in this structure are sufficiently small that a field-dependent mobility model is not required[123]. Finally, the program allows the specification of ohmic boundary conditions or of a surface recombination velocity to take account of surface recombination as well as Shockley-Read-Hall recombination in the bulk.

5.4 Results of the Numerical Simulation

As indicated in Sec. 5.2, the final analytical results, (5.2.10) and (5.2.11), are obtainable only if high level injection is assumed (the effect is negligible in low level injection). Unfortunately, the very structure utilized to achieve the enhancement also works against it. The rather large effective field created by the grading tends to sweep electrons towards the junction and, thereby, make the condition of high level injection difficult to achieve. By heavily doping the base (the n-GaAs) and lightly doping the emitter, minority carrier injection into the graded emitter (essential for V_{oc}-enhancement) is promoted.

Figure 5.4.1 illustrates a simple structure for achieving the enhanced V_{oc}. Table 5.1 contains additional information pertinent to the device. In the ensuing analysis an anti-reflection coating which allows a 3% reflection loss and Boltzmann statistics for carriers have been assumed. The essential difference between the simplified structure and those proposed in the literature[103, 105, 110] is the low doped emitter. As Hutchby has pointed out[110], however, the use of a low doped emitter can result in a large series resistance which will degrade the fill-factor of the cell.

Figure 5.4.2 shows V_{oc} versus intensity for the graded gap cell described above and for a similar cell with a more heavily doped ($N_A = 10^{17}/cm^3$) emitter. While V_{oc}-enhancement occurs for the cell with the lightly doped emitter, the improvement is not substantial until very high (more than 1000 suns) concentrations. By correlating Fig. 5.4.3a-5.4.3c with Fig. 5.4.2, it can be seen that the enhancement of V_{oc} is, as anticipated, coincident with the onset of high level injection in the graded gap emitter.

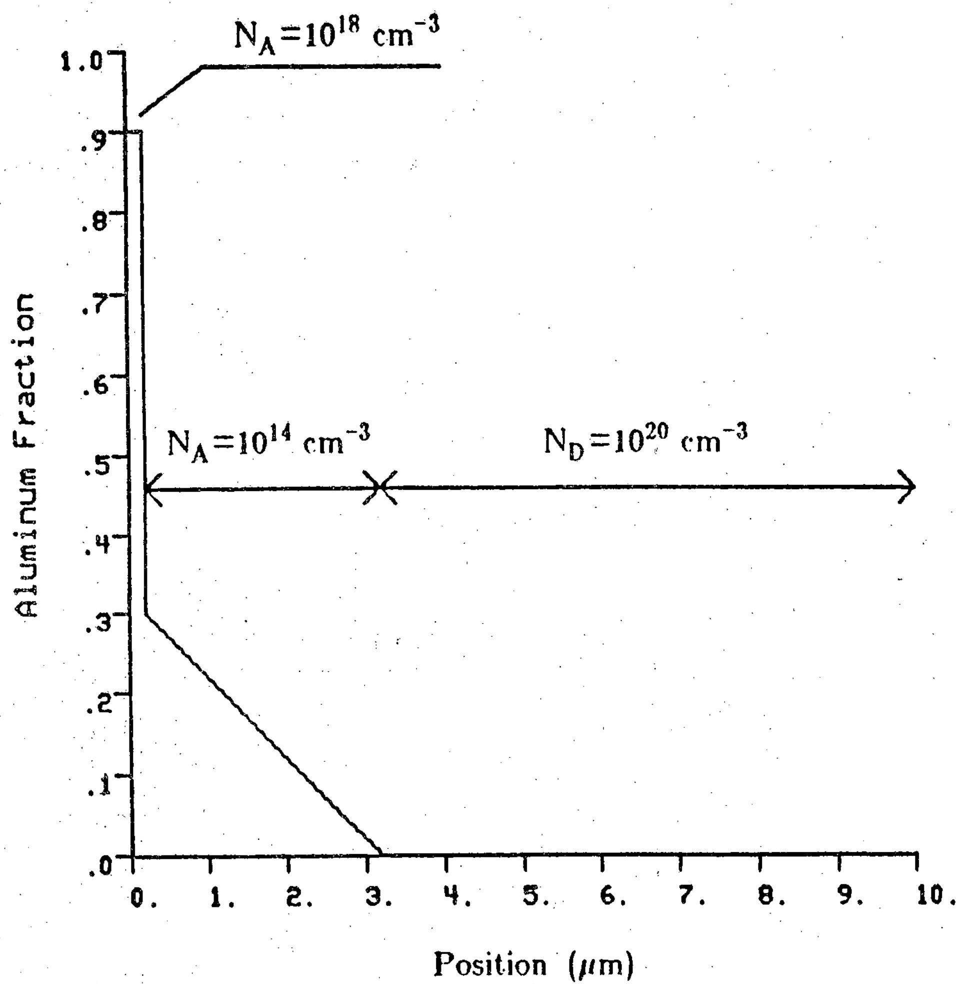

Figure 5.4.1 Device structure of a graded gap solar cell designed to illustrate V_{oc}-enhancement.

Table 5.1 Additional information for the simplified cell.

Temperature	300 K
S_F	10^4 cm/sec
S_B	∞
$\tau_{n\ AlAs}$	2.0 ns
$\tau_{n\ GaAs}$	3.0 ns $N_{AE}=10^{18}$ cm^{-3}
	4.5 ns $N_{AE}=10^{14}$ cm^{-3}
$\tau_{p\ GaAs}$	2.0 ns
$\tau_{p\ AlAs}$	1.0 ns

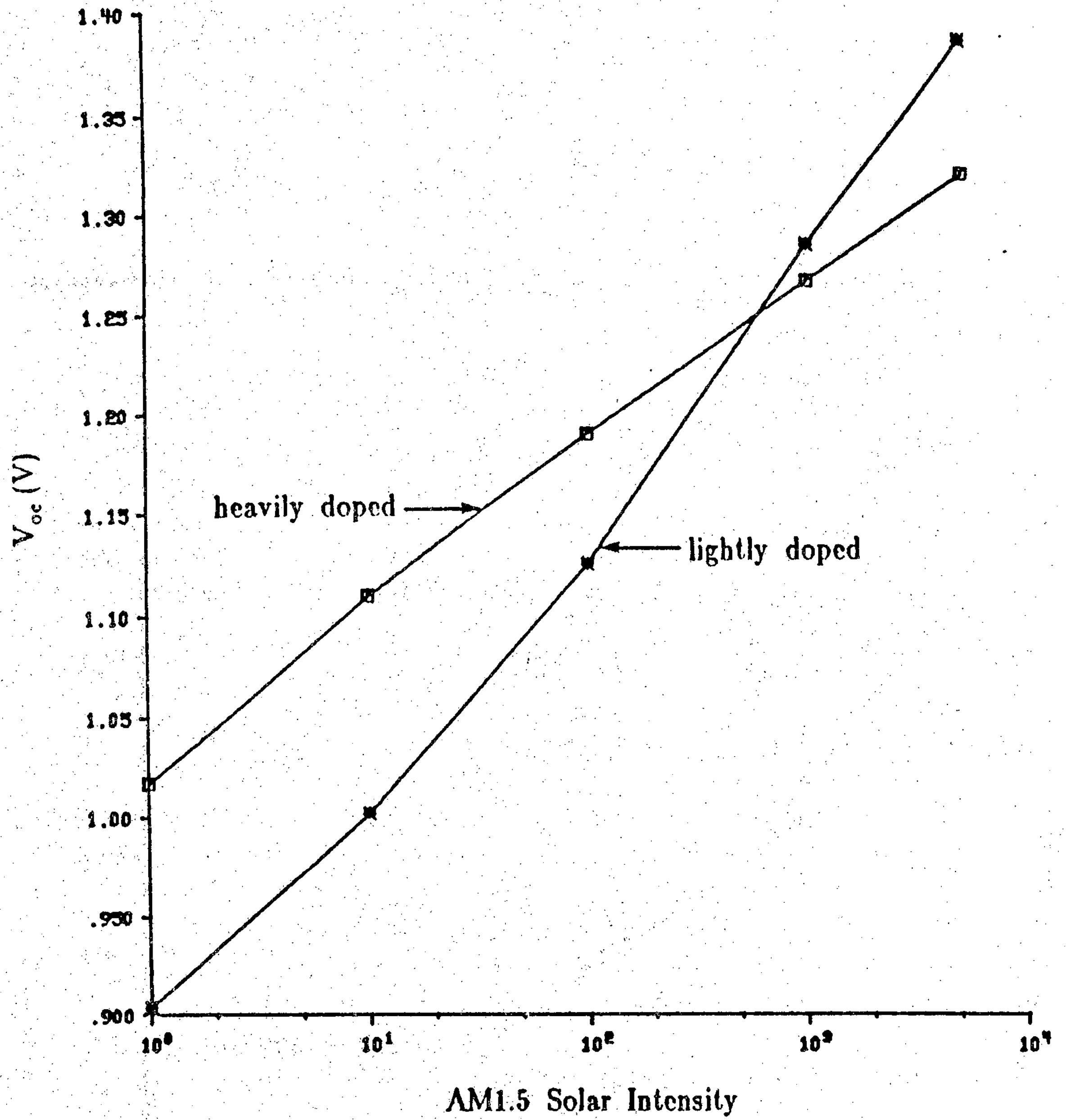

Figure 5.4.2 V_{oc} versus solar intensity for the simple cell.

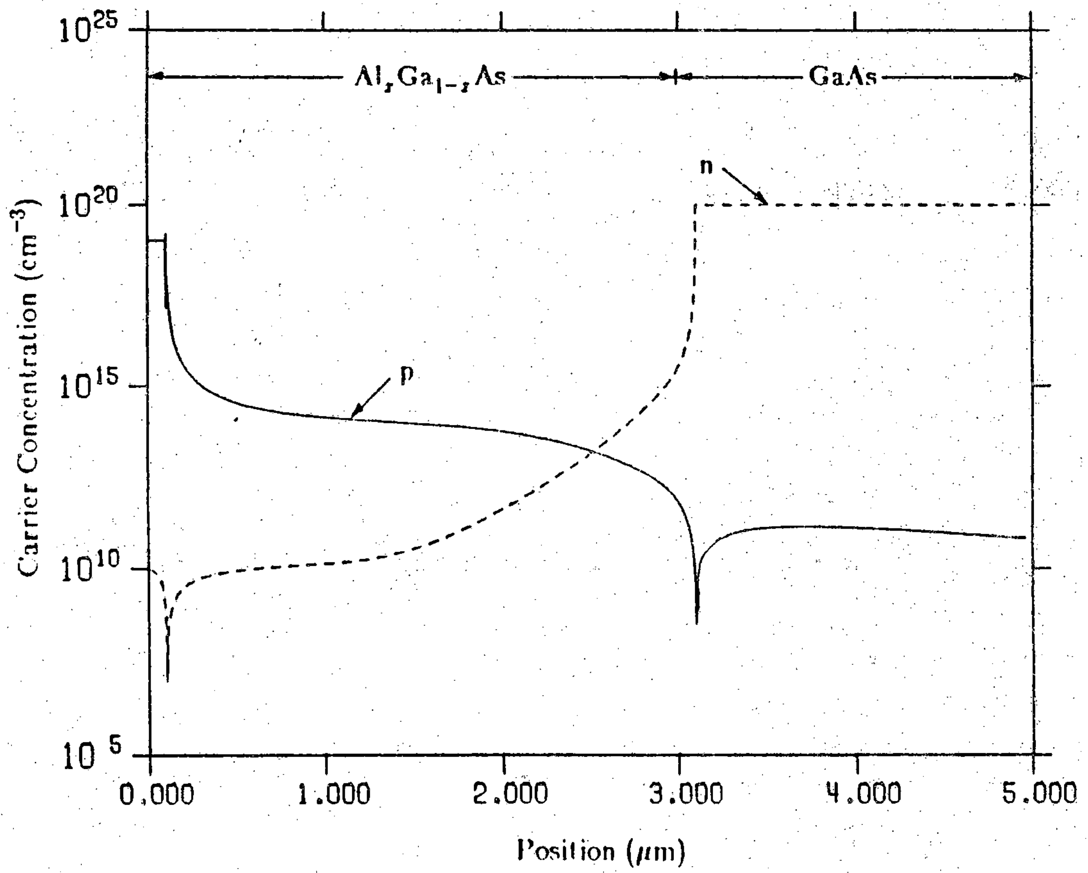

Figure 5.4.3a 1 sun intensity carrier concentration at Voc.

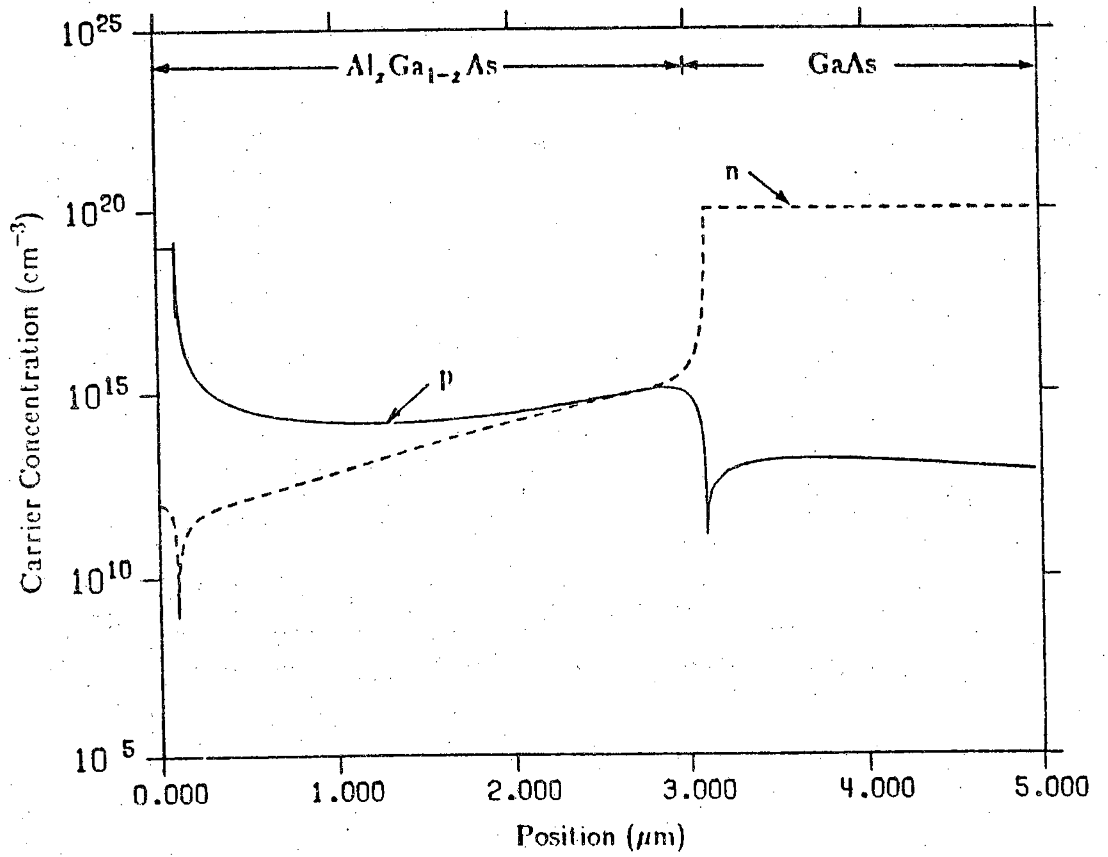

Figure 5.4.3b 1000 sun intensity carrier concentration at Voc.

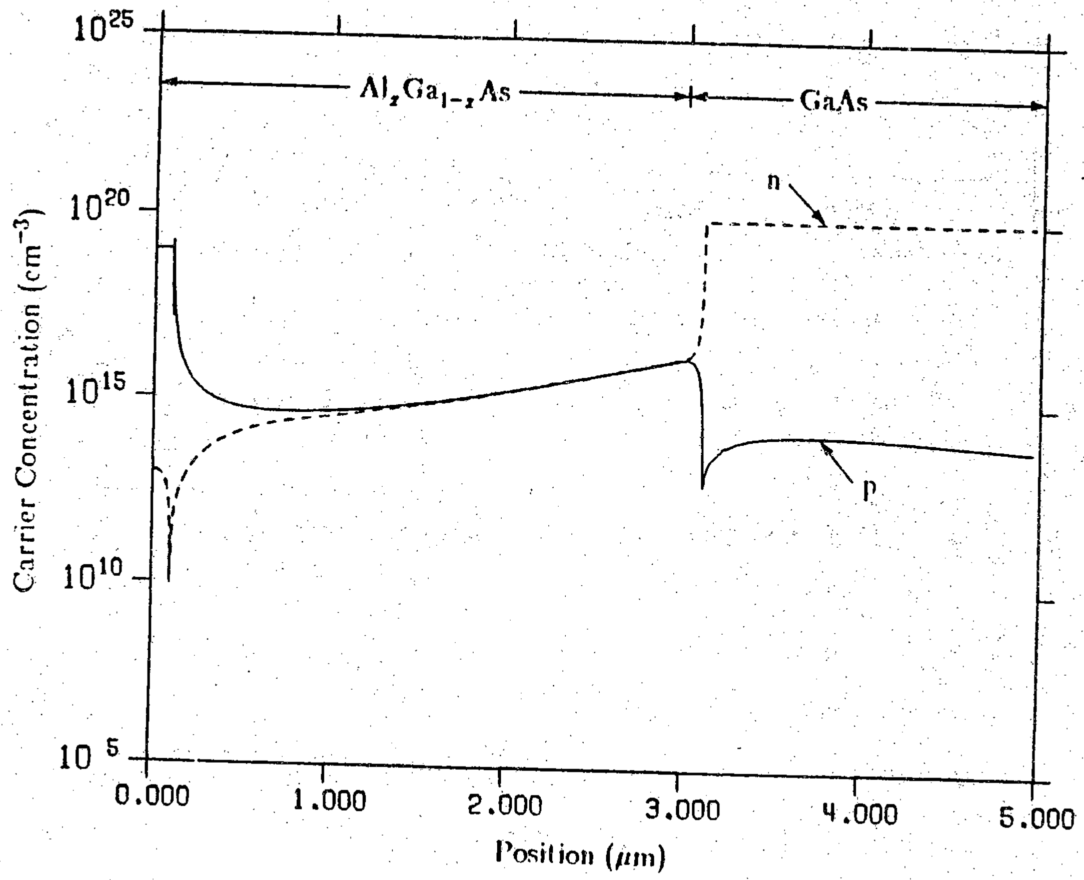

Figure 5.4.3c 5000 sun intensity carrier concentration at Voc.

While this example illustrates that substantial V_{oc} enhancement can occur in graded bandgap cells, the design cannot be considered practical. To drive the graded region into high level injection, a very light emitter doping (1×10^{14} cm^{-3}) was used (even for this light doping, solar intensities in excess of 1000 suns were required). Since the resistance of the emitter is high (conductivity modulation occurs only near V_{oc}), the fill factor (FF) is severely degraded. (At 5000 suns, for example, FF=0.59 for the cell with light emitter doping and FF=0.87 for the cell with heavier emitter doping). The fill factor is even worse if the lateral component of the series resistance (due to the sheet resistance of the emitter) is included.

5.5 Cell Design and Optimization

A more realistic graded gap cell design is considered in this section. The doping densities of the above-described cell were adjusted to more technologically feasible values and a thick, heavily doped window layer was introduced to reduce the emitter sheet resistance. The revised structure and pertinent information appear in Fig. 5.5.1 and Table 5.2. The emitter doping used is a compromise between a low concentration to permit high level injection and a larger value to reduce emitter resistance. Lower doping levels resulted in a significant ohmic drop across the emitter. The thickness of the graded region was a compromise between a large value to maximize the number of photogenerated carriers and a small value to minimize the resistance of the lightly doped region. The window layer thickness and its doping level are comparable to those used in practice[101].

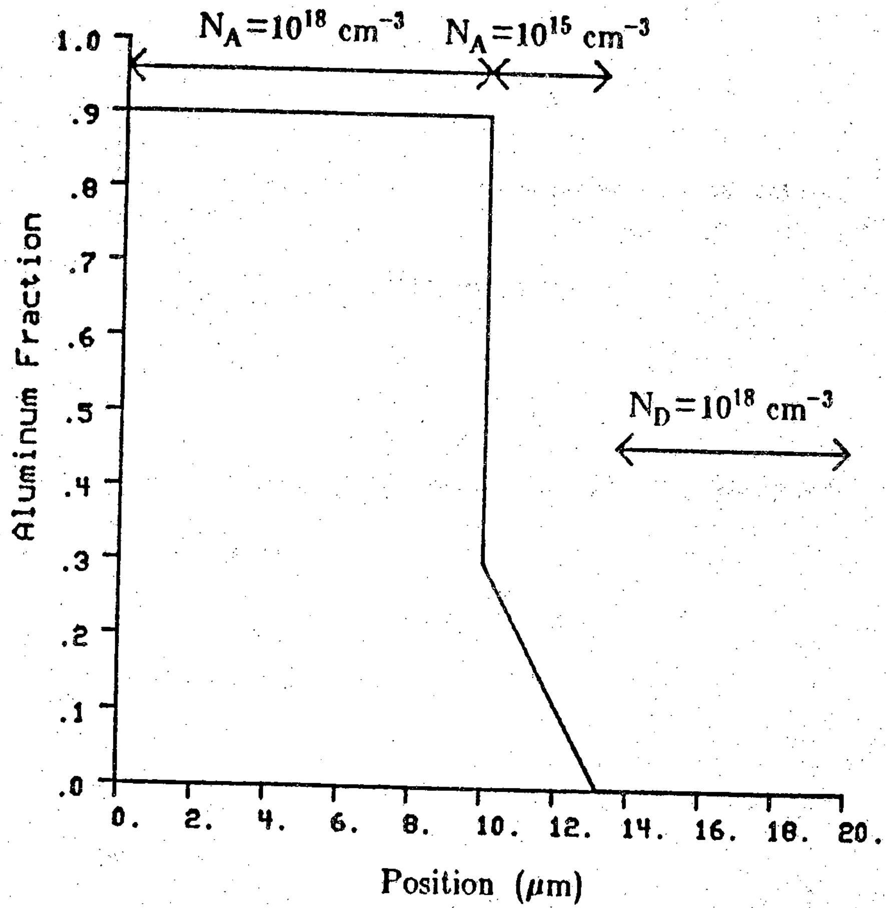

Figure 5.5.1 Device structure of a graded gap solar cell designed for reduced series resistance.

Table 5.2 Additional information for the practical cell.

Temperature	300 K
S_F	10^4 cm/sec
S_B	∞
$\tau_{n\,AlAs}$	2.0 ns
$\tau_{n\,GaAs}$	3.0 ns $N_{AE}=10^{17}$ cm^{-3}
	4.5 ns $N_{AE}=5\times10^{15}$ cm^{-3}
$\tau_{p\,GaAs}$	2.0 ns
$\tau_{p\,AlAs}$	1.0 ns

Figure 5.5.2, a plot of V_{oc} versus solar intensity, shows that V_{oc} enhancement also occurs for this cell. Due to the higher emitter doping, however, the solar intensity required for V_{oc}-enhancement is higher than for the cell described in the previous section. Moreover, while Fig. 5.5.2 shows substantial V_{oc} enhancement at 5000 suns concentration, Fig. 5.5.3 shows that a large drop in fill factor also occurs. The drop in fill factor is a result of a voltage drop across the lightly doped emitter.

To optimize the performance of this graded bandgap solar cell, one should reduce the voltage drop across its emitter. One technique is to reduce the thickness of the graded region, but short-circuit current may suffer because most photogeneration will occur in the heavily doped bulk. Figure 5.5.2 and 5.5.3 also show simulated results for a cell with higher emitter doping. As expected, the higher doping prevents the emitter from entering high injection so no V_{oc}-enhancement occurs. Despite the lack of V_{oc}-enhancement, Fig. 5.5.3 shows that the cell with the heavier emitter doping performs better at all solar intensities than the V_{oc} enhanced cell. Figure 5.5.4 shows the simulated I-V characteristic of this cell and compares the heavily and lightly doped emitter cells. The improved performance of the cell with a heavily doped emitter is due to the higher fill factor that results from the lower series resistance.

In summary, while V_{oc}-enhancement can occur in P–$Al_xGa_{1-x}As$:n–GaAs graded gap cells, very high solar intensities are required and fill factor degradation due to resistive losses is likely to occur. The fill factor is readily increased by raising the emitter doping - at the cost of eliminating V_{oc}-enhancement but with the result of raising the cell's efficiency. For such designs, the bandgap grading serves to enhance the cell's collection efficiency - not V_{oc}. When V_{oc}-enhancement is not sought, the N–$Al_xGa_{1-x}As$:p–GaAs cell

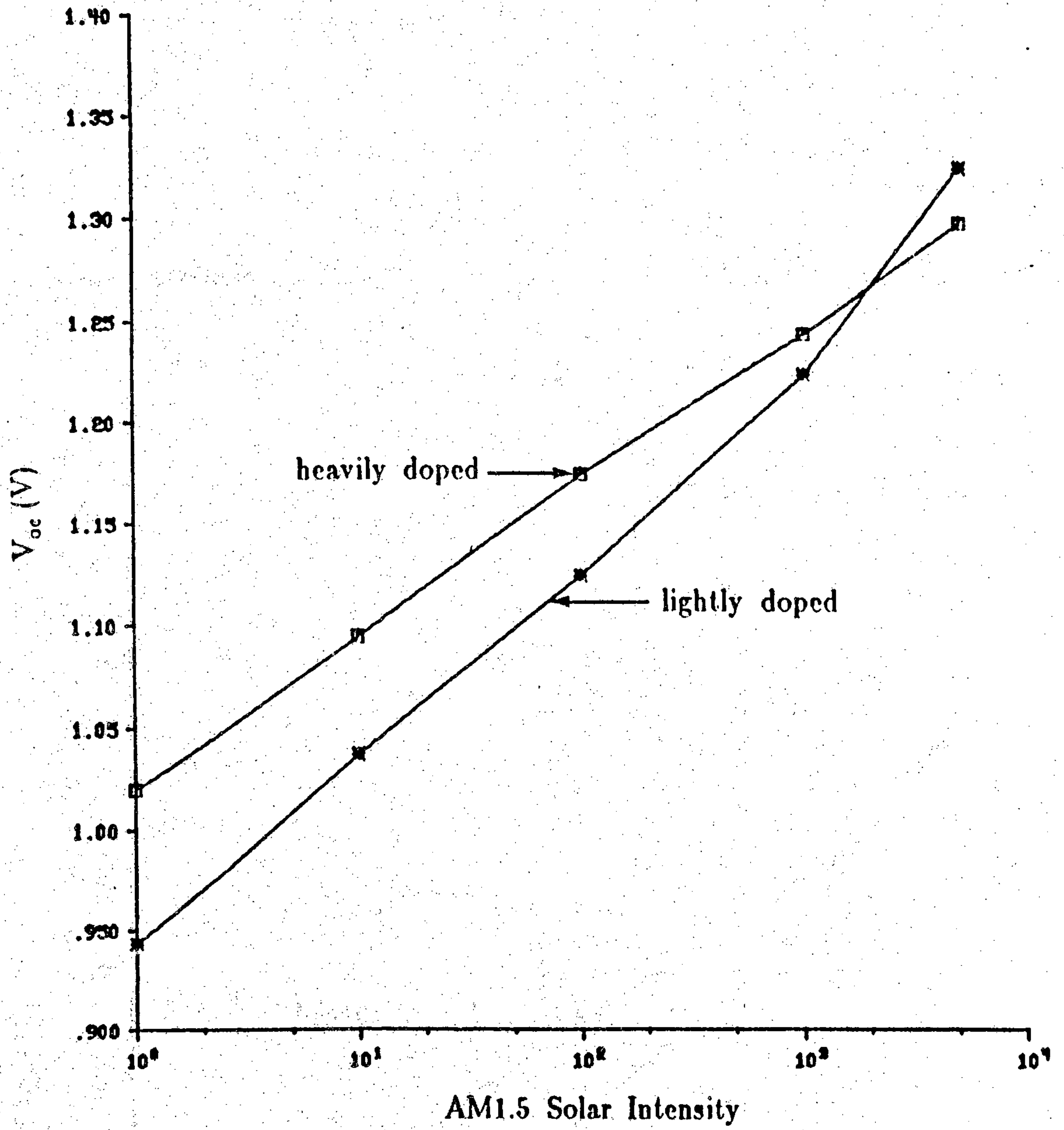

Figure 5.5.2 V_{oc} versus solar intensity for the practical cell.

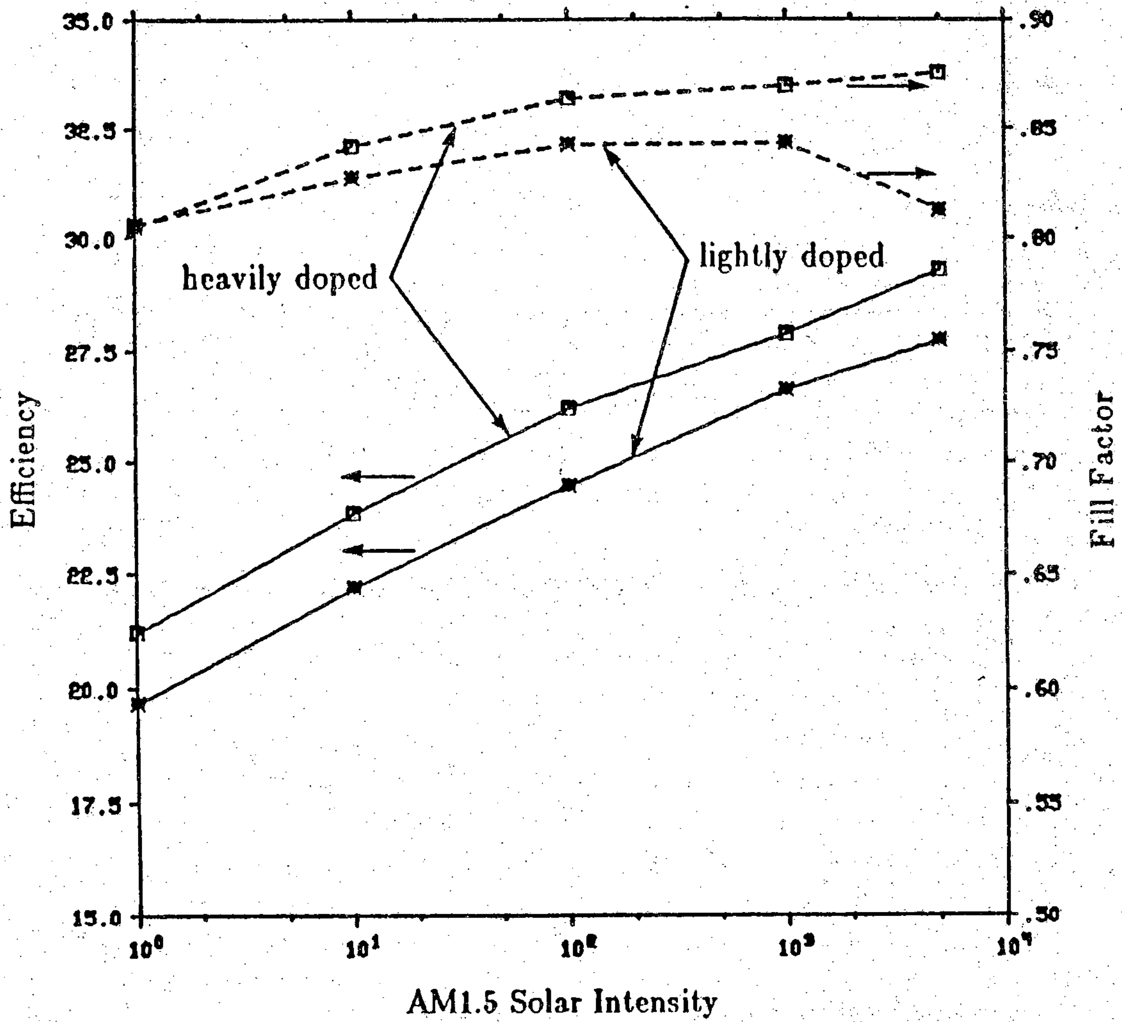

Figure 5.5.3 Fill factor and efficiency versus solar intensity.

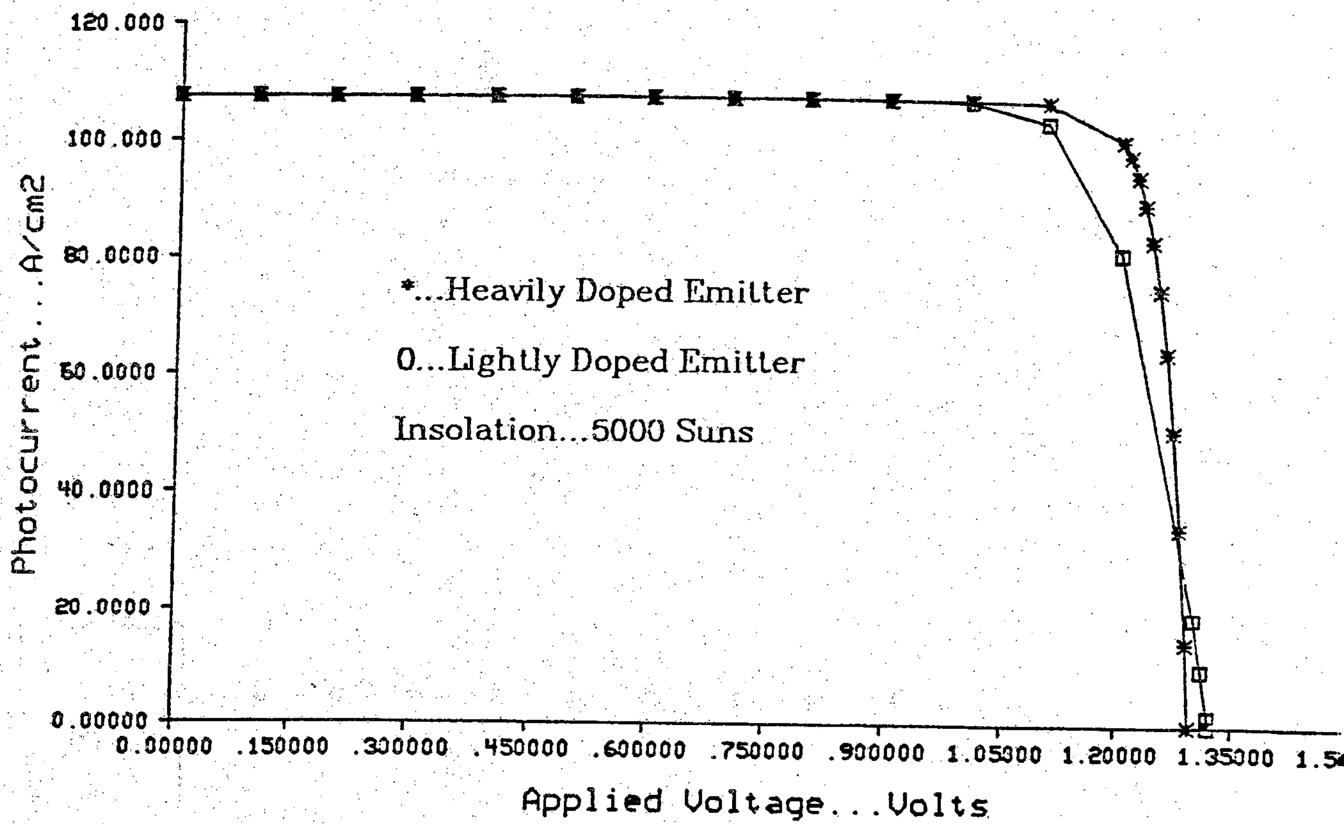

Figure 5.5.4 I versus V for practical cell

may prove superior due to its lower emitter sheet resistance.

5.6 Summary

This chapter has examined the practicality of using a graded bandgap to increase the open circuit voltage of solar cells. A simple analytical treatment was used to show that high level injection must occur in the graded portion of the cell to achieve V_{oc} enhancement and that the graded region should be p-type. The requirement for high-level injection dictates that the emitter (graded bandgap) region of the cell be lightly doped.

Because different approximations in analytical treatments of graded bandgap cells has resulted in differing conclusions regarding the importance of V_{oc} enhancement, a numerical device simulator was used to realistically assess the potential of graded bandgap $Al_xGa_{1-x}As$ solar cells. The results we presented showed that, although an extremely high solar concentration was required, V_{oc}-enhancement does occur. But the required low emitter doping caused a voltage drop that degraded the cell's fill factor. To increase the cell's performance, the emitter concentration was raised. The cell's performance was increased, but V_{oc}-enhancement was lost. Consequently, the most beneficial use of bandgap grading may be to enhance photocollection efficiency - not V_{oc}.

LIST OF REFERENCES

1. Fahrenbuch, Alan L., Richard H. Bube. *Fundamentals of Solar Cells*. New York: Academic Press, 1983.

2. Loferski, Joseph L. "Theoretical Considerations Governing the Choice of the Optimum Semiconductor for Photovoltaic Solar Energy Conversion," J. Appl. Phys., 27, No. 7, pp. 777-784, 1956.

3. Hovel, H. J. "Novel Materials and Devices for Sunlight Concentrating Systems," IBM Research and Development, 22, No. 2, pp. 112-121, 1978.

4. Fan, John C. C., Carl O. Bozler. "High Efficiency GaAs Shallow Homojunction Solar Cells," Conf. Rec., 13th IEEE Photovoltaic Spec. Conf., pp. 953-955, 1978.

5. Lender, R. J., S. Tiwari, J. M. Borrego, S. K. Ghandhi. "Diffusion Length Measurement in Schottky Barrier GaAs Solar Cells." Solid-State Electron., vol. 22, pp. 213-214, 1979.

6. Sahai, R., D. D. Edwall, J. S. Harris. "High Efficiency Thin Window $Ga_{1-x}Al_xAs$/GaAs Solar Cells," Conf. Rec. 12th IEEE Photovoltaic Spec. Conf., pp. 989-992, 1977.

7. James, L. W., R. L. Moon. "GaAs Concentrator Solar Cells," Conf. Rec. 11th IEEE Photovoltaic Spec. Conf., pp. 402-408, 1976.

8. Kamath, G. S., J. Ewan, R. C. Knechtli. "High Efficiency and Large Area (GaAl)As-GaAs Solar Cells," Conf. Rec. 12th IEEE Photovoltaic Spec. Conf., pp. 929-933, 1977.

9. Woodall, J. M., H. J. Hovel. "An Isothermal Etchback-Regrowth Method for High-Efficiency GaAlAs-GaAs Solar Cells," Applied Phys. Letters, 30, N0. 9, pp.492-493, 1977.

10. Kordos, P., G. L. Pearson. "Grown Junction GaAs Solar Cells With a Thin Graded Band-Gap AlGaAs Surface Layer," Solid-State Electron., vol. 23, pp. 399-400, 1980.

11. Turner, G. W., J. C. C. Fan, R. L. Chapman, R. P. Gale, "GaAs Shallow Homojunction Concentrator Solar Cells," Conf. Rec. 15th IEEE Photovoltaic Spec. Conf., pp. 151-155, 1981.

12. Sahai, R., D. D. Edwall, J. S. Harris. "High Efficiency AlGaAs/GaAs Concentrator Solar Cell Development," Conf. Rec. 13th IEEE Photovoltaic Spec. Conf., pp. 946-952, 1978.

13. Fichtner, Wolfgang, Donald J. Rose, Randolph E. Bank. "Semiconductor Device Simulation," IEEE Transactions on Electron Devices, ED-30, No. 9, pp. 1018-1030, 1983.

14. Pierret, Robert F. *Semiconductor Fundamentals*, Modular Series on Solid State Devices, Vol 1. Addison Wesley: Reading, Mass., 1983.

15. Konagai, M., K. Takahashi. "Theoretical Analysis of Graded Band-Gap Gallium-Aluminum Arsenide/Gallium Arsenide p-GaAlAs/p-GaAs/n-GaAs Solar Cells," Solid-State Electron., vol. 19, pp. 259-264, 1976.

16. Tsaur, S. C., A. G. Milnes, R. Sahai, D. L. Feucht. "Theoretical and Experimental Results for GaAs Solar Cells," International Symposium on GaAs, pp. 156-167, 1972.

17. Sekela, Albert M., Donald L. Feucht, Arthur G. Milnes. "Efficiency Calculations for AlGaAs Heteroface Solar Cells," IEEE Trans. Electron Devices, 24, No. 4, pp. 373-380, 1977.

18. Lamorte, M. F., D. Abbott. "Analysis of AlGaAs-GaInAs Cascade Solar Cells Under AM0-AM5 Spectra," Solid-State Electron., vol 22, pp. 467-473, 1979.

19. Lamorte, M. F., David H. Abbott. "Computer Modeling of a Two-Junction, Monolithic Cascade Solar Cell," IEEE Transactions on Electron Devices, ED-27, No. 1, pp. 231-249, 1980.

20. Lamorte, M. F., D. H. Abbott. "AlGaAs/GaAs Cascade Solar Cell Computer Modeling Under High Solar Concentration," Solar Cells, vol. 9, pp. 311-326, 1983.

21. Sutherland, Joseph E., John R. Hauser. "A Computer Analysis of Heterojunction and Graded Composition Solar Cells," IEEE Transactions on Electron Devices, ED-24, No. 4, pp. 363-372, 1977.

22. Sutherland, J. E., J. R. Hauser. "Computer Analysis of Heterojunction and Graded Bandgap Solar Cells," Conf. Rec. 12th Photovoltaic Spec. Conf., pp. 939-944, 1976.

23. Dunbar, P. M., J. R. Hauser. "A Study of Efficiency in Low Resistivity Silicon Solar Cells," Solid-State Electronics, Vol. 19, pp. 95-102, 1976.

24. Lundstrom, M. S., "Numerical Analysis of Silicon Solar Cells." Ph.D. Thesis Purdue University 1980.

25. Schwartz, R. J., M. S. Lundstrom, and R. D. Nasby. "The Degradation of High Intensity BSF Solar Cell Fill Factors Due to a Loss of Base Conductivity Modulation," IEEE Trans. Electron Devices, ED-28, No. 3, pp. 264-269, 1981.

26. Gray, Jeffery L. "Two-Dimensional Modeling of Silicon Solar Cells," Ph.D. Thesis, Purdue University, West Lafayette, IN, August 1982.

27. Martin, G. M., J. P. Farges, G. Jacob, J. P. Hallais, G. Poiblaud. "Compensation Mechanisms in GaAs," Journal of Applied Physics, 51, No. 5, p. 5840, 1980.

28. Johnson, E. J., J. A. Kafalas, R. W. Davies. "The Role of Deep-Level Centers and Compensation in Producing Semi-Insulating GaAs," Journal of Applied Physics, 54, No. 1, pp. 204-207, 1983.

29. Kressel, Henry, Jerome K. Butler. *Semiconductor Lasers* and *Heterojunction LEDs*, Academic Press, New York, 1977.

30. Sze, S. M. *Physics of Semiconductor Devices*, John Wiley & Sons, New York, 1981.

31. Blakemore, J. S. "Semiconducting and Other Major Properties of Gallium Arsenide," Journal of Applied Physics, 53, No. 10, pp. R123- R181, 1982.

32. Kurata, Mamor. *Numerical Analysis* for *Semiconductor Devices*, Lexington Books: New York, 1982.

33. Martin, G. M., A. Mitonneau, D. Pons, A. Mircea, D. W. Woodward. J. Phys. C., vol. 13, p. 3855, 1980.

34. Lee, D. S., J. G. Fossum. "Energy Band Distortion in Highly Doped Silicon," IEEE Trans. Electron Devices, ED-30, No. 6, pp. 626-634, 1983.

35. Zverev, L. P., s. A. Negashev, V. V. Kruszhaev, G. M. Min'kov. "Mechanism of Band Gap Variation in Heavily Doped Gallium Arsenide," Soviet Physics Semiconductors, 11, No. 6, pp. 603-605, 1977.

36. Kane. "Thomas-Fermi Approach to Impure Semiconductor Band Structures," Phys. Rev., vol. 131, pp. 79-88, 1963.

37. Stringfellow, G. B., H. Kunzel. "Electron Mobility in Compensated $Al_xGa_{1-x}As$," Journal of Applied Physics, 51, No. 6, pp. 3254-3261, 1980.

38. Walukiewicz, W., J. Lagowski, H. C. Gatos. "Reassessment of Space-Charge and Central Cell Scattering Contributions to GaAs Electron Mobility," Journal of Applied Physics, 52, No. 9, pp. 5853-5854, 1981.

39. Stringfellow, G. B. "Comment on 'Reassessment of Space-Charge and Central Cell Scattering Contributions to GaAs Electron Mobility'," Journal of Applied Physics, 53, No. 7, p. 5345, 1982.

40. Walukiewicz, W., J. Lagowski, H. C. Gatos. "Reply to 'Comment on "Reassessment of Space-Charge and Central Cell Scattering Contributions to GaAs Electron Mobility"'," Journal of Applied Physics, 53, No. 7, p. 5346, 1982.

41. Walukiewicz, J. Lagowski, L. Jaztrzebski, M. Lichtensteiger. "Electron Mobility and Free-Carrier Absorption in GaAs: Determination of the Compensation Ratio," Journal of Applied Physics, 50, No. 2, pp. 899-908, 1979.

42. Caughey, D. M., R. E. Thomas. "Carrier Mobilities in Silicon Empirically Related to Doping and Field," Proceedings of the IEEE, pp. 2192-2193, December 1967.

43. Stillman, G. E., C. M. Wolfe. "Electrical Characterization of Epitaxial Layers," Thin and Solid Films, vol. 31, pp. 69-88, 1976.

44. Fan, H. Y. "Effects of Free Carriers on the Optical Properties," *Semiconductors* and *Semimetals*, vol. 3, Academic Press: New York, pp. 405-419, 1967.

45. Jordan, A. S. Journal of Applied Physics, vol. 51, p. 2218, 1980.

46. Casey, H. C., M. B. Panish. *Heterostructure Lasers*, *Part A*, Academic Press: New York, 1978.

47. Haga, E., H. Kimura. J. Phys. Soc. Jap., vol. 19, p. 658, 1964.

48. Spitzer, W. G., J. M. Whelen. Phys. Rev., 114, No. 59, 1959.

49. Sturge, M. D. "Optical Absorption of Gallium Arsenide Between 0.6 and 2.75 eV," Phys. Rev., 127, No. 3, pp. 768-773, 1962.

50. Philipp, H. R., H. Ehrenreich, "Optical Properties of Semiconductors," Phys. Rev., 129, No. 4, pp. 1550-1560, 1963.

51. Casey, H. C., D. D. Sell, K. W. Wecht. "Concentration Dependence of the Absorption Coefficient for n- and p-type GaAs Between 1.3 and 1.6 eV," Journal of Applied Physics, 46, No. 1, pp. 250-257, 1975.

52. Urbach, F. Phys. Rev., vol. 92, page 1324, 1953.

53. Szczyrbowski, J. "The Exponential Shape of the Optical Absorption Edge Tail," Phys. Stat. Sol. (b), vol. 105, pp. 515-524, 1981.

54. Antonioli, G., D. Bianchi, P. Franzosi. " Intrinsic Urbach Rule and Electron-Phonon Interaction in GaAs and Related III-V Compounds," Phys. Stat. Sol. (b), vol. 106, pp. 79-84, 1981.

55. Mahan, G. D. Phys. Rev. B, vol. 5, p. 594, 1972.

56. Pankove, J. I. "Absorption Edge of Impure Gallium Arsenide," Phys. Rev., 140, No. 6a, pp. a2059-a2065, 1965.

57. Casey, H. C., Frank Stern. "Concentration Dependent Absorption and Spontaneous Emission of Heavily Doped GaAs," Journal of Applied Physics, 47, No. 2., pp. 631-643, 1976.

58. Stillman, G. E., C. M. Wolfe, J. O. Dimmock. Willardson and Beer vol 12.

59. Philipp, H. R., H. Ehrenreich. "Ultraviolet Optical Properties," *Semiconductors* and *Semimetals*, vol. 3, 1967. 19??.

60. Koltun, M. M. *Selective Optical Surfaces* for *Solar Energy Converters*, Allerton Press: New York, 1981.

61. Marple, D. T. "Refractive Index of GaAs," Journal of Applied Physics, 35, No. 4, pp. 1241-1242, 1964.

62. Stern, F. "Dispersion of the Index of Refraction Near the Absorption Edge of Semiconductors," Phys. Rev., 133, No. 6a, pp. a1653-a1664, 1964.

63. Sell, D. D., H. C. Casey, K. W. Wecht. "Concentration Dependence of the Refractive Index for n-Type and p-Type GaAs Between 1.2 and 1.8 eV," Journal of Applied Physics, 45, No. 6, pp. 2650-2657, 1974.

64. Zoroofchi, J., J. K. Butler. "Refractive Index of n-Type Gallium Arsenide," Journal of Applied Physics, 44, No. 8, pp. 3697-3699, 1973.

65. Pankove, Jacques I. *OpticalProcessesinSemiconductors*, Prentice Hall: Englewood Cliffs, NJ, 1971.

66. Li, Sheng S., W. L. Wang, P. W. Lai, R. Y. Loo, G. S. Kamath, R. C. Knechtli, "Deep Level Defects and Recombination Parameters in Proton Irradiated AlGaAs-GaAs Solar Cells," Conf. Rec. 14th Photovoltaic Spec. Conf., pp. 1080-1083, 1980.

67. Cape, J. A., J. R. Oliver, J. L. Miller, M. D. Paul. "Automated Measurement System for Solar Cell Optical Characterization Studies of GaAs and Multijunction Cascade Cells," Conf. Rec. 15th Photovoltaic Spec. Conf., pp. 1195-1198, 1981.

68. Casey, H. C., B. I. Miller, E. Pinkas. "Variation of Minority- Carrier Diffusion Lengths with Carrier Concentration in GaAs Liquid-Phase Epitaxial Layers," Journal of Applied Physics, 44, No. 3, pp. 1281-1287, 1973.

69. Sekela, A. M., D. L. Feucht, A. G. Milnes. "Diffusion Length Studies in n-Gallium Arsenide," Inst. Phys. Conf. Ser. No. 24, pp. 245-253, 1975.

70. Hrivnak, L., M. Morvic, J. Betko. "Current-Voltage Characteristics of GaAs p-i-n and n-i-n Diodes," Solid-State Electron., vol. 20, pp. 417-419, 1977.

71. Pietzsch, J. "Measurement of Minority Carrier Lifetime in GaAs and GaAsP with an Intensity-Modulate Electron Beam," Solid-State Electron., 25, No. 4, pp. 295-304, 1982.

72. Ewan, J., R. C. Knechtli, R. Loo, G. S. Kamath. "GaAs Solar Cells for High Solar Concentration Applications," Conf. Rec. 13th IEEE Photovoltaic Spec. Conf., pp. 941-945, 1978.

73. Holmes, D. E., R. T. Chen, Kenneth R. Elliot, C. G. Kirkpatrick, Phil Won Yu. "Compensation Mechanism in Liquid Encapsulated GaAs: Importance of Melt Stoichiometry," IEEE Trans. Electron. Dev., ED-29, No. 7, pp. 1045-1050, 1982.

74. Suthrland, Joseph Edward. " A Computer Analysis of Heterojunction and Graded Bandgap Solar Cell," Ph.D Thesis, North Carolina State University, Raleigh, NC, 1977.

75. Fan, John C. C., George W. Turner, Ronald P. Gale, Carl O. Bozler. "GaAs Shallow-Homojunction Solar Cells," Conf. Rec. 14th IEEE Photovoltaic Spec. Conf., pp. 1102-1105, 1980.

76. Borrego, J. M., R. P. Keeney, I. B. Bhat, K. N. Bhat, L. G. Sundaram, S. K. Ghandhi. "Photovoltaic Characteristics of Diffused p^+n Bulk GaAs Solar Cells," Conf. Rec. 16th IEEE Photovoltaic Spec. Conf., pp. 1157-1160, 1982.

77. Acket, G. A., W. Nijman, H. 't Lam. " Electron Lifetime and Diffusion Constant in Germanium-Doped Gallium Arsenide," Journal of Applied Physics, 45, No. 7, pp. 3033-3040, 1974.

78. Shen, C. C., K. P. Pande, G. L. Pearson. "Electron Diffusion Length in Liquid-Phase Epitaxial p-GaAs:Ge Layers Determined by Electron Beam Induced Current Method," Journal of Applied Physics, 53, No. 2, pp. 1236-1237, 1982.

79. Krautle, H., P. Narozny, H. Beneking. "Lateral PNP GaAs Bipolar Transistor with Minimized Substrate Current," Electron Device Letters, 3, No. 10, pp. 315-317, 1982.

80. Lender, R. J., S. Tiwari,J. M. Borrego, S K. Ghandhi. "Diffusion Length Measurement in Schottky Barrier GaAs Solar Cells," Solid- State Electron., vol. 22, pp. 213-214, 1979.

81. Paz, O., J. M. Borrego. "Determination of Diffusion Length of Electron Beam Induced Minority Carriers in Polycrystalline GaAs," Applied Physics Letters, 41, No. 11, pp. 958-960, 1982.

82. Hutchby, James A., Richard L. Furdurich. "Theoretical Optimization and Parametric Study of n- on p $Al_xGa_{1-x}As$–GaAs Graded Band-Gap Solar Cells," Journal of Applied Physics, 47, No. 7, pp. 3152-3158, 1976.

83. Yim, Michael. "Direct and Indirect OPtical Energy Gaps of AlAs," Journal of Applied Physics, 42, No. 7, pp. 2854-2856, 1971.

84. Mead, C. A., W. G. Spitzer. "Conduction Band Minima in AlAs and AlSb," Physical Review Letters, 11, No. 8., pp. 358-360, 1963.

85. Lorenz, M. R., R. Chicotka, G. D. Pettit. "The Fundamental Absorption Edge of AlAs and AlP," Solid State Communications, vol. 8, pp. 693- 697, 1976.

86. Johnson, Ernest J. "Absorption Near the Fundamental Edge," *Semiconductors* and *Semimetals*, vol. 3, pp. 154-158, 1967.

87. Fern, R. E., A. Onton. "Refractive Index of AlAs," Journal of Applied Physics, 42, No. 9, pp. 3499-3500, 1971.

88. Kuphal, E., H. W. Dingle. "Composition and Refractive Index of $Ga_xAl_{1-x}As$ as Determined by Ellipsometry," Journal of Applied Physics, 50, No. 6, pp. 4196-4200, 1979.

89. Aframowitz, Martin A. "Refractive Index of $Ga_xAl_{1-x}As$," Solid State Communications, vol. 15, pp. 59-63, 1974.

90. Wemple, S. H., M. DiDomenico. "Behavior of the Electronic Dielectric Constant in Covalent and Ionic Materials," Phys. Rev. B, 3, No. 4, pp. 1338-1345, 1971.

91. Pikhtin, A. N., A. D. Yas'kov. "Dispersion of the Refractive Index of Semiconducting Solid Solutions with the Sphalerite Structure," Soviet Physics Semiconductors, 14, No. 4, pp. 389-392, 1980.

92. Pikhtin, A. N., A. D. Yas'kov. "Dispersion of the Refractive Index of Semiconductors with Diamond and Zinc-Blende Structures," 12, No. 6, pp. 622-626, 1978.

93. Barnes, P. A., D. P. Schinke. "Refractive Index of a Native Oxide Anodically Grown on GaAs," Applied Physics Letters, 30, No. 1, pp. 26-28, 1977.

94. Ishii, T., B. Jeppsson. "Influence of Temperature on Anodically Grown Native Oxides on Gallium Arsenide," Journal of the Electrochemical Society, 124, No. 11, pp. 1784-1794, 1977.

95. Ghandhi, S. K., R. J. Field. "Precisely Controlled Shallow p^+ Diffusions in GaAs," Appl. Phys. Letters, 38, No. 4, pp. 267-268, 1981.

96. J. Tauc, "Generation of an emf in Semiconductors with Nonequilibrium Current Carrier Concentrations," *Reviews of Modern Physics*, vol. 29, no. 3, pp. 308-32, July 1957.

97. P. R. Emtage, "Electrical Conduction and the Photovoltaic Effect in Semiconductors with Position-Dependent Band Gaps," *J. Appl. Phys.*, vol. 33, no. 6, pp. 1950-1960, June 1962.

98. J. C. C. Fan, G. W. Turner, R. P. Gale, and C. O. Bozler, "GaAs Shallow-Homojunction Solar Cells," *14th IEEE Photovoltaic Spec. Conf.*, pp. 1102-1105, 1980.

99. J. M. Borrego, R. P. Keeney, I. B. Bhat, K. N. Bhat, L. G. Sundaram, and S. K. Ghandi, "Photovoltaic Characteristics of Diffused P^+N Bulk GaAs Solar Cells," *16th IEEE Photovoltaic Spec. Conf.*, pp. 1157-1160, 1982.

100. R. Sahai, D. D. Edwall, E. Cory, and J. S. Harris, "High Efficiency Thin Window $Ga_{(1-x)}Al_xAs/GaAs$ Solar Cells," *12th IEEE Photovoltaic Spec. Conf.*, pp. 989-992, 1977.

101. J. Ewan, R. C. Knechtli, R. Loo, and G. S. Kamath, "GaAs Solar Cells for High Solar Concentration Applications," *13th IEEE Photovoltaic Spec. Conf.*, pp. 941-945, 1978.

102. H. A. Vander Plas, L. W. James, R. L. Moon, and N. J. Nelson, "Performance of AlGaAs/GaAs Terrestrial Concentrator Solar Cells," *13th IEEE Photovoltaic Spec. Conf.*, pp. 934-940, 1978.

103. P. Kordos and G. L. Pearson, "Grown Junction GaAs Solar Cells with a Thin Graded Band-Gap $Al_xGa_{1-x}As$ Surface Layer," *Solid-State Electron.*, vol. 23, no. 4, pp. 399-400, April 1980.

104. J. C. C. Fan, A. R. Calawa, R. L. Chapman, and G. W. Turner, "Efficient Shallow-Homojunction GaAs Solar Cells by Molecular Beam Epitaxy," *Appl. Phys. Lett.*, vol. 35, no. 10, pp. 804-806, Nov. 1979.

105. D. K. Wagner and J. R. Shealy, "Graded Bandgap AlGaAs Solar Cells Grown by OMVPE," To be published in *17th IEEE Photovoltaic Spec. Conf.* .

106. D. K. Wagner and J. R. Shealy, "Graded Band-Gap p/n AlGaAs Solar Cells Grown by Organometallic Vapor Phase Epitaxy," *Appl. Phys. Lett.*, vol. 45, no. 2, pp. 162-164, July 1984.

107. H. J. Hovel, J. M. Woodall, and W. E. Howard, "The Spectral Response and Conversion Efficiency of $Ga_{1-x}Al_xAs$–GaAs Solar Cells," *1972 Symp. on GaAs*, pp. 205-213, 1972.

108. J. A. Hutchby and R. L. Fudurich, "Theoretical Optimization and Parametric Study of n-on-p $Al_xGa_{1-x}As$–GaAs Graded Band-Gap Solar Cell," *J. Appl. Phys.*, vol. 47, no. 7, pp. 3152-3158, July 1976.

109. M. Konagai and K. Takahashi, "Theoretical Analysis of Graded-Band-Gap Gallium-Aluminum Arsenide/Gallium Arsenide p–$Ga_{1-x}Al_xAs$/p–GaAs/n–GaAs Solar Cells," *Solid-State Electron.*, vol. 19, pp. 259-264, 1976.

110. J. A. Hutchby, "High Efficiency Graded Band-Gap $Al_xGa_{1-x}As$–GaAs p-on-n Solar Cell," *11th IEEE Photovoltaic Spec. Conf.*, pp. 414-423, 1975.

111. J. M. Borrego, S. K. Ghandhi, and D. A. Page, "A High Efficiency Bulk Graded Band Gap/PN Junction Solar Cell Structure at High Concentration Ratios," To be published in *17th IEEE Photovoltaic Spec. Conf.* .

112. A. N. Imenkov, N. Nazarov, B. V. Suleimenov, B. V. Tsarenkov, and Yu. P. Yakovlev, "Experimental Detection of Variable-Gap Photo-emf," *Sov. Phys. Semicond.*, vol. 12, no. 12, pp. 1413-1417, Dec. 1978.

113. Y. Marfaing and J. Chevallier, "Photovoltaic Effects in Graded Bandgap Structures," *IEEE Trans. Electron Devices*, vol. ED-18, no. 8, pp. 465-471, Aug. 1971.

114. V. M. Evdokimov, A. F. Milovanov, and D. S. Strebkov, "Utilization of the Incident Radiation in Semiconductors Exhibiting the Bulk Photovoltaic Effect," *Sov. Phys. Semicond.*, vol. 11, no. 11, pp. 1308-1309, Nov. 1977.

115. O. V. Konstantinov and G. V. Tsarenkov, "Photoconductivity and Dember Effect in Variable-Gap Semiconductors," *Sov. Phys. Semicond.*, vol. 10, no. 4, pp. 427-432, April 1976.

116. M. S. Lundstrom, "Numerical Simulation of Silicon Solar Cells," Purdue University, School of Electrical Engineering Tech. Rept. TR-EE 80-27, 1980.

117. C. M. Maziar, "Material Models and Device Structures for GaAs Solar Cells," Master's Thesis, Purdue University, 1984.

118. J. E. Sutherland and J. R. Hauser, "A Computer Analysis of Heterojunction and Graded Composition Solar Cells," *IEEE Trans. Electron Devices*, vol. ED-24, no. 4, pp. 363-372, April 1977.

119. J. E. Sutherland, "A Computer Analysis of Heterojunction and Graded Bandgap Solar Cells," Doctoral Thesis, North Carolina State University, 1977.

120. J. E. Sutherland and J. R. Hauser, "Computer Analysis of Heterojunction and Graded Bandgap Solar Cells," *12th IEEE Photovoltaic Spec. Conf.*, pp. 939-944, 1976.

121. M. S. Lundstrom and R. J. Schuelke, "Numerical Analysis of Heterostructure Semiconductor Devices," *IEEE Trans. Electron Devices*, vol. ED-30, no. 9, pp. 1151-1159, Sept. 1983.

122. M. S. Lundstrom and R. J. Schuelke, "Computer Simulation of Integrated Circuit Devices and Fabrication Processes," Purdue University, School of Electrical Engineering Tech. Rept. TR-EE 84-1, Jan. 1984.

123. R. J. Schuelke, "Numerical Simulation of Semiconductor Heterostructures," Doctoral Thesis, Purdue University, 1984.

124. B. Carnahan, H. A. Luther, and J. O. Wilkes, *Applied Numerical Methods*, John Wiley and Sons Inc., New York, 1969.

[125]B.R. Nag, *Theory of Electron Transport in Semiconductors*, Pergamon Press, New York, 1972.

APPENDICES

APPENDIX A

```
c
c               COMPCAL.F
c
c
c        This program finds the compensator concentration.
c       We use Walukiewicz's definition of the compensation
c       ratio:
c               THETA=(COMPENSATOR CONC.)/(CARRIER CONC.)
c        It uses the IMSL routine ICSCCU.
c
c
      Dimension c(9,3),mumin(10),alpha(10),nref(10),y(10),x(10)
        real mumin,alpha,nref,mumax,comp,incon,c,y,x,inmu
        data mumin /2750.,2100.,1750.,1350.,1100.,800.,550.,
   c     400.,200.,100./
        data alpha /0.553,0.568,0.537,0.531,0.542,0.539,0.537,0.554,
   c     0.551,0.594/
        data nref /9.85e16,1.03e17,8.1e16,6.8e16,5.09e16,3.89e16,
   c     2.79e16,1.74e16,9.85e15,4.02e15/
        data mumax,nx,ic /8200.,10,9/
        data incon,inmu /2.7e16,5200/
c
c        User Screen Prompts
c
 01      write(6,02)
 02      format(//5x,'ENTER INITIAL CARRIER CONC>',/,10x)
         read(5,03) incon
 03      format(e10.2)
       write(6,04)
 04      format(//5x,'ENTER INITIAL MOBILITY',/,10x)
       read(5,05) inmu
 05     format(e10.2)
        do 10 i=1,10
              x(11-i)=(mumax-mumin(i))/(1+(incon/nref(i))**(alpha(i)))
              x(11-i)=x(11-i)+mumin(i)
              y(11-i)=0.1*(i-1)
              write(6,15) x(11-i),y(11-i)
 15           format(5x,'x= ',e10.2,5x,'y= ',e10.2)
 10     continue
c
c        Call IMSL 2-D Interpolation Routine
```

```
c
        call icsccu(x,y,nx,c,ic,ier)
        index=1
        if (inmu .lt. x(index)) then
                index= 0
        else
 20           if (inmu .gt. x(index)) then
                index=index +1
              go to 20
                endif
        endif
c
c       Compute Compensation
c
        if (index .eq. 0) then
                comp=0.0
        else
                d= inmu-x(index)
                comp= c(index,3)*d + c(index,2)*d + c(index,1)*d
                comp= comp + y(index)
        endif
        cmpcon=incon*comp
c
c       Output Results to Terminal Scree
c
       write(6,25) comp
 25     format(/5x,'*** theta= ',f5.2,'  ***')
        write(6,30) cmpcon
 30     format(/5x,'*** cmpcon= ',e10.2,'  ***')
       go to 01
        stop
        end
```

APPENDIX B

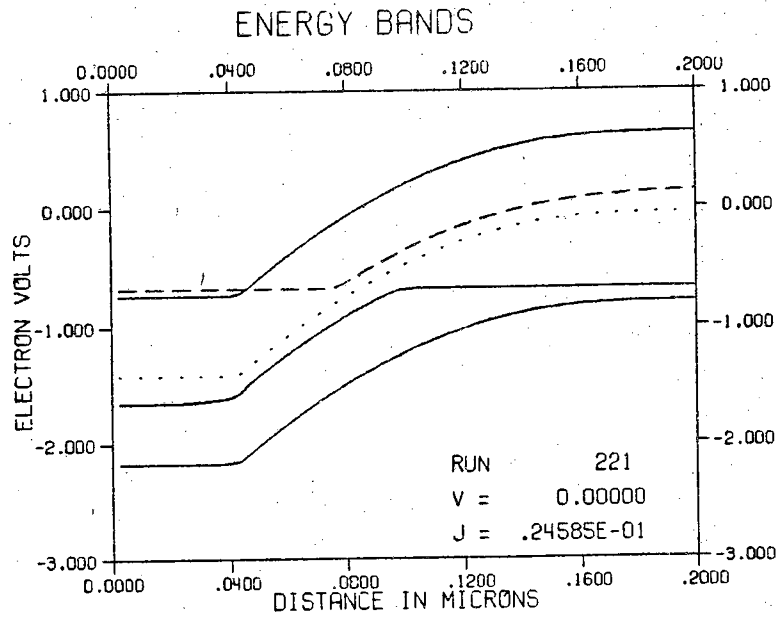

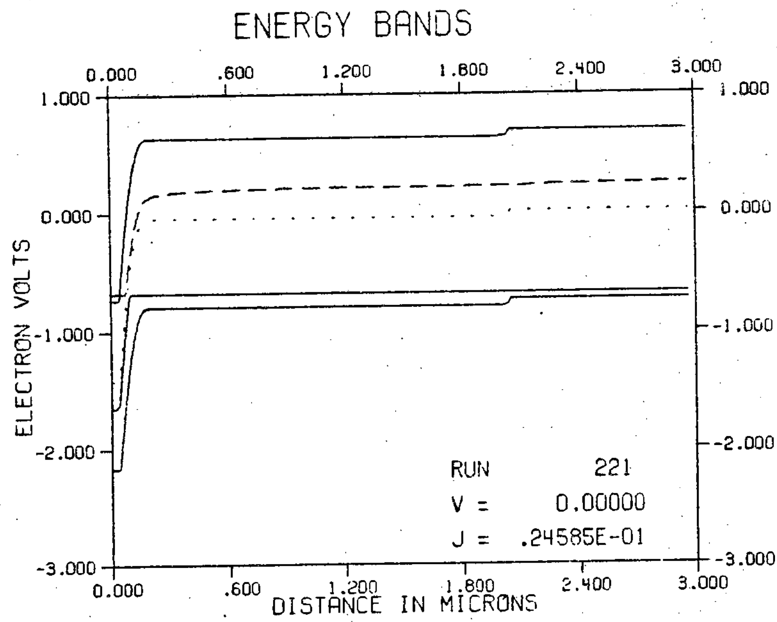

Figure B.1 Energy Band Diagrams.. Fan-Bozler Shallow Homojunction

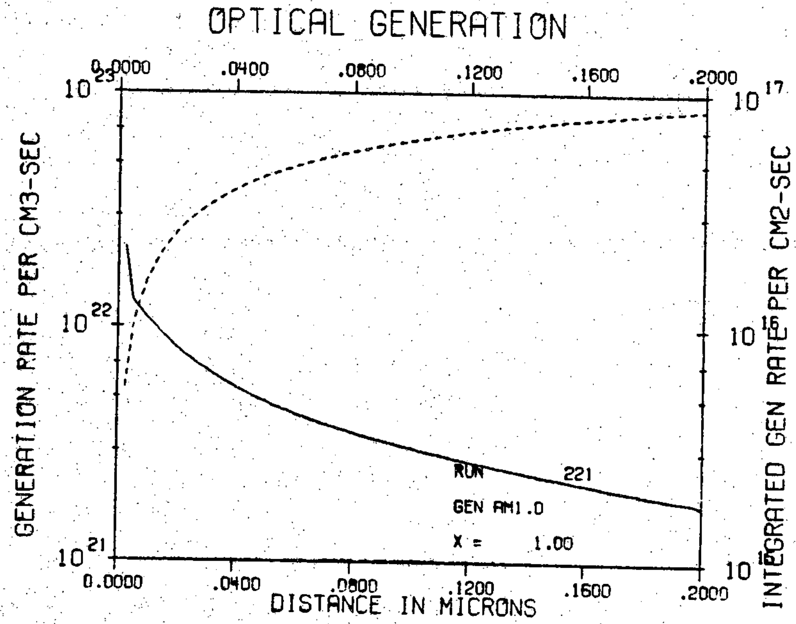

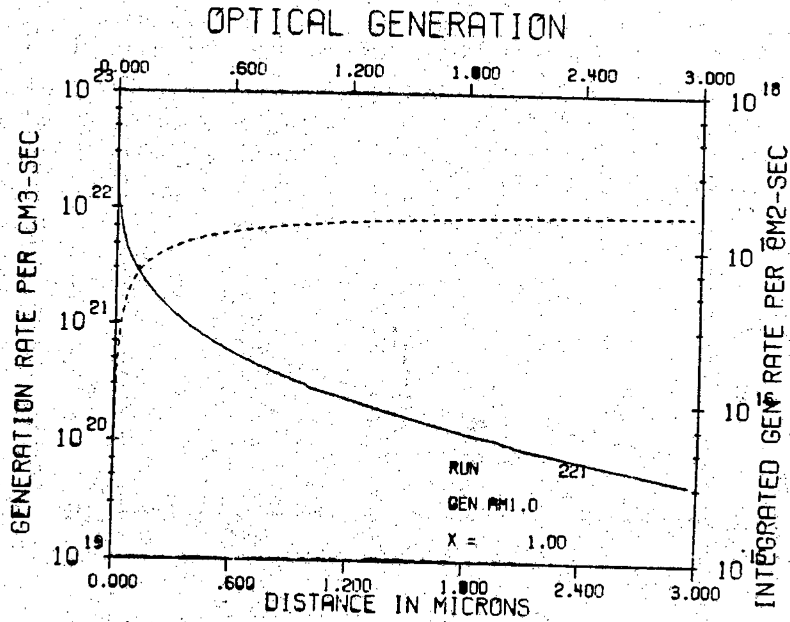

Figure B.2 Optical Generation

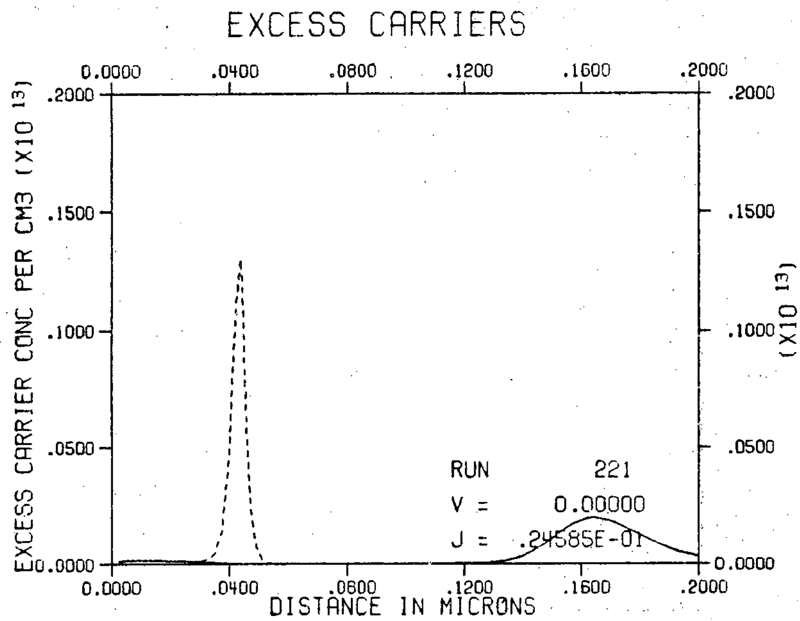

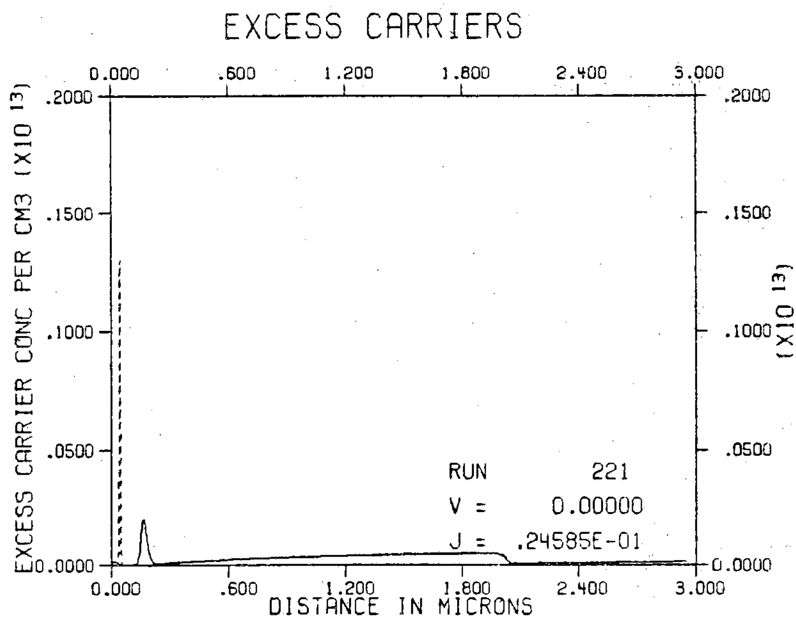

Figure B.3 Excess Carrier Concentration

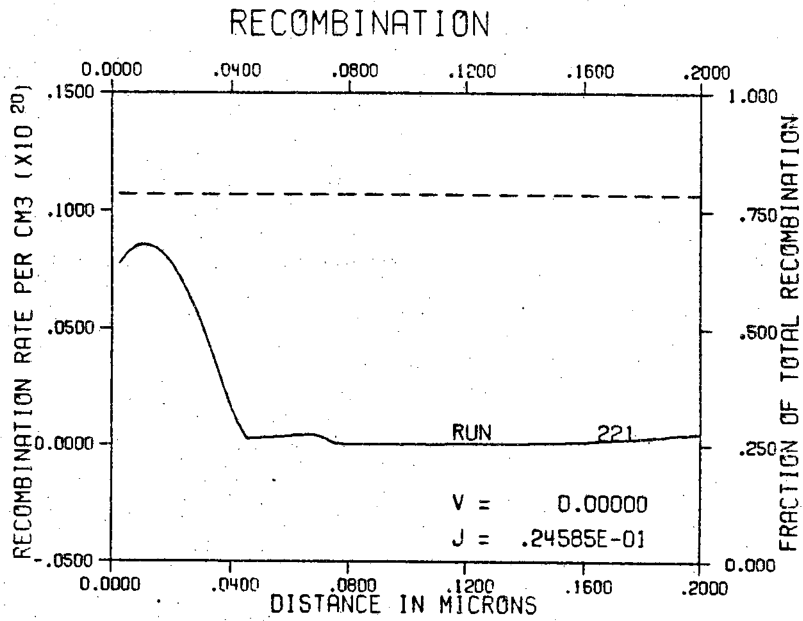

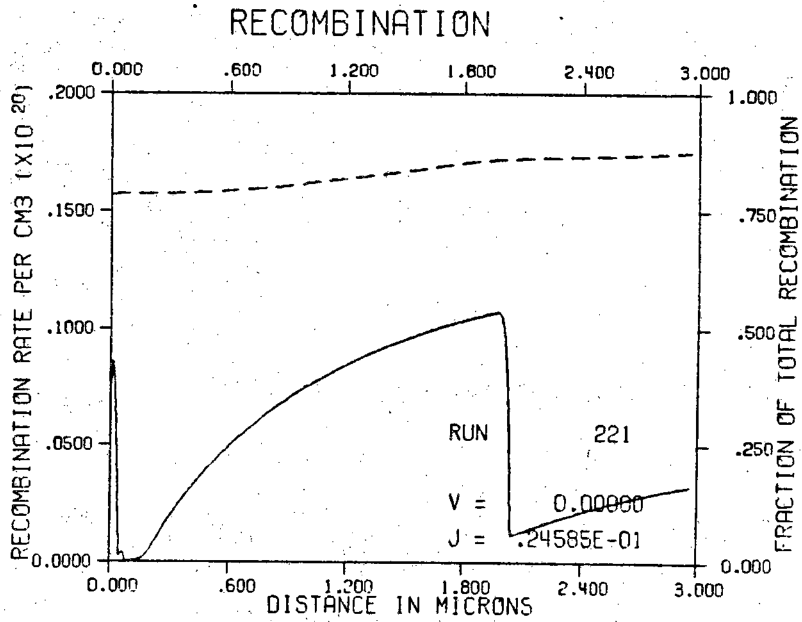

Figure B.4 Recombination Rate

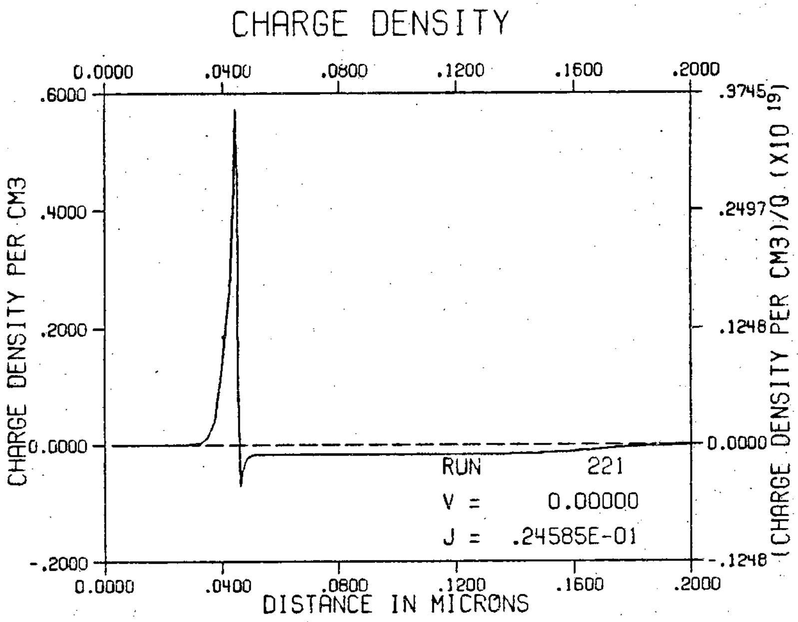

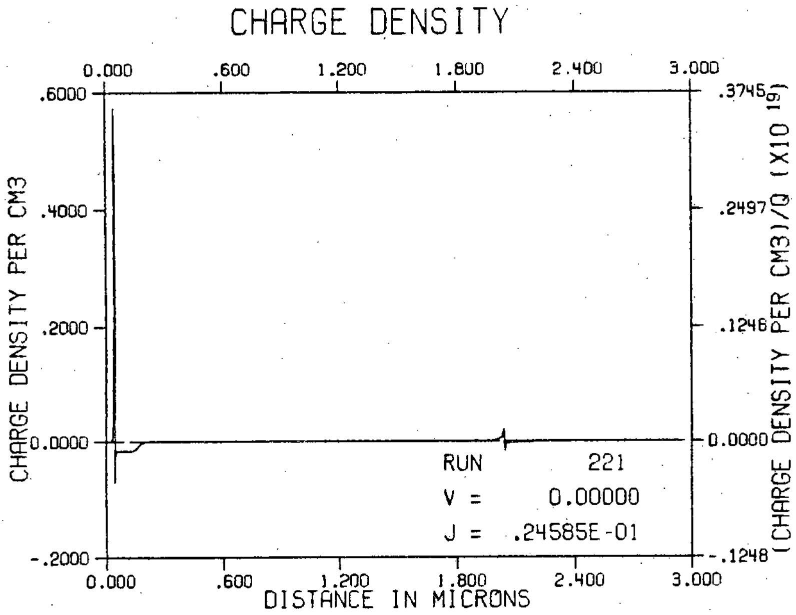

Figure B.5 Charge Density

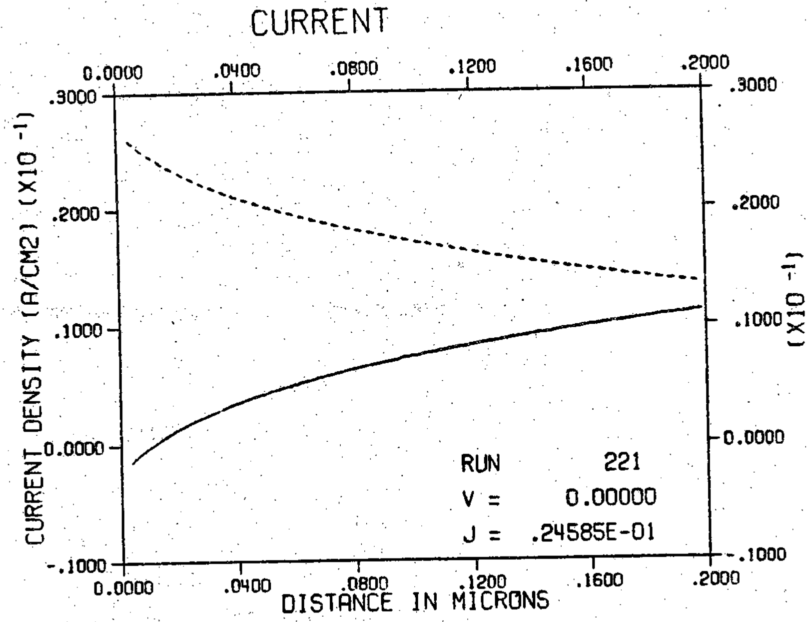

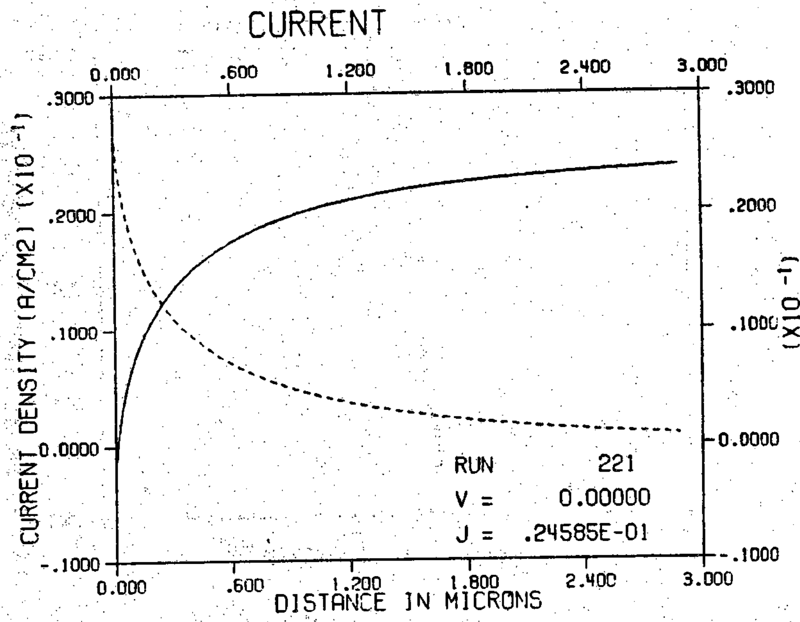

Figure B.6 Current Density

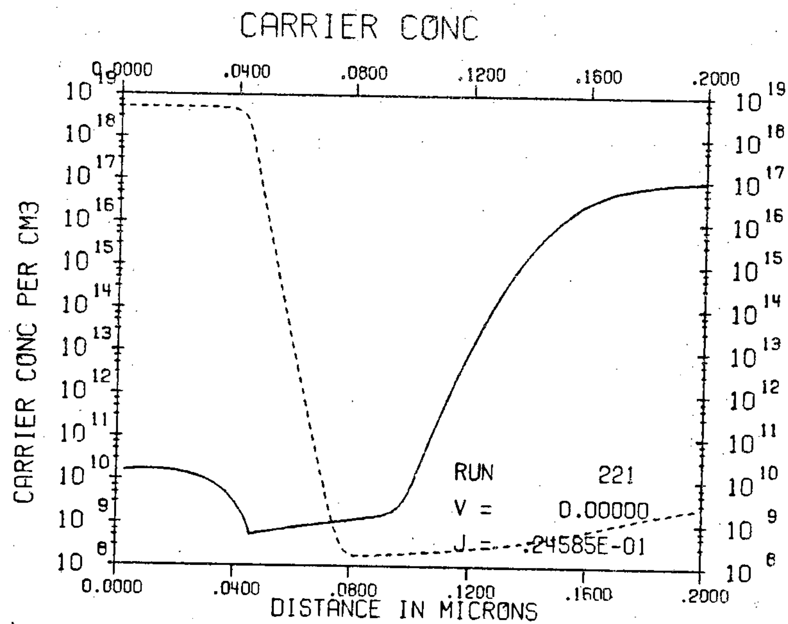

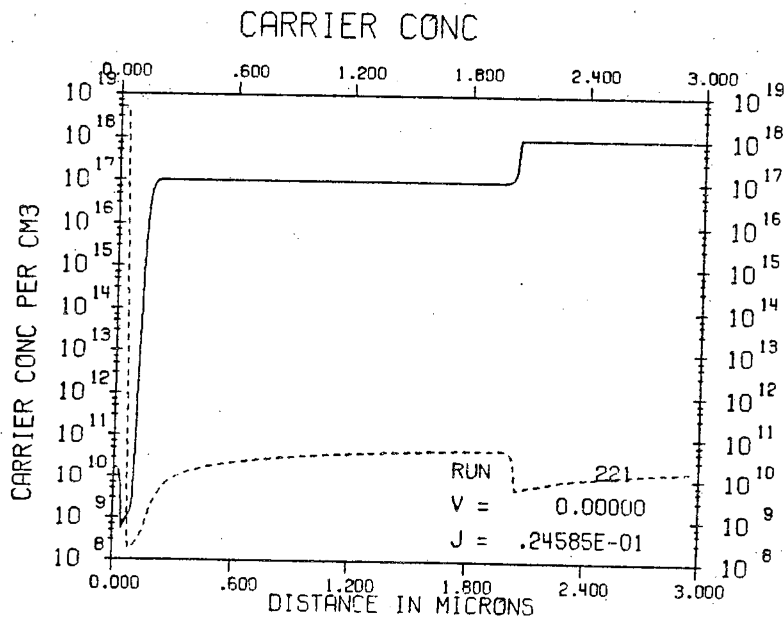

Figure B.7 Carrier Concentration

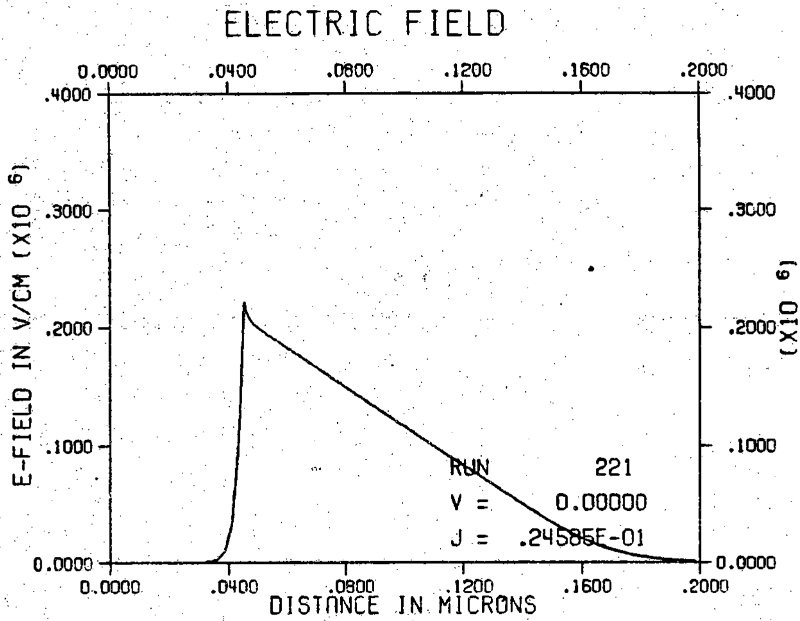

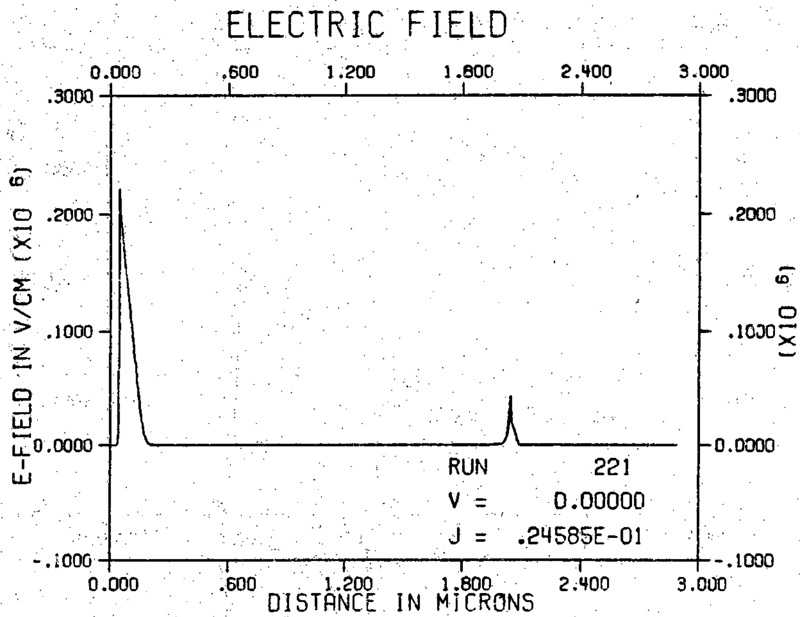

Figure B.8 Electric Field

APPENDIX C

SCAP1D(GAAS) USER'S MANUAL

The input deck for SCAP1D has input cards of the form:

```
NAME  KEY1=VALUE1, KEY2=STRING2, ..., KEYn=VALUEn
+     ARRAY1=VA1/VA2/VA3/VA4, ARRAY2=WA1/WA2
```

Each card begins in column 1 with its name; a card may be up to 5 lines long. If a card is longer than one line, the continuation symbol, +, must appear in column 1 for lines 2, 3, 4, etc. Commas or blanks are assumed to be separaters; any number of separaters may appear between assignments. An assignment cannot contain any blanks, i.e.

PARM = - 12.0

is not valid. The above assigment should read:

PARM=-12.0

Values are assigned to arrays by separating the values by /'s In the example card shown above, values are defined for ARRAY1(1), ARRAY1(2), ARRAY1(3), ARRAY1(4), and for ARRAY2(1), and ARRAY2(2). Any parameter that does not appear in the card assumes its default value. Only those keys that are to be changed from their default value need to be specified. If the default values are to be used for all parameters of the card, the card need not appear.

The input deck consists of a title followed by several other cards. The *TITLE card, which consists of up to 80 characters, is used to identify the simulation run; it must not be omitted. For the other cards, order is not significant. On the following pages, we briefly describe the allowed keys and their default values for of the cards.

MESH

The MESH card is used to specify the finite difference mesh for the problem. Since the accuracy of the computed results is to a great extent determined by the quality of the mesh, it should be carefully specified. When specifying the mesh, several nodes should be placed in each of the doping layers defined. Nodes should also be concentrated where the electrostatic potential is expected to vary rapidly.

The possible keys are:

NODES	The number of nodes to be used in the mesh. Allowed values are integers between 1 and 250. Default value: NODES=250
XD(i)	The user-specified mesh is defined by dividing the device length into a number of sections, then placing a specified number of nodes uniformly within these regions. The XD(i) keys, where $1 \leq i \leq 20$, specify the right edge of each section in micrometers. Default value: XD(1)=10.0
NXD(i)	The number of nodes to be place within each of the sections. an NXD(i) values must be specified for each XD(i) specified. The sum of the NXD(i), the total number of nodes, must not exceed 251. Note that the $x = 0$ boundary node is not among these, but the boundary at $x = L$ is. Default value: NXD(1)=251
ND	The number of mesh regions to be used. If we have XD(1), XD(2), XD(3), and NXD(1), NXD(2), NXD(3), then ND=4. Default value: ND=1

SOLVE

The SOLVE card is used to specify iteration and convergence criteria for the finite difference solution. For most applications, the default values of these parameters should be used. Note that changes to DELMAX can affect the accuracy of the results.

The possible keys are:

DELMAX — Before iteration can be terminated, the maximum change in the electrostatic potential between iterations must be less than DELMAX. DELMAX is a dimensionless voltage measured in units of kT/q. Default value: DELMAX=1.0e-06

ITMAX — ITMAX is the maximum number of iterations allowed. The program aborts if convergence it not achieved in ITMAX or fewer iterations. Default value: ITMAX=30

MISC

The MISC card is used to specify certain device-related parameters for the simulation such as the cross-sectional area, and operating temperature.

The possible keys are:

TEMP — A real variable that specifies the operating temperature in degree centigrade. Default value: TEMP=27.0

IGAM — The effective asymmetry factor gamma may be set to 0.0, 1.0, or 0.5. These settings correspond to IGAM equal to 0, 1, and 2 respectively. Refer to M.S. Lundstrom, Numerical Analysis of Silicon Solar Cells, Ph.D Thesis. Default value: IGAM=2

AREA — The device cross-sectional area in square centimeters. Default value: AREA=1.0

RS — The external series resistance. Default value: RS=0.0

IBGN

An integer variable which specifies the type of bandgap narrowing model to be selected.

IBGN=0 - bandgap narrowing suppressed

IBGN=2 - Lanyon-Tuft bandgap narrowing modeled

Default value: IBGN=0

DOPSTEP

The DOPSTEP card is used to specify the position-dependent donor and acceptor concentrations and related parameters for step profiles.

The possible keys are:

XSTEP(i) — Doping profiles consisting of up to 10 piece-wise constant intervals may be specified. XSTEP(i), where $1 \leq i \leq 10$, specifies the right endpoint (in microns) of the ith section. Default value: XSTEP(1)=0.0

DSTEP(i) — The impurity concentration per cubic centimeter in the ith section. DSTEP(i) is positive for donor impurities and negative for acceptors. DSTEP(i)=$N_D - N_A$. Default value: DSTEP(1)=0.0

UDOP — A logical variable that, if true, tells the program that the user is supplying his own FORTRAN function subroutine to define the donor and acceptor concentrations versus position. Default value: UDOP=FALSE

NSTEP — The number of individual doping regions. One step junction constitutes two doping regions. Default value: nstep=1

DOPBULK — The doping of the bulk material in per cubic centimeters. Default value: dopbulk=1.0e16

DOPERFC

The DOPERFC card is used to specify the position-dependent donor and acceptor concentrations and related parameters for complementary error profiles.

The possible keys are:

XJF	The junction depth measured from the front surface in microns. Default value: XJF=1.0
XJB	The junction depth measured from the back surface in microns. Default value: XJB=1.0
DOPO	The impurity doping at the front surface measured in per cubic centimeters. Default value: DOPO=1.0e16
DOPL	The impurity doping at the back surface measured in per cubic centimeters. Default value: DOPL=1.0e16
DOPBULK	The impurity doping in the bulk. Default value: DOPBULK=1.0e16

CONTACT

The CONTACT card is used to specify the type of contacts at both the front and back ends of the cell.

The possible keys are:

SF	The front surface recombination velocity in centimeters per second. Default value: SF=0.0
SB	The back surface recombination velocity in centimeters per second. Default value: SB=0.0
OHMIC	A string that indentifies which contacts are ohmic. The options are front, back, both, or none. Default value: OHMIC=NONE
SBFRONT	A logical variable which indicates a Schottky-barrier on the front surface of the cell. Default value: SBFRONT=FALSE
SBBACK	A logical variable which indicates a Schottky-barrier on the back surface of the cell. Default value: SBBACK=FALSE
PHIMF	The work function difference at the front surface of the cell in electron volts. Default value: PHIMF=0.0
PHIMB	The work function difference at the back surface of the cell in electron volts. Default value: PHIMB=0.0

I-V

The I-V card is used to specify the desired range of applied biases for a dark I-V simulation. The back (X = L) contact is assumed to be grounded and the bias (in volts) is applied to the front (x = 0) contact. The total number of applied biases specified by this card must not exceed 25.

The possible keys are:

VSTART The starting bias in volts. Default value: VSTART=0.0

VSTOP The ending bias in volts. Default value: VSTOP=0.0

VDEL The bias increment in volts. The total number of biases thus specified must not exceed 25. Default value: VDEL=0.10

V(i) A real array which specifies the bias in volts. This variable should not be used in conjunction with VSTART, VSTOP, and VDEL.

SOLCELL

The SOLCELL card is used to specify the desired range of applied biases for an illuminated device. The back (X = L) contact is assumed to be grounded and the bias (in volts) is applied to the front (x = 0) contact. The total number of applied biases specified by this card must not exceed 25.

The possible keys are:

VSTART — The starting bias in volts. Default value: VSTART=0.0

VSTOP — The ending bias in volts. Default value: VSTOP=0.0

VDEL — The bias increment in volts. The total number of biases thus specified must not exceed 25. Default value: VDEL=0.10

V(i) — A real array which specifies the bias in volts. This variable should not be used in conjunction with VSTART, VSTOP, and VDEL. The total number of biases thus specified must not exceed 25.

DROP — When computing the current-voltage characteristics the voltage increment is changed to VINCR once the current reaches a fraction DROP of the short circuit current. Default value: DROP=0.90

VINCR — The bias increment in volts for currents less than DROP of the short circuit current. Default value: VINCR=0.02

SPEC

The SPEC card specifies parameters for a spectral response simulation.

The possible keys are:

Key	Description
WSTART	The starting wavelength in microns. Default value: WSTART=0.3
WSTOP	The stopping wavelength in microns. Default value: WSTOP=1.0
WINC	The wavelength increment in microns. The total number of wavelengths specified must not exceed 20. Default value: WINC=0.1
WL(i)	An array for specifying as many as 20 wavelengths. WL is not to be used in conjunction with WSTART, WSTOP, and WINC.
JSR	The incident photon flux divided by q for each wavelength specified (units are amps per square centimeter). Default value: JSR=1.0e-6
VSR	The bias voltage measured in volts. Default value: VSR=0.0

RECOMB

The RECOMB card specifies recombination characteristics of the device.

The possible keys are:

TAUP — The lifetime of holes measured in seconds. Default value: TAUP=1.0e-9

TAUN — The lifetime of electrons measured in seconds. Default value: TAUN=1.0e-9

AUGER — A logical variable which if true, will specify that auger recombination modeling is to be used. Default value: AUGER=FALSE

MIDG — A logical variable which if true, will specify the intrinsic level as the trap energy level for SRH recombination. Default value: MIDG=TRUE

AP — The auger recombination coefficient for holes measured in inverse seconds. Default value: AP=1.0e-35

AN — The auger recombination coefficient for electrons measured in inverse seconds. Default value: AP=1.0e-35

ZKP — The cutoff concentration for doping dependent minority carrier lifetime for holes.

$$\tau_p = \frac{\mathrm{TAUP}}{1 + \frac{N_D + N_A}{\mathrm{ZKP}}}$$

Default value: ZKP=1.0e50

ZKN — The cutoff concentration for doping dependent minority carrier lifetime for electrons.

$$\tau_n = \frac{\mathrm{TAUN}}{1 + \frac{N_D + N_A}{\mathrm{ZKN}}}$$

Default value: ZKN=1.0e50

ARCOAT

The ARCOAT card specifies parameters concerning the anti- reflective coating. The possible keys are:

REFLECT	A logical variable which if true, indicates that reflection is being modeled. If false, all incident radiation is entering the device. Default value: REFLECT=FALSE
NLYERS	A maximum of three layers may be used for anti-reflective coatings. $0 \leq$NLYERS≤ 3 Default value: NLYERS=0
TH1	The thickness of the first anti-reflective layer adjacent to the front of the device measured in microns. Default value: TH1=0.0
TH2	The thickness of the second anti-reflective layer adjacent to the first layer measured in microns. Default value: TH2=0.0
TH3	The thickness of the third anti-reflective layer adjacent to the second layer measured in microns. Default value: TH3=0.0
REMAT1	A character string representing the reflective material of the first layer. Choices of material are "ANOX" and "ALGAAS", which are anodic oxide and aluminum gallium arsenide respectively.
REMAT2	A character string representing the reflective material of the second layer.
REMAT3	A character string representing the reflective material of the third layer.

GENRATE

The GENRATE card specifies parameters concerning generation of carriers such as the type of illumination and solar concentration.

The possible keys are:

IGEN — The types of optical generation are:

- DARK - no illumination
- AM0 - amo spectrum
- AM1.0 - am1.0 spectrum
- AM1.5 - am1.5 spectrum
- GDATA - spectrum in file labeled gdata
- UNIFORM - uniform illumination
- UGEN - uniform generation
- MONO - monochromatic illumination

Default value: IGEN=DARK

CONCEN — The solar concentration measured in suns. Default value: CONCEN=1.0

SHADOW — The fraction of the incident illumination shadowed Default value: SHADOW=0.0

WAVEL — The wavelength to be used for monochromatic illumination as measured in microns. Default value: WAVEL=1.0

FLUXQ — The incident flux divided by q to be used for monochromatic illumination measured in amperes per square centimeter. Default value: FLUXQ=1.0e-6

RBACK — The fraction of the illumination reflected off of the back surface. Default value: RBACK=0.0

ANGLE — The angle with which the incident illumination strikes the cell. Measured from the normal to the front surface in degrees. Default value: ANGLE=0.0

OUTPUT

The OUTPUT card specifies the kind and amount of output to be printed.

The possible keys are:

IPRINT	An integer value which indicates the amount of debugging output. IPRINT may vary from 0 to 5, with 0 being the least amount of output and 5 the most. Default value: IPRINT=0
TABL	A logical variable that, if true, specifies a table of results of the non-equilibrium solution. Default value: TABL=FALSE
TABLQ	A logical variable that, if true, specifies a table of results of the equilibrium solution. Default value: TABLQ=TRUE
PSTEP	An integer variable which specifies the interval of nodes to be printed in the equilibrium table. PSTEP=1 means print every node. PSTEP=2 means print every other node, and so forth. Default value: PSTEP=1
SAVE	A logical variable which, if true, specifies that the output is to be saved on magnetic tape. Default value: SAVE=FALSE
IRUNNUM	An integer which specifies the run number. Default value: IRUNNUM=-1

DEFAULT INPUT DECK

The default input deck is listed below. Lines which start with a blank are ignored when read.

```
*TITLE   DEFAULT INPUT DECK
MISC     TEMP=27.0,AREA=1.0,IBGN=0,IGAM=2,RS=0.0
DOPSTEP  XSTEP=0.0,DSTEP=0.0,NSTEP=1,DOPBULK=1.0e16,UDOP=FALSE
 DOPERFC  XJF=1.0,XJB=1.0,DOPO=1.0e16,DOPL=1.0e16,DOPBULK=1.0e16
MESH     ND=1,NXD=251,XD=10.0,NODES=250
SOLVE    ITMAX=30,DELMAX=1.0e-6
RECOMB   AUGER=FALSE,MIDG=TRUE,AN=1.0e-35,AP=1.0e-35,TAUP=1.0e-9
+        TAUN=1.0e-9,ZKN=1.0e50,ZKP=1.0e50
CONTACT  SF=0.0,SB=0.0,OHMIC=none,SBFRONT=FALSE,SBBACK=false
+        PHIMF=0.0,PHIMB=0.0
ARCOAT   REFLECT=FALSE,NLYERS=0,TH1=0.0,TH2=0.0,TH3=0.0
SOLCELL  VSTART=0.0,VSTOP=0.0,VDEL=0.1,VINCR=0.02,DROP=0.90
 I-V     VSTART=0.0,VSTOP=0.0,VDEL=0.1
 SPEC    WSTART=0.3,WSTOP=1.0,WINC=0.1,JSR=1.0e-6,VSR=0.0
OUTPUT   IRUNNUM=-1,IPRINT=0,PSTEP=1,TABL=FALSE,TABLQ=TRUE
+        SAVE=FALSE
```